ENERGY HARVESTING OF INFRARED RADIATION USING DUAL-POLARIZED NANOANTENNAS

ENERGY HARVESTING OF INFRARED RADIATION USING DUAL-POALRIZED NANOANTENNAS

By

Rishad Arfin, B.Sc.

Electrical & Electronic Engineering Department

Islamic University of Technology (IUT), Bangladesh.

A Thesis

Submitted to the School of Graduate Studies

In Partial Fulfilment of the Requirements

For the Degree

Master of Applied Science

McMaster University

MASTER OF APPLIED SCIENCE (2017) McMaster University

(Electrical and Computer Engineering) Hamilton, Ontario, Canada

TITLE : Energy Harvesting of Infrared Radiation Using Dual-Polarized Nanoantennas.

AUTHOR : Rishad Arfin, B.Sc. (Electrical & Electronic Engineering)
Islamic University of Technology (IUT), Bangladesh.

SUPERVISOR : Dr. Mohamed Bakr
Department of Electrical & Computer Engineering
McMaster University

CO-SUPERVISOR(S) : Dr. Matiar R. Howlader
Department of Electrical & Computer Engineering
McMaster University

Dr. Shirook Ali
McMaster University

NUMBER OF PAGES : xviii, 153.

Abstract

In this research work, we propose a novel energy harvester which converts solar electromagnetic radiation into DC energy at infrared regime. The proposed device consists of a dual polarized nanoantenna loaded with an anisotropic material at its gap. The dual polarized nanoantenna focuses the randomly polarized radiation into its gap resulting in high electric field. This high local electric field at the gap interacts with the anisotropic material. In our proposed design, the anisotropic material possesses nonlinear electrical conductivity and converts the dual polarizations at the gap into a DC voltage difference across the terminals of the nanoantenna. The novelty of our proposed design is in the rectification of the electromagnetic radiation without utilizing a diode. The theory of the energy harvester depends on the utilization of the dual polarized nanoantennas at high frequency regime. Therefore, we carry out a parametric study to investigate the resonance characteristic of the dual polarized nanoantenna. In addition, we investigate the effect of the geometrical parameters on the local field enhancement at the gap of the dual polarized nanoantenna. Also, another parametric study is carried out to determine the effect of the governing parameters of the anisotropic material on the generated DC voltage across the harvester. Our approach is illustrated through electromagnetic simulations.

Acknowledgement

First and foremost, I would like to express my deepest gratitude to my supervisor Dr. Mohamed Bakr for his relentless guidance, wise suggestions and excellent supervision at all stages of this thesis work. I am thankful to him for giving me the opportunity to be a part of Computational Electromagnetic Research Laboratory (CERL) at McMaster University with a comfortable research environment.

Additionally, I would like to express my sincere gratitude to my proactive co-supervisors Dr. Matiar R. Howlader and Dr. Shirook Ali. I would like to thank them for their constructive suggestions in every meeting for the last two years. This thesis would not have been possible without their utmost cooperation and encouragement.

I highly would like to extend my appreciation to my colleague and a PhD student at McMaster University, Ahmed Elsharabasy, for his altruistic assistance with wise suggestions at different stages of this thesis work. Without his kind help, the interesting results that are presented in this thesis would have been very difficult for me.

I would like to extend my special thanks to Dr. Jamal Deen for all his help and suggestions with the selection of anisotropic material that will lead to feasible fabrication of the novel device.

Finally, I would like to thank my caring mother, Nilufar Sultana, for her continuous support and encouragement during my study in Canada. I would like to thank my wife, Shamanta Sharmin Shithi, for being understandable and patient enough to be away from

me throughout my study. None of this would have been possible without their endless love and sacrifice over years.

Although, I have given my best effort to complete this thesis paper, I, humbly, seek you kind apologies for any kind of mistake that I have committed in this report.

Table of Contents

Abstract.....i

Acknowledgement.....ii

Table of Contents.....iv

List of Figures.....viii

List of Tables.....xvi

List of Acronyms.....xvii

List of Variables & Constants.....xviii

CHAPTER 1.....1

1. Introduction.....1

1.1 Solar Energy & Solar Spectrum.....2

1.2 Solar Energy Harvesting Techniques.....3

1.2.1 Photovoltaic (PV) Solar Cells.....3

1.2.2 Concentrated Solar Power (CSP) Cells.....5

1.2.3 Photo Bio-Electrochemical Cell.....6

1.3 Limitations & Challenges.....7

1.3.1 Limitations of Solar Cells.....8

1.3.2 Limitations of Concentrated Solar Power Cell.....8

1.3.3 Limitations of Photo Bio-Electrochemical Cell 9

1.4 Rectennas for Energy Harvesting 9

1.4.1 Rectennas 10

1.4.2 Rectennas Technology 10

1.4.3 Operation Principle of Rectennas 11

1.4.4 Advantages of Rectennas 12

1.4.5 Challenges & Fundamental Limitations 13

1.5 Objectives 14

1.6 Thesis Organization 15

CHAPTER 2 16

2. Background 16

2.1 History of Solar Rectenna 17

2.2 Microwave Rectennas 19

2.3 Optical Nanoantenna 21

2.3.1 Drude Model 23

2.3.2 Limitation of Drude Model 29

2.3.3 Reflectivity & Conductivity in Metal 33

2.3.4 Surface Plasmon (SP) 36

2.3.5. Applications of Optical Nanoantenna 41

2.4. Rectifiers for Nanoantennas 46

2.4.1. Physical Interpretation of Quantum Tunneling 46

2.4.2. Tunnel Diodes 48

2.4.3. Metal-Insulator-Metal (MIM) Diode 54

2.5 Coupling Efficiency of Rectenna 57

2.6 Recent Development on Rectennas 62

2.7 Fundamental Limitation of MIM Diodes 77

CHAPTER 3 81

3. Parameterization of Dual Polarized Nanoantenna 81

3.1. Operation Principle of Bowtie Nanoantenna 83

3.2. Dual Polarized Cross Bowtie Nanoantenna 89

3.3. Comparison of Local Field Enhancement at the Gap 92

3.4. Parametric Studies of Dual Polarized Cross Bowtie Nanoantenna 95

3.4.1 Gap-Size 95

3.4.2. Length 96

3.4.3. Width 98

3.4.4. Tip-Shape 99

CHAPTER 4 102

4. The Novel Approach 102

4.1. Novel Energy Harvester 102

4.2 Conductivity Tensor of Anisotropic Material 105

4.3 Proof of Concept 106

4.4 Simulation Setup in COMSOL Multiphysics 108

4.4.1. Time Domain Modeling in COMSOL 108

4.4.2. Geometries and Dimensions 109

4.4.3. Boundary Conditions 111

4.4.4. Defining Materials 113

4.4.5. Mesh 114

4.5. Parameterization of Anisotropic Material & Simulation Results 116

4.6. Choice of Anisotropic Material 135

4.7. Optimization of Generated Voltage 136

4.8. Array Configuration of Energy Harvester 139

CHAPTER 5 140

5.1 Conclusion 140

5.2 Future Works 141

References 143

List of Figures

Figure 1.1: Solar energy distribution over the broad spectrum from infrared (IR) to ultraviolet (UV) [2]. 2

Figure 1.2: Photon absorption in a semiconductor based PV solar cell. 4

Figure 1.3: Solar energy harvesting using concentrating solar power technology [3]. 5

Figure 1.4: Conversion of solar energy into electrical power using photo-bio electrochemical cells: Assembly of electrically wired PSI/enzyme photo-electrochemical electrode [5]. 6

Figure 1.5: Schematic diagram of the rectenna [15]. 12

Figure 2.1: The real and imaginary part of the relative permittivity of the metal for $\gamma = \frac{\omega_p}{4}$ [40]. 28

Figure 2.2: Relative permittivity εr of Silver using Drude model at the optical regime. For Silver, ε_∞= 3.36, ω_p= $1.33 \times 10^{16}\ s^{-1}$ and γ =$7.075 \times 10^{13}\ s^{-1}$ [40]. 29

Figure 2.3: Experimental reflectivity of Aluminum (Al) as a function of photon energy, copyright@ American Physical Society [39]. 30

Figure 2.4: (a) Direct transition, (b) and indirect transition between the valence band and the conduction band. 31

Figure 2.5: Energy band diagram of Aluminum (Al), copyright@ American Physical Society [39]. 32

Figure 2.6: Reflectivity of metal as a function of frequency [39]. 34

Figure 2.7: Surface Plasmons at the interface between metal and dielectric material [44]. 37

Figure 2.8: Field penetration decays exponentially in both metal and dielectric medium [44]. 39

Figure 2.9: Excitation spectra changes with the size of the nanoparticles. The increase in the size of the nanoparticles leads to broader spectrum and redshift in the resonance (left). SEM images of the Silver nanoparticles (right) [43]. 40

Figure 2.10: Local field enhancement at the gap, tips, and around edges of the bowtie nanoantenna. 41

Figure 2.11: (a) Light trapping by using metallic nanoparticle in the solar cell. (b) Light trapping by embedding metallic nanoparticles as nanoantennas in the solar cell. (c) Light trapping by embedding metal film on the back surface of the photovoltaic absorber layer [50]. 43

Figure 2.12: A near field probe based on bowtie (right) has a better signal to noise ratio than classical rounded aperture (left) [50]. 45

Figure 2.13: Quantum mechanical tunneling a particle through the potential barrier. 47

Figure 2.14: Degenerately doped semiconductor at thermal equilibrium. 49

Figure 2.15: (a) Tunneling current due to forward bias. (b) Tunneling current increases with the increase in the forward bias (since depletion region decreases). 50

Figure 2.16: (a) Tunneling current due applied forward bias. (b) Tunneling current increases due to increase in the forward bias and creating holes in n-type. (c) Tunneling

current decreases since a number of electrons in n-type decrease (differential negative resistance). 51

Figure 2.17: Diffusion current flows through the potential barrier. 52

Figure 2.18: Tunneling current in forward bias direction subdivided into three regions. 53

Figure 2.19: Tunneling current for reverse bias voltage. 53

Figure 2.20: Physical structure of Metal-Insulator-Metal (MIM) diode. 54

Figure 2.21: Energy band diagram of a MIM diode. 55

Figure 2.22: (a) Band diagram of MIM diode with a negative bias voltage. (b) Band diagram of MIM diode with further increase in the applied voltage. Tunneling current gets higher due to the decrease in effective thickness of the insulator. 56

Figure 2.23: The Small signal model of rectenna. The antenna is designed as a voltage source with series resistance and the diode is modeled as parallel *RC* circuit [58]. 58

Figure 2.24: Coupling efficiency of the antenna to the diode as a function of diode edge for R_A= 377Ω [56], [13]. R_p is defined as the equivalent resistance of $(R_A \,||\, R_D)$. 59

Figure 2.25 : Coupling efficiency of the antenna to the diode as a function of diode edge for R_A=10 kΩ [56], [13]. R_p is defined as the equivalent resistance of $(R_A \,||\, R_D)$. 60

Figure 2.26: Different structure of nanoantennas (a) Dipole (b) Bowtie (c) Spiral..... 63

Figure 2.27: (a) Gold dipole nanoantenna incorporated with MIM diode, overlapping (red area) indicates the diode [61]. (b) Antenna integrated with Traveling Wave (TW) MIM diode [62]. (c) Vertical Coupled Strip (VCS) and Lateral Coupled Strips (LCS), blue arrow shows the decay length [7]. 66

Figure 2.28: (a) Misaligned bowtie nanoantenna on Si substrate [63]. (b) Gold nanoantenna on chromium adhesion layer. SiO_2 is employed on the Si substrate as a matching section. Gold at the bottom of the substrate is working as a good reflector. The black arrow indicates the reflective wave, green arrows indicate the coupled wave and red arrows indicate the incident waves on the matching section [17]. 72

Figure 2.29: (a) SEM images for the overlapped bowtie with 2.7 μm arm length and 50° flare angle [64]. (b) The design of a sector bowtie nanoantenna incorporated with Au-TiO_x-Ti (MIM) diode [65]. 73

Figure 2.30: (a) Structure of inverse arrowhead geometric diode, the dimension of the neck region i.e. d_{neck} = 75 nm, is in the scale of the MFPL for the charge carriers, and $d_{shoulder}$ = 1μm. (b) AFM image of the fabricated graphene geometric diode. The thickness of the graphene between the two metal contacts is around 0.5 nm to 1 nm [66].....74

Figure 2.31: Structure of (a) Log Periodic Spiral Nanoantenna [67]. (b) Square Spiral Nanoantenna [67]. (c) Archimedean Spiral Nanoantenna [67]. (d) Square Spiral incorporated with Au-TiO_x-Ti (MIM) diode where a = 300 nm, b = 1μm, h= 100 nm and d = 5 nm [68]. 76

Figure 2.32: Top view of (a) Crescent nanoantenna with inner circular patch, D_{in} = 430 nm and D_{out} = 670 nm [69]. (b) Crescent nanoantenna with inner elliptical patch, major axis for outer and inner ellipse is 670 nm and 430 nm [70]. 77

Figure 3.1: Structure of a regular bowtie nanoantenna (a) side view (b) top view.....84

Figure 3.2: Local field enhancement at the gap of the bowtie nanoantenna for L = 1.0 μm, d = 1.0 μm, and G = 50 nm. 86

Figure 3.3: Intensity of the local field enhancement at the gap of the bowtie nanoantenna for L = 1.0 μm, d = 1.0 μm, and G = 50 nm. 87

Figure 3.4: Local field enhancement at the gap for different shapes of nanoantenna; top view of (a) Dipole (b) Bowtie (c) Rounded-Bowtie (d) Cross Bowtie (e) Cross Rounded-Bowtie [73]. 88

Figure 3.5: Structure of dual polarized cross bowtie nanoantenna (a) side view (b) top view. 89

Figure 3.6: Local field enhancement at the gap of the dual polarized cross bowtie nanoantenna for L = 1.0 μm, d =1.0 μm, and G = 50 nm. 91

Figure 3.7: Intensity of the local field enhancement at the gap of the dual polarized cross bowtie nanoantenna for L = 1.0 μm, d = 1.0 μm, and G = 50 nm. 92

Figure 3.8: Comparison of local field enhancement at the gap for single polarized bowtie and dual polarized cross bowtie nanoantenna for L =1.0 μm, d =1.0 μm, and G = 50 nm. 93

Figure 3.9: Comparison of local field intensity at the gap for single polarized bowtie and dual polarized cross bowtie nanoantenna for L = 1.0 μm, d = 1.0 μm, and G = 50 nm. ... 94

Figure 3.10: Variation in the local field enhancement with the change in the gap-size G of the cross bowtie nanoantenna. 96

Figure 3.11: Local field enhancement at the gap of the dual polarized cross bowtie nanoantenna for different values of length L. 97

Figure 3.12: Local field enhancement at the gap of the dual polarized cross bowtie nanoantenna for different values of width *d*. 98

Figure 3.13: Variation in the local field enhancement with the change in the tip-shape of the cross bowtie nanoantenna. 100

Figure 4.1: Dual polarized cross bowtie nanoantenna loaded with an anisotropic material in its gap. 103

Figure 4.2: Orthogonally polarized (E_x,E_y) light wave illuminates perpendicularly (along z-axis) on the surface of the cross bowtie nanoantenna. 104

Figure 4.3: Our proposed novel energy harvester with design parameters (top view). .. 110

Figure 4.4: Scattering boundary condition (SBC) for the time-domain modeling. 111

Figure 4.5: PEC and PMC setup for 3D simulation, if EM wave is only (a) *x*-polarized (b) *y*-polarized. 112

Figure 4.6: Realization of PEC and PMC setup for (a) dual polarized plane wave (b) proposed design. 113

Figure 4.7: (a) PEC and (b) PMC setup in 3D simulation. 114

Figure 4.8: 3D Mesh of our proposed model in time-domain simulation. 115

Figure 4.9: Electric field (E_x,E_y) at the gap for σ_{xxo} = 2.5 $\times 10^{-3}$ S/m and α = 0.04.. 117

Figure 4.10: Normalized field at the gap for σ_{xxo} = 2.5 $\times 10^{-3}$ S/m and α = 0.04. 118

Figure 4.11: Electric field (E_x,E_y) at the gap for σ_{xxo} = 2.5 $\times 10^{-3}$ S/m and α = 0.40. 119

Figure 4.12: Normalized field at the gap for σ_{xxo} = 2.5 $\times 10^{-3}$ S/m and α = 0.40. 119

Figure 4.13: Electric field (E_x,E_y) at the gap for σ_{xxo} = 2.5 × 10 S/m and α = 0.04..120

Figure 4.14: Normalized field at the gap for σ_{xxo} = 2.5 × 10 S/m and α = 0.04. 121

Figure 4.15: Electric field (E_x,E_y) at the gap for σ_{xxo} = 2.5 × 10^2 S/m and α = 0.04. 122

Figure 4.16: Normalized field at the gap for σ_{xxo} = 2.5 × 10^2 S/m and α = 0.04.....122

Figure 4.17: Electric field (E_x,E_y) at the gap for σ_{xxo} = 2.5 × 10^3 S/m and α = 0.01. 123

Figure 4.18: Normalized field at the gap for σ_{xxo} = 2.5 × 10^3 S/m and α = 0.01.....124

Figure 4.19: Electric field (E_x,E_y) at the gap for σ_{xxo} = 2.5 × 10^3 S/m and α = 0.02. 125

Figure 4.20: Normalized field at the gap for σ_{xxo} = 2.5 × 10^3 S/m and α = 0.02.....125

Figure 4.21: Electric field (E_x,E_y) at the gap for σ_{xxo} = 2.5 × 10^3 S/m and α = 0.03. 126

Figure 4.22: Normalized field at the gap for σ_{xxo} = 2.5 × 10^3 S/m and α = 0.03.....127

Figure 4.23: Electric field (E_x,E_y) at the gap for σ_{xxo} = 2.5 × 10^3 S/m and α = 0.04. 128

Figure 4.24: Normalized field at the gap for σ_{xxo} = 2.5 × 10^3 S/m and α = 0.04.....128

Figure 4.25: Electric field (E_x,E_y) at the gap for σ_{xxo} = 2.5 × 10^3 S/m and α = 0.05. 129

Figure 4.26: Normalized field at the gap for σ_{xxo} = 2.5 × 10^3 S/m and α = 0.05.....130

Figure 4.27: Electric field (E_x,E_y) at the gap for σ_{xxo} = 2.5 × 10^4 S/m and α = 0.01. 131

Figure 4.28: Normalized field at the gap for σ_{xxo} = 2.5 × 10^4 S/m and α = 0.01.....131

Figure 4.29: Electric field (E_x,E_y) at the gap for σ_{xxo} = 2.5 × 10^4 S/m and α = 0.04. 132

Figure 4.30: Normalized field at the gap for σ_{xxo} = 2.5 × 10^4 S/m and α = 0.04.....133

Figure 4.31: Generated voltage for different values of DC conductivity σ_{xxo} at fixed α = 0.04.....134

Figure 4.32: Generated voltage for different values of the nonlinear conductivity coefficient α at a fixed σ_{xxo} = 2.5 ×10^3 S/m. 135

Figure 4.33: Optimization of the generated voltage by changing the spatial orientation of the anisotropic material at the gap. 137

Figure 4.34: Isometric view of parallel array configuration of energy harvester……..138

Figure 4.35: Top view of series array configuration of energy harvester……..139

List of Tables

Table 2.1: Key events of the rectenna device [16].....18

Table 2.2: Different types of nanoantennas in the optical range 62

Table 2.3: Rectenna based on dipole nanoantenna for IR energy harvesting.....64

Table 2.4: Rectenna based on bowtie nanoantenna for IR energy harvesting 67

Table 2.5: Rectenna based on spiral nanoantenna for IR energy harvesting 70

Table 2.6: Recent development of crescent nanoantenna.....75

Table 3.1: Dimensions for the bowtie nanoantenna.....85

Table 3.2: Drude-parameters for gold.....85

Table 3.3: Dimensions for the cross bowtie nanoantenna 90

Table 3.4: Design parameters for tip-shape 99

Table 4.1: Design parameters of the proposed model.....110

Table 4.2: Values of σ_{xxo} and α.....116

List of Acronyms

TW	Terawatt
IR	Infrared
UV	Ultra-Violet
nm	Nanometer
CSP	Concentrated Solar Power
PV	Photovoltaic
PSI	Photo-System I
CNT	Carbon Nano-Tube
EM	Electromagnetic
GHz	Gigahertz
THz	Terahertz
fs	Femtoseconds
eV	Electron Volt
MIM	Metal-Insulator-Metal
SPP	Surface Plasmon Polariton
PEC	Perfect Electric Conductor
PMC	Perfect Magnetic Conductor
SBC	Scattering Boundary Condition
FEM	Finite Element Modeling
LSPR	Localized Surface Plasmon Resonance
TW	Travelling Wave
MOM	Metal Oxide Metal
MFPL	Mean Free Path Length

List of Variables & Constants

F_{acc}	Acceleration Force
m	Mass of an electron
r	Displacement
F_d	Damping force
q	Charge of an electron
E	Electric field
D	Electric field density
χ	Susceptibility
ε_r	Relative permittivity of metal
ω_p	Plasma frequency
ε_1, ε_2	Real & Imaginary part of relative permittivity
γ	Damping frequency
$\hbar$	Plank constant divided by 2π
n_c, R	Complex refractive index, Reflection
k	Extinction Coefficient
J	Current density
δ_m,δ_d	Propagation decay length in metal & dielectric
R_A	Resistance of the antenna
R_D	Resistance of the diode
C_D	Capacitance of the diode
σ_{xxo}	DC conductivity of the anisotropic material
$\boldsymbol{\alpha}$	Nonlinear Conductivity Coefficient
L, d	Length and width of the bowtie nanoantenna
G	Gap-size
t	Thickness of the bowtie nanoantenna

CHAPTER 1

1. Introduction

The ever increasing demands of the energy across the world and limited conventional energy sources suggest the need for a new sustainable paradigm for energy harvesting. Sufficient supplies of energy are inherently related to global stability, economic development and quality of life. The balance in supply and demand of the energy ensures global development in every sphere of human activity. Some of the sources of energy like solar, wind, and ocean have existed since the prehistoric times till today. Some others like fossil fuels e.g. oil, natural gas, and coals have been employed to meet the energy demand to a great extent. Unfortunately, these fossil fuels are non-renewable sources and they are expected to experience progressive depletion over the next few decades. Therefore, the science community is investigating extensively for an alternative reliable epitome to satisfy the unprecedented demand for energy.

Electromagnetic radiation is a new promising alternative source which can potentially contribute to solve the global energy demand. Apart from the electromagnetic radiation from the sun, the infrared radiation from any heated object such as the dissipated heat from the earth's surface can also be employed to harvest energy.

1.1 Solar Energy & Solar Spectrum

Solar energy is considered to be an infinite reservoir of clean energy. The sun deposits 120,000 TW of radiation on the earth's surface whereas at present the continuous power consumption of world is 13 TW per year [1]. The energy from the sun arrives on the surface of the earth as electromagnetic radiation and gets distributed across the color spectrum from infrared (IR) to ultraviolet (UV).

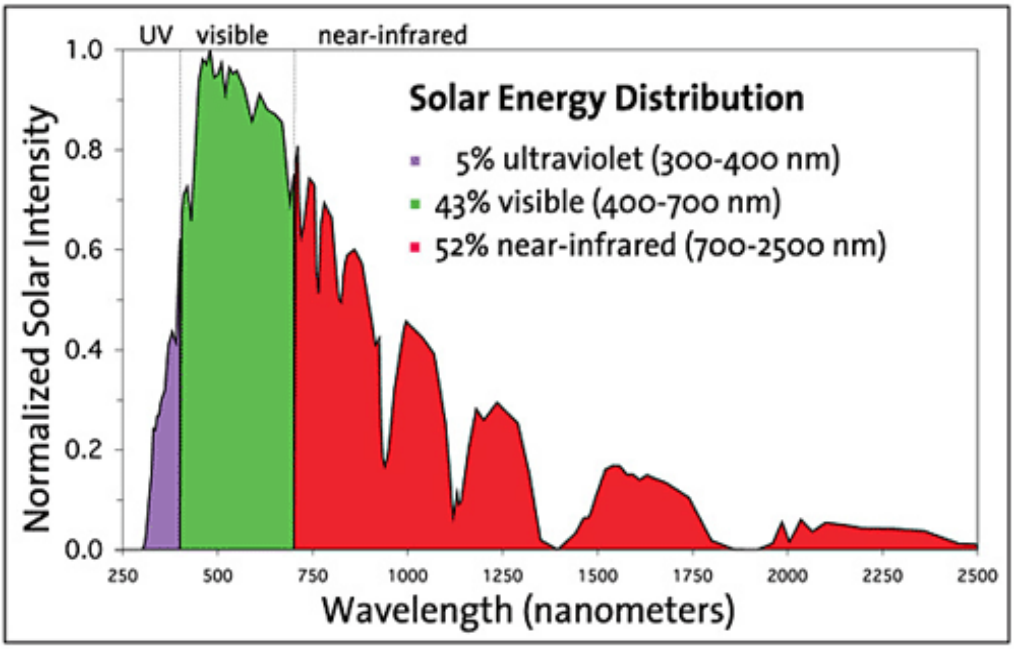

Figure 1.1: Solar energy distribution over the broad spectrum from infrared (IR) to ultraviolet (UV) [2].

The average solar intensity that reaches the earth surface is 1368 W/m^2 [2]. Most of this solar energy is highly concentrated in the visible spectrum, wavelength ranging from 400 nm to 700 nm. In contrast, a small portion of energy is distributed over ultraviolet (UV),

wavelength ranging from 300 nm to 400 nm, and infrared (IR), wavelength ranging from 700 nm to 2500 nm, as shown in Fig. 1.1. Unfortunately, this solar energy is not fully or even partially utilized as the primary source of energy. However, it is clear that, if the solar energy can be exploited on an adjustable scale, it can be a promising alternative source to meet the global energy demand.

1.2 Solar Energy Harvesting Techniques

All the techniques for solar energy utilization include the functional steps of absorption, conversion, and storage. Many recent research and development efforts focus on improving the ability to harvest, store, and distribute solar energy. The solar energy can be transformed into other forms of energy such as electricity or heat. Currently, there are different kinds of techniques to utilize and harvest solar energy. The different techniques for harnessing solar energy have been listed as follows:

- Photovoltaic (PV) solar cells.
- Concentrated Solar Power (CSP) cells.
- Photo bio-electrochemical cells.

1.2.1 Photovoltaic (PV) Solar Cells

Photovoltaic (PV) solar cells are the most ubiquitous and mature solar harvesting technology. It converts the incident electromagnetic radiation directly into electrical energy by using semiconductor-based PN junction where the conversion mechanism is

based on photon-electron interactions. Generally, a PV cell consists of light-absorber that only absorbs photon above a threshold energy level, as shown in Fig. 1.2. The threshold energy level is defined as bandgap, i.e. the energy difference between conduction and valence band, which entirely depends on the properties of the material.

The material becomes transparent for the photons with energies less than the bandgap. On the other hand, for photons with energies higher than the bandgap, it becomes an absorber. When a photon is absorbed and interacts with an electron in the valence band of the semiconductor, the energy of the photon is absorbed by the electron. Consequently, the electron gets promoted in the conduction band, leaving a hole in the valence band, as shown in Fig.1.2. This is called the photo-generation of an electron-hole pair. The electron-hole pair is then driven by the electric field in the depletion zone of the PN junction which results in photovoltage and photocurrent.

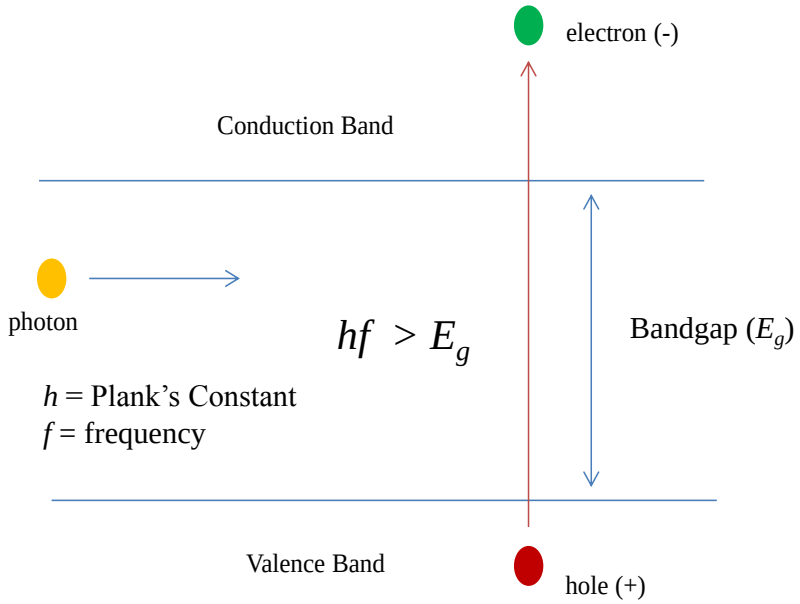

Figure 1.2: Photon absorption in a semiconductor based PV solar cell.

Most of the PV cells are made of semiconductor-based inorganic materials, e.g. Silicon (Si), which has the ability to absorb sunlight and creates electrical energy in the external circuit. The electrical energy, i.e. photovoltage and photocurrent, generated from the PV solar cells are dc in nature.

1.2.2 Concentrated Solar Power (CSP) Cells

Concentrated Solar Power (CSP) is one of the other techniques, which converts solar energy into heat or thermal energy. The energy harvesting process of CSP is quite different from PV technology.

Figure 1.3: Solar energy harvesting using concentrating solar power technology [3].

The incident electromagnetic radiation from the sun is concentrated at a single point using lens or mirror, as shown in Fig. 1.3. This highly concentrated energy is then used to heat or boil water which produces steam. The steam then drives the turbine and generates the electrical power in the similar way as conventional power plants do.

1.2.3 Photo Bio-Electrochemical Cell

Photosynthesis is a process which converts sunlight energy into chemical energy of various organic compounds. The conversion efficiency of a photosynthesis process is very high and close to 100% [4]. Therefore, photosynthesis has come to the attention of many researchers who are looking for an alternative energy source for energy harvesting.

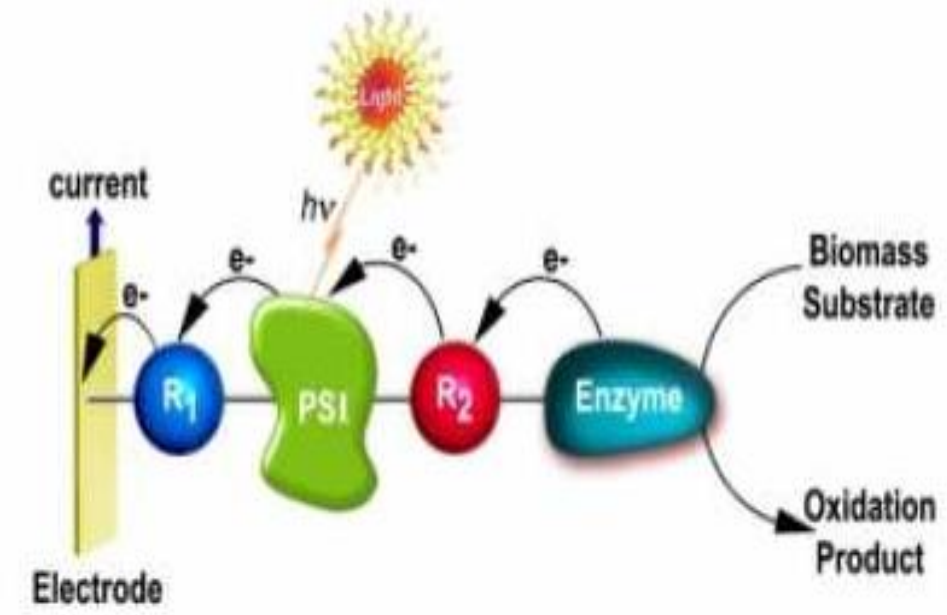

Figure 1.4: Conversion of solar energy into electrical power using photo-bio electrochemical cells: Assembly of electrically wired PSI/enzyme photo-electrochemical electrode [5].

The photo bio-electrochemical cell based on native photosynthetic reaction, photosystem I (PSI), is one of the recent techniques which convert the solar energy into electrical power [5]. This native photosynthetic reaction acts as functional nanostructures for the assembly of photo bio-electrochemical cells. The system provides a standard prototype which employs the native photosynthetic apparatus for the conversion of solar energy into electrical power using biomass substrate as fuel. As shown in Fig.1.4, the system consists of modified integrated electrodes that include the natural photosynthetic reaction center. The native proteins are electrically wired by the means of chemical electron transfer mediators. Photo irradiation to the electrodes results in electrical power while oxidizing the glucose acts as fuel.

In this system, the photoexcitation of photosystem I (PSI) results in electron transfer to the electrical wiring unit. Different methodologies have been developed to establish a contact electrically between photosystems and electrodes. Fig. 1.4 shows, the reconstitution of the photosystem on diffusional relay units. Efficient electrical wiring between the electrode and the photosynthetic reaction center leads to the generation of photocurrent.

1.3 Limitations & Challenges

There are some limitations and challenges involved with each of the energy harvesting techniques. The limitations corresponding to each of the techniques are briefly discussed as follows:

1.3.1 Limitations of Solar Cells

- One of the major limitations of solar cells is low conversion efficiency. The theoretical limit of the conversion efficiency is around 41% for single junction solar cells [6].
- The utilization of the solar cells is limited to the bandgap of the material. Most of the PV solar cells are based on Silicon (Si) which has a bandgap of 1.1 eV at room temperature. As a consequence, Si-based PV cells cannot absorb energy that is less than 1.1 eV.
- PV solar cells are highly sensitive to weather condition and cannot operate at night.
- In addition to that, optimization of the output energy of the PV solar cells requires expensive mechanical tracking system.

1.3.2 Limitations of Concentrated Solar Power Cell

- Concentrated Solar Power (CSP) technology is expensive compared to PV technology because it requires more space and storage systems for large-scale installations.
- Unlike PV cell, CSP technology requires suitable places to be installed since it needs a high amount of solar radiation to generate electricity. They mostly can be built in deserts or large land areas.

1.3.3 Limitations of Photo Bio-Electrochemical Cell

- The stabilities of the photosystem are limited upon their elimination to the native environment.
- Despite the developments of different methodologies to establish contact electrically between photosystems and electrodes, the electrical contact requires further improvement. The maximum current density in a cell can be obtained by modeling a system which requires no mediator to transfer electrons from photosystem to electrode rather it transfers electrons directly. The electrons lose some of their energies if they are transferred through a mediator. [4]
- To improve the efficiency of the photo bio-electrochemical cells, traditionally, the surface area of the electrode is increased. The modification can also be employed in the electrodes by using materials which have large surface area i.e. nanomaterials.

1.4 Rectennas for Energy Harvesting

The incident radiation that reaches the earth's surface can be both in the visible and infrared regime. Approximately, 70 % of this radiation energy is absorbed by the earth's surface and re-emitted as infrared radiation (IR) in the wavelength ranging from 8 μm to 14 μm with a peak wavelength of around 10 μm [7]–[9]. Recent researches aim to exploit the IR energy, which is abundantly available in the environment as a reliable potential source of green energy, by using a sub-wavelength device called 'Rectenna'.

1.4.1 Rectennas

The word 'Rectenna' means **Rect**ifying-Ant**enna**. A successful incorporation of the antenna to the rectifier that allows the energy conversion of free propagating electromagnetic radiation into dc electricity is called '*Rectenna*'; an idea which was originally proposed by Bailey [10]. Therefore, rectenna technology is based on the combined operation of two fundamental elements: an electromagnetic antenna followed by an electrical rectifier. Unlike PV technology, the physics of rectenna does not require quantum mechanics to explain the interaction between the antenna and electromagnetic waves. Since the electrons in the metal antenna are already in the conduction band, they do not require any photon-energy. In contrast to the solar cells, the generated voltage of the antenna is AC in nature. Therefore, it requires basic element such as rectifier to convert AC into DC output before supplying to the load.

1.4.2 Rectennas Technology

Rectenna technology involves rectennas that operate at different frequency regimes. There is radio frequency (RF) rectenna which consists of an antenna that operates at microwave or radio frequency regime followed by a fast-switching diode [11] to provide the dc output to the load. Traditionally, the dimension of the antenna for microwave regime varies linearly [12] with the wavelength.

Optical rectenna [13] is considered to be another form of rectenna technology which involves antenna that operates at optical regime such as THz, infrared, and visible regime.

Since the antenna operates in the high-frequency regime, the dimension of the antenna becomes small in size i.e. nano. Therefore, antennas operating at optical regime are called optical nanoantennas. Unlike microwave antenna, the dimension of the optical nanoantenna does not vary linearly with wavelength [12]. The frequency of the generated voltage in the optical nanoantenna is very high. Therefore, it requires the incorporation of a rectifier which works based on quantum tunneling.

Since the antenna element and the rectifier at optical regime do not have the scalable properties of the RF counterpart; therefore, the optical rectenna cannot be considered as an extrapolation of RF rectenna concept to the optical range.

1.4.3 Operation Principle of Rectennas

The operation principle of the rectenna model, shown in Fig. 1.5, can be discussed based on the interaction of the electromagnetic (EM) waves to the electrons on the surface of the metal antenna. The antenna receives the incident electromagnetic (EM) waves and converts the EM waves into localized electric field [14]. This localized energy creates a high frequency oscillating electrical current which gets rectified (by the rectifier) and flows to the resistive load. The low pass filter, shown in the schematic diagram, provides the impedance matching between the receiving antenna and the rectifier. It also blocks the higher order harmonics generated by the rectifier from being reradiated by the antenna [15]. A dc pass filter is required to smooth the signal before going to the resistive load.

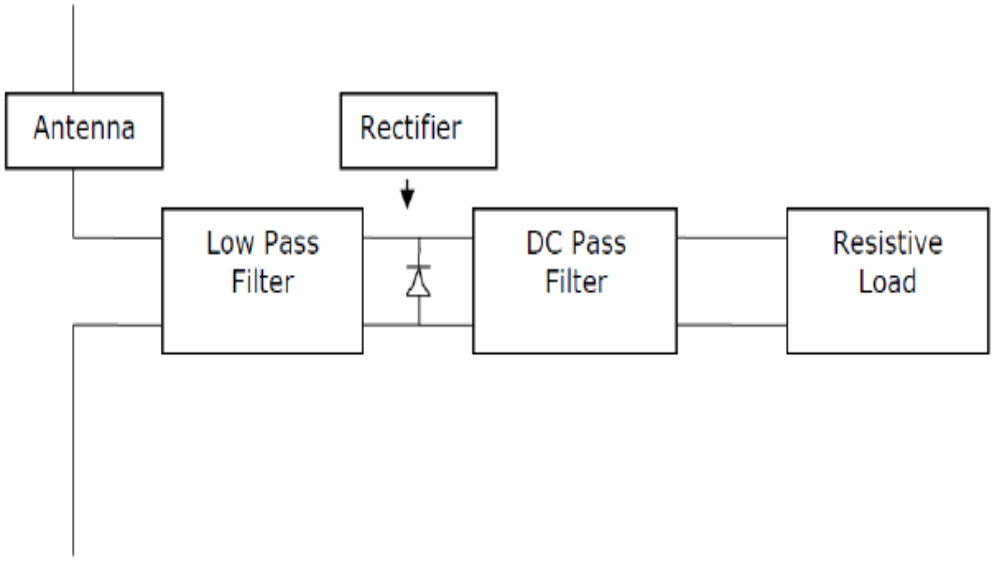

Figure 1.5: Schematic diagram of the rectenna [15].

1.4.4 Advantages of Rectennas

Nowadays, the space in the urban and suburb areas, including the work and home environment are densely packed with electromagnetic waves of different regimes (e.g. radio waves, infrared waves). The ubiquitous presence of the radio, TV, cell phones, and other personal devices produce a non-negligible amount of EM energy propagating around us. This form of propagating EM energy can be harvested properly into the electronic system which requires ultra-low power to operate. The advantages of energy harvesting by using rectennas have been listed as follows:

- Theoretical conversion efficiency is 100%. Rectenna used for microwave regime has a conversion efficiency of 90% [16].

- Insensitive to weather condition and can also operate at night. Unlike PV cells, rectennas are able to operate in any weather conditions such as humid or cloudy climate.
- The operation of the rectennas is not restricted to bandgap. Rectennas are able to operate in IR regime which is not only limited to the sun rather it includes all the radiated heat from the industrial product, human body and earth's surface.

1.4.5 Challenges & Fundamental Limitations

Optical rectenna i.e. nanoantenna incorporated with rectifier can be effectively employed to harvest energy at high-frequency regime (e.g. THz, infrared, and visible range). Unfortunately, the efficiencies obtained for microwave rectennas have not been replicated at infrared and visible regime [6]. This is mostly due to the inherent properties of the material at high frequency e.g. metals are dispersive and not perfect conductor at high frequency. There are some fundamental challenges and limitations involved with optical rectennas which limit the efficiency. They are mentioned briefly as follows:

- One of the major challenges involved with the THz or infrared rectennas is the rectification process [17]. In order to perform rectification at the high-frequency regime, the RC time constant of the diode has to be on the scale of a femtosecond.
- Efficient rectification depends on the impedance matching between the antenna and the rectifier [17]. In essence, a diode with high resistance provides good

rectification. However, the resistance of the nanoantenna is very small, typically around few hundreds of ohms. Therefore, impedance matching becomes an ambitious problem.

- Very thin layer of insulator and small junction area of the diode result in both small resistance (R) and capacitance (C). However, the realization of a small contact area and the thin insulator layer is often very challenging in the fabrication process.

A detailed discussion of the challenges and limitations of the rectenna has been carried out in the next chapter.

1.5 Objectives

- Conducting a theoretical study for surface waves propagation at the metal-dielectric interface.
- Conducting a study on the rectifiers of the optical rectennas.
- Study on the recent development of optical rectennas for energy harvesting.
- Conducting a parametric study of cross bowtie nanoantenna for energy harvesting at the THz regime.
- A novel theoretical approach to perform rectification at high frequency, i.e. THz regime, without the physical incorporation of a rectifier. Our novel energy harvester

consists of a dual polarized nanoantenna loaded with an anisotropic material at its gap.

1.6 Thesis Organization

- **CHAPTER 2** of the report gives a historical overview of the rectennas technology at microwave and optical regime. It also focuses on the rectifier i.e. Metal Insulator Metal (MIM) diode, which operates at high-frequency regime. This chapter also provides a brief review of the recent development of the optical rectennas.

- **CHAPTER 3** emphases on the parametric study of a dual polarized cross bowtie nanoantenna. For instance, it discusses the effect of different geometrical parameters on the local field enhancement at the gap of the cross bowtie nanoantenna.

- **CHAPTER 4** proposes a novel technique to perform rectification at high-frequency regime without the physical realization of a rectifier or diode. The proposed design consists of a cross bowtie nanoantenna loaded with an anisotropic material at the gap.

- **CHAPTER 5** finally presents the overall findings in the conclusion and discusses the future works.

CHAPTER 2

2. Background

Fundamentally, solar cells and rectennas are similar since there is absorption of light energy to produce electricity. However, there is a substantial difference in their operational mechanism which relies on the wave-particle duality of light. Solar cells are semiconductor-based devices in which light is perceived as a particle (e.g. absorption of photons) form, whereas the concept of rectenna devices is entirely based on the wave nature of light [18] [19].

Since the absorption of photons in the solar cells is limited by the bandgap of the material, the efficiency of single-junction and multi-junction solar cells is around 30% and 55% respectively [20]. The light energy in solar cells is lost primarily in two ways:

- Low energy photons pass through the material.
- High energy photons cause heat loss.

Due to the limited efficiency of the PV solar cells, an alternative approach i.e. rectenna device is becoming increasingly attractive for solar energy harvesting application. This chapter presents the history of this 40-year old device concept and describes the operational mechanism of the rectenna device. It also explains the role of the new physics i.e. Surface Plasmon Polariton (SPP) for the rectenna device which operates in the high-frequency regime. Finally, the chapter provides the state-of-art

research and some recent developments of rectennas and its two main components i.e. antenna and rectifier.

2.1 History of Solar Rectenna

The rectenna concept was initially proposed by William C. Brown in 1960 [21] for wireless power transmission. Wireless power transmission was not a new concept since it was demonstrated by Tesla in 1899 [21][22] using radio waves.

The idea of exploiting the wave nature of light and converting its energy into usable DC form by using antennas was originated as a part of NASA summer project in 1960 by J.C. Fletcher and R.L Bailey [19]. The invention was similar to the rectenna proposed by Brown at microwave regime with a modification which allows both the antenna and rectifier to operate at much higher frequencies to harvest solar energy. The device invented by Bailey was called 'Electromagnetic Wave Energy Converter (EWEC)' which is presently entitled as 'Solar Rectenna' [10] [11].

Following the invention, the first official report was published by Bailey in 1972 as a proof of concept where he demonstrated the broadband characteristics of his antenna device. In 1975, Bailey et al. presented some theoretical works which equally emphasize on the potential research in the optimization of antenna design, fabrication, and rectification [19].

In 1988, Marks was first to patent antenna-like cylinders incorporated with asymmetrical Metal-Insulator-Metal (MIM) diodes for the purpose of rectification [16]. The first experimental work on a fabricated nanostructure that operates at visible regime was reported by Lin et al. in 1996 [23]. A brief historical timeline of the key events of the rectenna device is presented in Table 2.1.

Table 2.1: Key events of the rectenna device [16]

Year	Key Events
1899	Tesla demonstrated Wireless Power Transmission (WPT) using radio waves.
1960	The concept of rectenna was proposed by William C. Brown for WPT.
1963	The first rectenna device was built for Raytheon Company, by George, a professor at Purdue University.
1964	A Helicopter with an array of 28 rectennas was demonstrated to fly around 60 feet above a transmitting microwave beam.
1972	The concept of 'Electromagnetic Wave Energy Converter (EWEC)' was proposed by Bailey in an official report, which is regarded presently as 'Solar Rectenna'.
1988	Marks coupled cylindrical antennas to asymmetrical Metal-Insulator-Metal (MIM) diodes.
1996	Lin et al. demonstrated experimental evidence of a fabricated nanostructure that works at high frequency, i.e. visible regime.

2.2 Microwave Rectennas

According to the microwave antenna theory, the antenna operates as a transmitter or a receiver at resonance. Typically, for half wavelength antenna, the resonant wavelength is the wavelength of the incoming electromagnetic wave. Therefore, the dimension of the antenna is on the same scale as the wavelength of the incident wave. Generally, for low gigahertz frequencies, the dimension of the antenna can be from few millimeters to tens of centimeters. Since it is not difficult to fabricate devices of this size with the existing technologies, it results in high efficiencies.

In 1963, the first rectenna device was designed to work at 2.45 GHz, which was the most commonly used transmission-frequency for microwave power transmission (MPT) [11]. The device provided 7 W power output with an efficiency of 40% [22]. The rectenna consisted of half-wave dipole antennas to receive incident signal and point-contact diodes for rectification. In later designs, the same antennas were incorporated with Schottky barrier diodes (SBDs) which showed higher efficiency.

There was a steady increase in the efficiency of the rectennas operating at 2.45 GHz until the 1980s. The integration of Pt/GaAs Schottky diode with the antenna for rectification resulted in 92% efficiency [11], [24], the highest efficiency recorded for rectenna at 2.45 GHz till now. The higher efficiencies which have been reported so far, all rectennas used GaAs-based Schottky diodes instead of Si-based Schottky diodes. In 1975, Dickinson and Brown showed a successful demonstration of MPT by using an array of 5000 rectennas operating at 2.388 GHz with an efficiency of 82% [25]. The efficiency

values for rectennas operating at 5.8 GHz have been predicted in [26]–[28] and demonstrated in [26], [29], and [30] in the range of 60-85%. However, the theoretical approximation for rectennas operating at 35 GHz is higher than the corresponding experimental results [31], [32]. The experimental efficiency obtained for rectennas operating at 35 GHz has been reported around 70% [33], [34].

Rectennas operating at 5.8 GHz, 35 GHz, and 94 GHz were designed in the late 1990s. There were some rectennas even working in two frequency bands i.e. 2.45 GHz - 5.8 GHz [30] and 35GHz - 94 GHz [34], [35]. However, the efficiency for two frequency bands varies since the operation at higher frequency results in lower efficiency due to the transfer losses from the antenna to the rectifier circuit. The highest efficiency for dual frequency rectennas was reported around 82% [30] at both 2.45 GHz and 5.8 GHz where the rectenna consisted of a dipole antenna and GaAs-based Schottky barrier diode (SBD).

Unlike microwave rectennas, the efficiencies for optical rectennas are not much high. The size of the antenna scales linearly [12] with the incoming frequency in microwave regime. Therefore, the size of the antenna is supposed to reduce to the scale of optical wavelength, i.e. nanometer, for infrared or visible regime. However, this is not the case. The design of the antenna in microwave regime is not scalable to optical regime. This is due to the fact that the material properties inherently change in high-frequency regime. The metal antennas are considered to be good conductor at microwave regime, whereas at high frequencies the metals become lossy and the penetration depth [36] becomes significant.

Similar to microwave antennas, the optical nanoantennas convert the freely propagating electromagnetic radiation into localized electric field [14]. However, the electric field produced by the optical nanoantennas has a very high frequency. This high frequency electric field needs to be rectified before being delivered to the load. Therefore, it requires a fast switching diode that operates in femtoseconds and has the ability to perform rectification efficiently at high frequency. Thus, it is very difficult to replicate the high efficiencies of the microwave rectennas in the optical regime.

The incoming light from the sun is randomly polarized and distributed over a broad spectrum. This leads to some challenges in designing the nanoantennas. Moreover, a small variation in the incoming frequency increases the parasitic capacitance and inductance resulting in inefficient energy absorption [11]. Therefore, the design and fabrication of the optical antenna need to be precise to harvest solar energy in an efficient way.

2.3 Optical Nanoantenna

In analogy to radiowave and microwave counterparts, optical nanoantennas are transducers which convert the freely propagating electromagnetic radiation into localized energy and vice versa [14]. The RF antennas were developed for the purpose of communication, whereas the invention of optical nanoantennas was motivated by microscopy [37]. They enable the control and manipulation of the optical field at sub-wavelength scale. Traditionally, the fields of optics and photonics deal with the control

and manipulation of optical radiation by using mirror, lenses, and diffractive elements. Since the optical nanoantennas are able to manipulate and control optical radiation at nanoscale, they are effectively replacing the conventional focusing objects which concentrate external laser radiation to a dimension smaller than the diffraction limit [37].

Although many of the properties and parameters of the optical nanoantenna are similar to their radiowave and microwave counterparts; still, they have noticeable differences which result from their small dimensions and unique optical properties of the metal at nanoscale. Recent researches in nano-optics and plasmonics have produced a significant interest in optical nanoantennas which is looking for better ways to transform well-established radio and microwave theories into the optical regime.

The properties of the metal changes in optical frequency [11]. Metals are no longer considered as a good reflector since there is a significant amount of penetration of EM field into the metal. The penetration depth is wavelength dependent [36] and increases in metals with high frequency. The penetration of the EM field in the metal at high frequencies stems from the finite effective mass and considerable inertia of the conduction electrons [37]. This effective mass and significant inertia cause the electrons to react with phase lag with the driving field. The phase lag increases as the frequency of the field increases. Due to the phase lag between the oscillating field and electronic response, it causes skin depth [36] which becomes comparable to the spatial dimension of the optical nanoantenna. The penetration depth for metals at optical regime is typically around 20 nm. Since the incident radiation does not completely reflect from the metal's

surface, electrons in the metal do not respond to the external wavelength λ of the incident radiation but to the effective wavelength λ_{eff} which depends on the properties of the materials.

The effective wavelength λ_{eff} can be defined by [12] –

$$\lambda_{eff} = n_1 + n_2 \left(\frac{\lambda}{\lambda_p}\right), \qquad (2.1)$$

where, n_1 and n_2 are the geometric constants and λ_p is the plasma wavelength. According to the scaling rule, the spatial dimension for the optical nanoantenna is shorter than $\lambda_{eff}/2$. Here, λ_{eff} and λ differ only by the geometric constants [14].

When the dimension of the antenna elements is less than 5 nm then metals might not be the right choice of materials. Carbon nanotubes (CNTs) are better conductors than metals for dimension less than 5 nm [14]. Therefore, for small scale, Carbon-based materials such as Graphene or nanotubes might be a good selection for optical nanoantennas.

2.3.1 Drude Model

Metal nanostructure exhibits unique properties at optical regime compared to the microwave regime. At microwave regime, when the EM wave illuminates on a metallic surface, it is reflected back. However, the physics entirely changes once the frequency increases to THz, infrared, or visible regime. The metal becomes lossy and dispersive at

such high frequencies. The relative permittivity of the metal ε_r can be determined by using a classical conductivity model called Drude model [38]. In 1990, Paul Drude introduced a model to explain the transport properties of the electrons in materials [39].

There are some assumptions to be considered in Drude model:

- The electron is attached to a fixed core which is nucleus. The electric field causes a definite force which accelerates the electrons in the metal.
- Electron-electron interaction is ignored.
- The positively charged cores of the atoms cause damping force.

The electrons in the metal behave like quasi-free particles since they are loosely connected to the center of the atom. There are fixed positive ions and free electrons in the metal where the positive ions exert no restraining force on the electrons. Since the number of two oppositely charged particles in the metal is the same, the metals are considered to be plasma.

When EM wave strikes on the metallic surface, the electric field E causes an external force on the electron resulting in acceleration.

The electric field E can be defined by –

$$E = E_o e^{-i\omega t} . \tag{2.2}$$

The acceleration force experienced by the electron can be defined by –

$$F_{acc} = m\frac{d^2r}{dt^2} , \tag{2.3}$$

where, r is the displacement, m is the mass of the electron and t is the time.

According to the third assumption, there is a damping force since the electron is attracted to the center of the atom.

The damping force F_d caused by the atom can be defined by –

$$F_d = m\gamma \frac{dr}{dt}, \tag{2.4}$$

where, γ is the damping frequency.

The differential equation obtained for the displacement r is given by –

$$F_{acc} + F_d = qE, \tag{2.5}$$

where, q is the charge of the electron, i.e. $q = -e$. Thus, equation (2.5) can be simplified as follows:

$$F_{acc} + F_d = -eE_o e^{-i\omega t}\,. \tag{2.6}$$

The steady state solution for the displacement can be given by –

$$r = r_o e^{-i\omega t}\,. \tag{2.7}$$

Solving the differential equation in equation (2.6) gives as follows:

$$r_o = \frac{eE_o}{m\omega^2 + im\gamma\omega}. \tag{2.8}$$

The polarization P_o can be defined by –

$$P_o = -r_o eN, \tag{2.9}$$

where, N is the number per unit volume.

Substituting the values of r_o in equation (2.9) results as follows:

$$P_o = \frac{-\frac{e^2}{m} N E_o}{\omega^2 + i\gamma\omega}. \tag{2.10}$$

The electrical displacement D can be defined by E through polarization as follows:

$$D = \varepsilon_o E + P, \tag{2.11}$$

$$D = \varepsilon_o E + \varepsilon_o \chi E, \tag{2.12}$$

where, χ is the susceptibility of the material.

Equation (2.12) can be simplified as follows:

$$D = \varepsilon_o E(1 + \chi), \tag{2.13}$$

$$D = \varepsilon_o \varepsilon_r E\ , \tag{2.14}$$

where, ε_r is the relative permittivity of the metal and is given by –

$$\varepsilon_r = 1 + \chi, \tag{2.15}$$

$$\varepsilon_r\ = 1 - \frac{P}{\varepsilon_o E}\ , \tag{2.16}$$

$$\varepsilon_r = 1 - \frac{\frac{e^2 N}{m\varepsilon_o}}{\omega^2 + i\gamma\omega}. \tag{2.17}$$

By assuming,

$$\frac{e^2 N}{m\varepsilon_o} = \omega_p^2\ , \tag{2.18}$$

We can rewrite (2.17) as follows:

$$\varepsilon_r = 1 - \frac{\omega_p^2}{\omega^2 + i\gamma\omega}. \tag{2.19}$$

Therefore, the relative permittivity ε_r of the metal can be defined by Drude model as follows:

$$\varepsilon_r = 1 - \frac{\omega_p^2}{\omega^2 + i\gamma\omega}\,. \qquad (2.20)$$

In some other literature, the relative permittivity ε_r of the metal has been defined by Drude model as follows:

$$\varepsilon_r = \varepsilon_\infty - \frac{\omega_p^2}{\omega^2 + i\gamma\omega}\,, \qquad (2.21)$$

where, ε_∞ in most cases, equals to 1. The positive (+) sign in front of the term $i\gamma\omega$ results due to $e^{-i\omega t}$. The change in the sign of the exponent term will result in a change of the expression for Drude model. The parameters ε_∞, ω_p, and γ can be obtained by fitting measured values. The Drude model for metal is illustrated in Fig.2.1.

Since ω is directly related to the wavelength of the incident wave, the relative permittivity ε_r of the metal can be expressed as a function of wavelength λ.

Fig.2.2 shows that the relative permittivity ε_r of the metal can be written in the following form:

$$\varepsilon_r = -\varepsilon_1 + i\varepsilon_2\,, \qquad (2.22)$$

where, ε_1 is the real part ($\varepsilon_1 > 0$) and ε_2 is the imaginary part ($\varepsilon_2 > 0$). The real part of the relative permittivity is negative for silver from 400 nm to 1600 nm, as shown in Fig. 2.2. This characteristic is important since it leads to a phenomenon called Surface

Plasmon Polariton (SPP) which is discussed in later section. On the other hand, the imaginary part of the relative permittivity means losses.

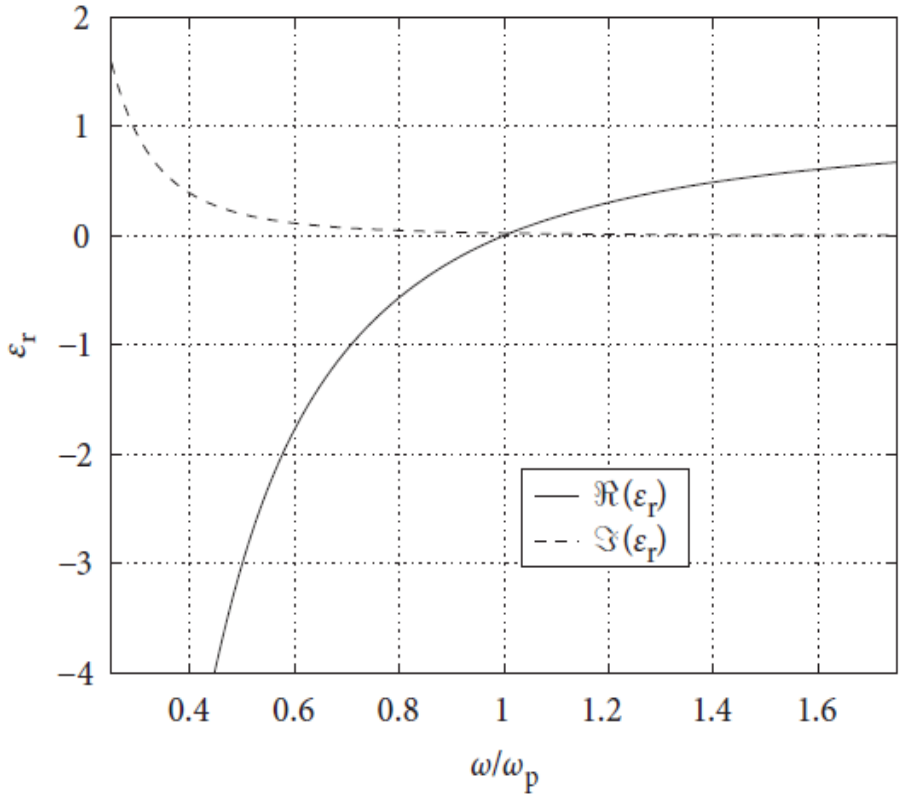

Figure 2.1: The real and imaginary part of the relative permittivity of the metal for $\gamma = \frac{\omega_p}{4}$ [40].

Typically high values of ε_2 indicate strong losses. Therefore, metals in the optical regime are considered to be lossy. Moreover, the relative permittivity ε_r of the metal is wavelength-dependent in the optical regime and dispersive in nature [40].

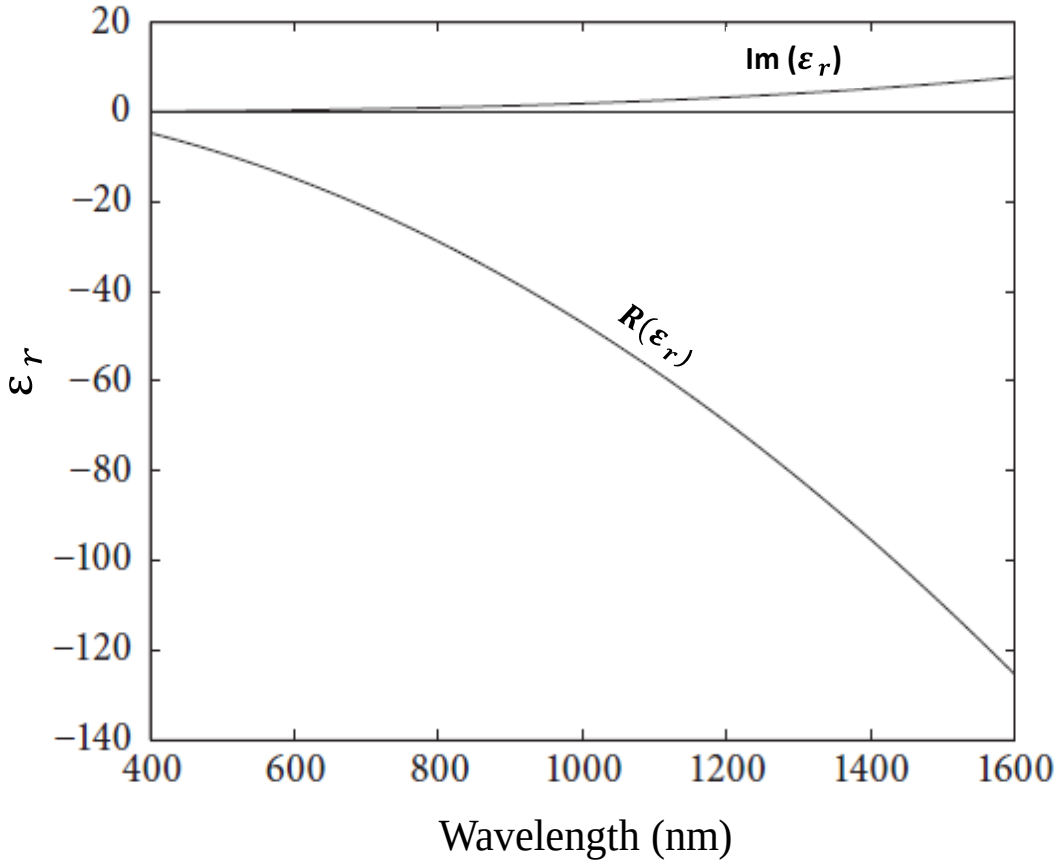

Figure 2.2: Relative permittivity ε_r of Silver using Drude model at the optical regime. For Silver, ε_∞= 3.36, ω_p= 1.33 $\times 10^{16} s^{-1}$ and γ =7.075 $\times 10^{13} s^{-1}$[40].

2.3.2 Limitation of Drude Model

All the interactions that occur between electrons and atoms are not considered in Drude model. Moreover, the quantum mechanical effects were not taken into account for Drude approximation. Therefore, some deviations are observed in the experimental data

from the theoretical estimation of Drude model. Fig. 2.3 shows the reflectivity of Aluminum (Al) and compares the theoretical data to the experimental one [39].

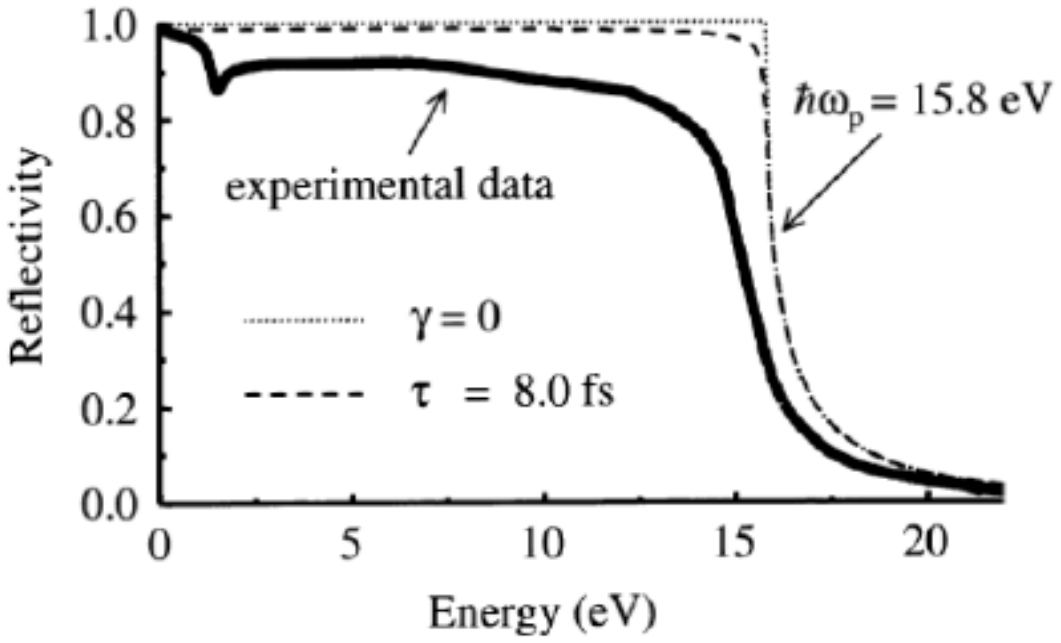

Figure 2.3: Experimental reflectivity of Aluminum (Al) as a function of photon energy, copyright@ American Physical Society [39].

The experimental reflectivity of Al is compared to the expected free electron model with $\hbar\omega_p = 15.8$ eV. One of the curves i.e. dotted is calculated with no damping and the other one i.e. dashed is estimated with a damping of 8.0 femtosecond. The experimental curve shows that there is a significant dip in the reflectivity of Al which did not appear in the theoretical curve obtained by Drude model. The reason behind that is the 'interband transition' that is shown in Fig. 2.4. When the energy of a photon is comparable to the

energy gap, it excites an electron from an occupied state in the valence band to an unoccupied state in the conduction band. This is called interband transition.

This transition can occur in two different ways:

- Direct (Momentum of the electron is conserved)
- Indirect (Momentum of the electron changes)

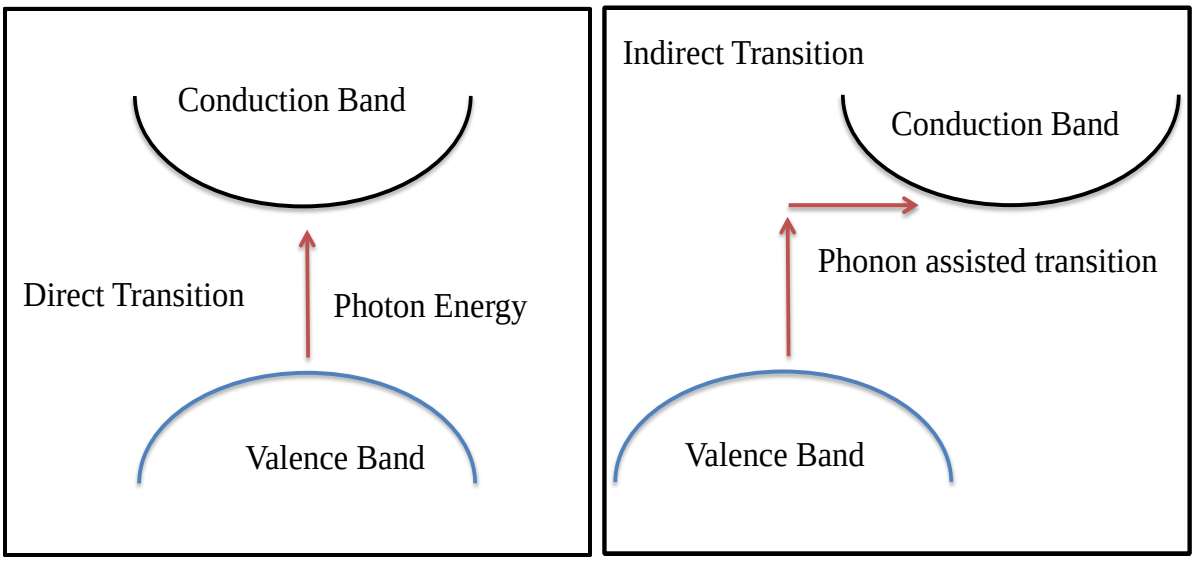

Figure 2.4: (a) Direct transition (b) Indirect transition between the valence band and the conduction band.

The direct transition occurs when the energy of the photon is absorbed by the electron with no change of momentum. On the other hand, for indirect transition, the energy of the phonon is absorbed when there is a change in the momentum required by the electron.

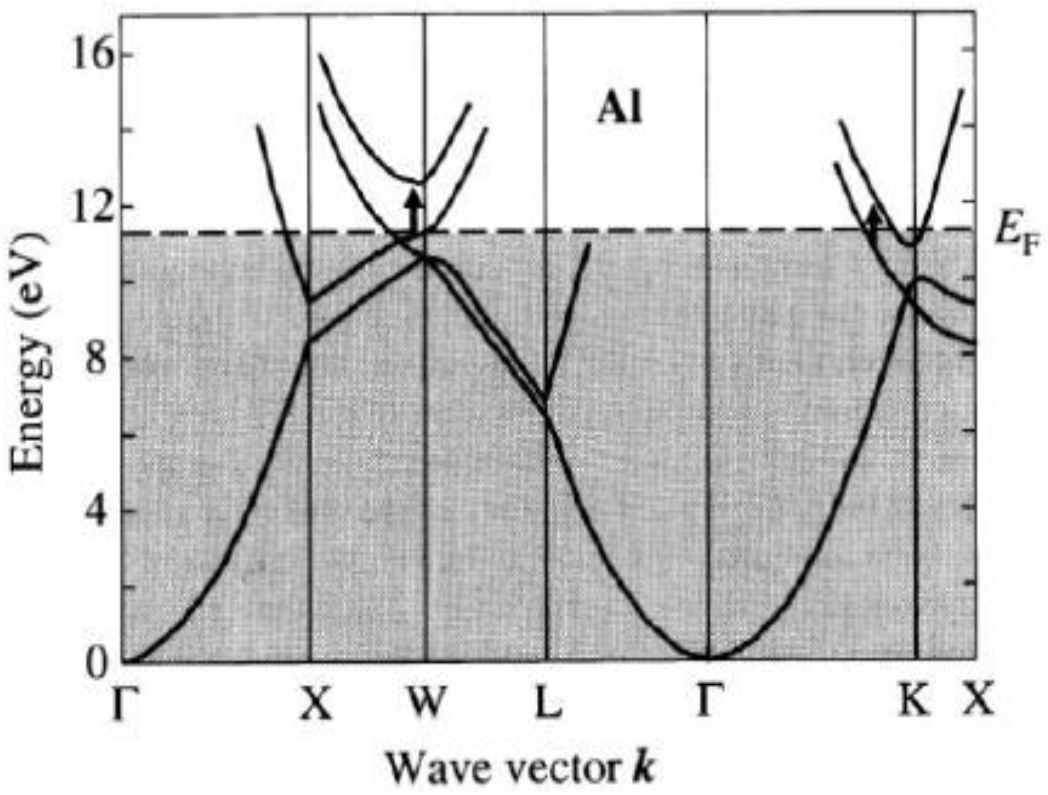

Figure 2.5: Energy band diagram of Aluminum (Al), copyright@ American Physical Society [39].

It can be observed in Fig. 2.5 that there are bands at W and K points, which are direct in nature. Thus, there is no need for phonon assisted transition of electrons from valence to conduction band which means there is no change in the value of the wave vector. The direct transition requires almost 1.5 eV energy of the photon resulting in a significant dip in the reflectivity of the Al in the experimental data.

2.3.3 Reflectivity & Conductivity in Metal

The simple model of metal involves a rigid arrangement of positively charged ions and negatively charged free electrons. Since the electrons are free particles and move randomly on the metal surface, they arrange themselves on the surface of the metal in such a way that the internal electric field vanishes. The free electrons respond to the external applied electric field. The electric field usually does not penetrate into the metal. Therefore, metals are usually good reflectors.

Ionized gases have also the charge arrangement similar to the metals. There are fixed positive ions and movable free electrons which exhibit ‘metal-like' behavior and tend to be good reflectors. Atoms in the upper atmosphere are mostly ionized and hence act as a good reflector for radio and microwaves [41].

When a high-frequency electric field is applied on the metal surface instead of static or low-frequency electric field, the characteristic of the metal changes and it becomes an absorber. The free electrons on the surface of the metal fail to respond to the rapid changes in the electric field as the frequency increases. Therefore, the electric field penetrates the surface of the metal at high frequency regime and gets absorbed.

Similarly, for high frequencies such as THz, infrared, and visible regime, ionized gas behaves as an absorber. If the gas is not dense enough, it becomes transparent to the high frequency radiation. Therefore, it reflects radiowaves but transmits waves which lie in the high frequency regime. It becomes very strong absorber at UV frequencies [41].

The reflectivity of the metal depends on the complex refractive index n_c and extinction coefficient k which is given by [39]–

$$R = \left|\frac{n_c - 1}{n_c + 1}\right|^2, \tag{2.23}$$

where, n_c is the complex refractive index of the material and is defined as follows:

$$n_c(\omega) = n(\omega) + ik(\omega). \tag{2.24}$$

Therefore, equation (2.23) can be written as follows:

$$R = \frac{(n-1)^2 + k^2}{(n+1)^2 + k^2}\,. \tag{2.25}$$

The relative permittivity ε_r of the material is related to the reflective index n_c in the following way –

$$n_c = \sqrt{\varepsilon_r}\,. \tag{2.26}$$

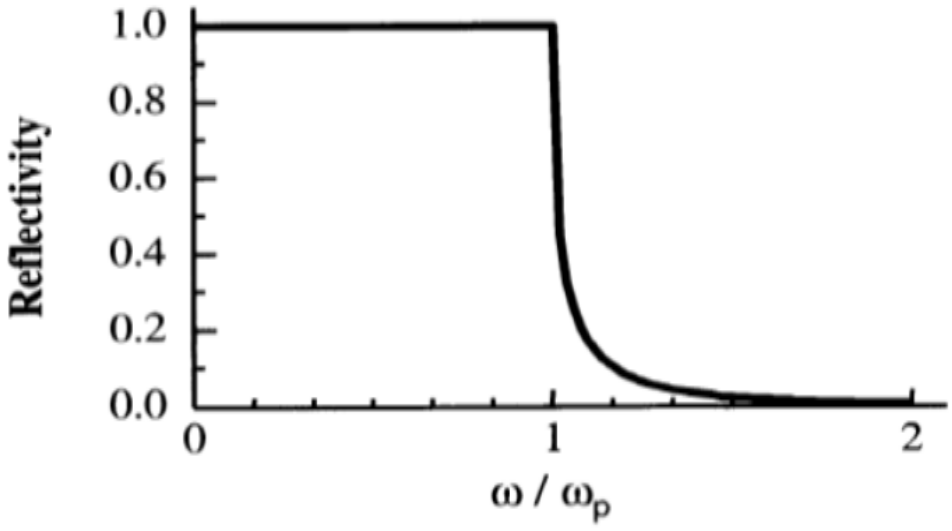

Figure 2.6: Reflectivity of metal as a function of frequency [39].

Fig 2.1 shows that for ω less than ω_p, ε_r is negative. This implies that n_c is purely imaginary. Therefore, in equation (2.25), the value reflectivity, R, becomes 1, i.e. 100% reflectivity. This indicates that the metal surface acts as a good reflector for the incident electromagnetic wave which has a frequency less than plasma frequency. Once the incident frequency is equal or above the plasma frequency, the reflectivity is not 100% anymore rather it drops off and acts as an absorber, as shown in Fig. 2.6.

From equation(2.4), we write as follows:

$$m\frac{dv}{dt} + m\gamma v = -eE, \tag{2.27}$$

where, v is the velocity of the free electrons and can be defined as,

$$v(t) = v_o e^{-i\omega t}. \tag{2.28}$$

Substituting the value of (2.28) in equation (2.27), we can obtain,

$$v(t) = \frac{-eE}{m(\gamma - i\omega)}\,. \tag{2.29}$$

The expression of the current density of a material can be defined in terms of electrical conductivity and velocity of electron as follows:

$$J = \sigma E, \tag{2.30}$$

$$J = -Nev\,. \tag{2.31}$$

By solving, equation (2.29), (2.30) and (2.31), we obtain the following expression for $\sigma(\omega)$,

$$\sigma(\omega) = -\frac{Ne^2}{m(\gamma - i\omega)}\,, \tag{2.32}$$

where, $\sigma(\omega)$ is the electrical conductivity of the metal at any frequency range. However, at very low frequency i.e. $\gamma \gg \omega$, the electrical conductivity, σ, of the metal becomes frequency-independent and equation (2.32) can be given as follows:

$$\sigma_o = -\frac{Ne^2}{m\gamma}, \qquad (2.33)$$

where, σ_o is the dc conductivity of the metal and usually used in low-frequency regime i.e. microwave regime. However, for high frequencies such as infrared and visible regime, the electrical conductivity of the metal is frequency-dependent.

In retrospect, low frequency i.e. less than plasma frequency (ω_p), metals act as good reflectors. Moreover, the electrical conductivity of the metals is almost constant and frequency-independent at low frequencies. On the other hand, at high frequency i.e. above plasma frequency (ω_p), metal becomes lossy due to the high penetration of EM waves and electrical conductivity becomes frequency-dependent.

2.3.4 Surface Plasmon (SP)

Surface Plasmon (SP) is widely recognized among the scientists ranging from physicists and chemists to biologist. Surface Plasmon became of great interest in research field due to its potential in optics, magneto-optic data storage, sensors, solar cells, and nanoantennas.

Surface Plasmons are electromagnetic waves that propagate along the surface of the conductor. In essence, when the light wave interacts with the surface of the metal, the free

electrons respond collectively by oscillating in resonance with the light wave. The resonant interaction between the collective oscillation of the surface charges and the electromagnetic field of the light wave propagating along the metal-dielectric interface is called Surface Plasmon. It was first reported by Ritchie in 1957 [42].

There are two types [43] of Surface Plasmons:

- Propagating Surface Plasmon Polaritons (SPP)
- Localized Surface Plasmons (LSP)

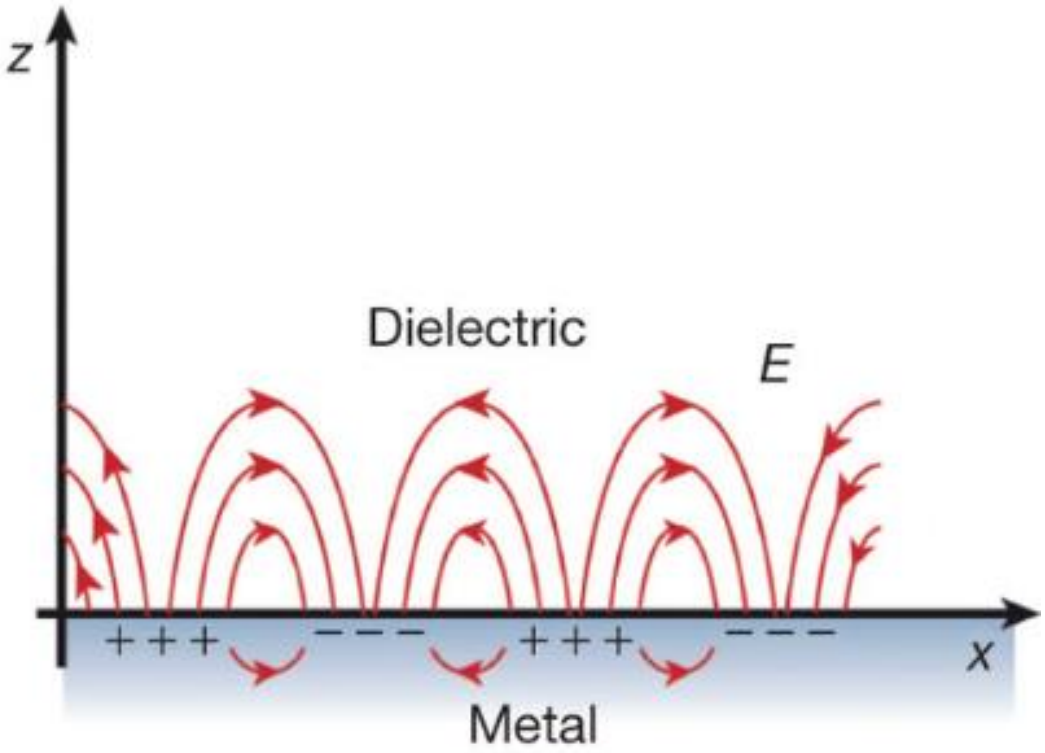

Figure 2.7: Surface Plasmons at the interface between metal and dielectric material [44].

- **Surface Plasmon Polariton (SPP)**

The Surface Plasmon Polariton (SPP) usually takes place when it satisfies the following conditions:

- The interface is between metal and dielectric media, as shown in Fig. 2.7.
- The frequency-dependent permittivity ε_r of the metal is negative ($\varepsilon_r < 0$) and the absolute value is larger than the permittivity of the dielectric ε_d . The permittivity of the metal and dielectric has to be opposite in signs i.e. $\varepsilon_r < 0$ and $\varepsilon_d > 0$. Surface Plasmon (SP) cannot occur at the interfaces between two dielectric media since the permittivity is positive.

The propagation nature of SP is along the interface of the metal-dielectric. The field perpendicular to the surface, called evanescent or near field, decays exponentially with the distance from the surface. Fig. 2.8 shows that in metals the field decays faster than in dielectric due to smaller skin depth value [45]. Since the wavelength of SPP is much smaller than the wavelength of incident light, it leads to strong confinement of electromagnetic field. The propagation of SPP continues along the interface until all the energy is lost.

SPP gives rise to unique properties. It helps to concentrate and channel the light through the sub-wavelength structures. The concentration of light results in high electric field enhancement that can be employed to manipulate light-matter interaction and increase nonlinear properties.

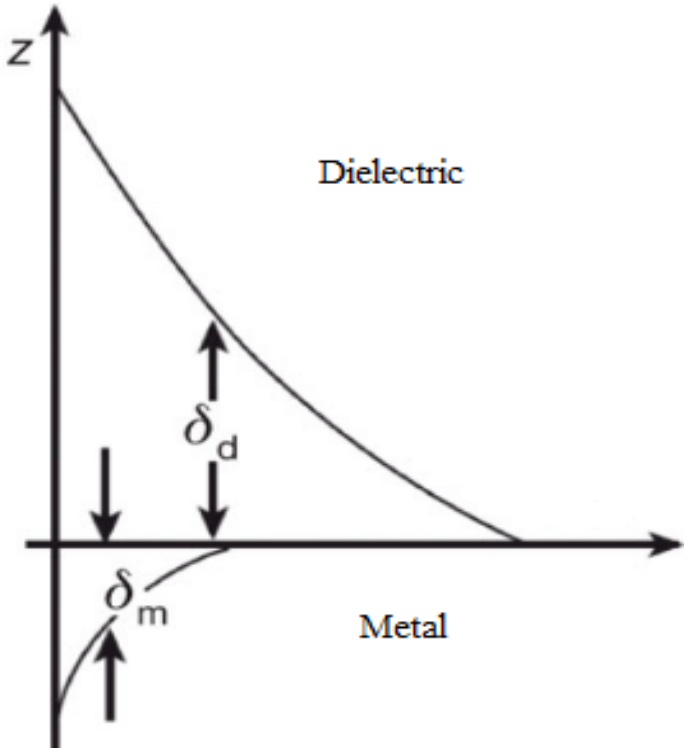

Figure 2.8: Field penetration decays exponentially in both metal and dielectric medium [44].

- **Localized Surface Plasmon (LSP)**

When a particle, has a dimension comparable to the wavelength of light, gets excited by a light wave, it results in strong confinement of Surface Plasmon which causes enhancement in the near field [46]. The strong confinement of the electric field leads to collective oscillation of free charge carriers on the surface called Surface Plasmon Resonance (SPR). When this resonance occurs in the sub-wavelength device, it is called Localized Surface Plasmon Resonance (LSPR) [43], [47].

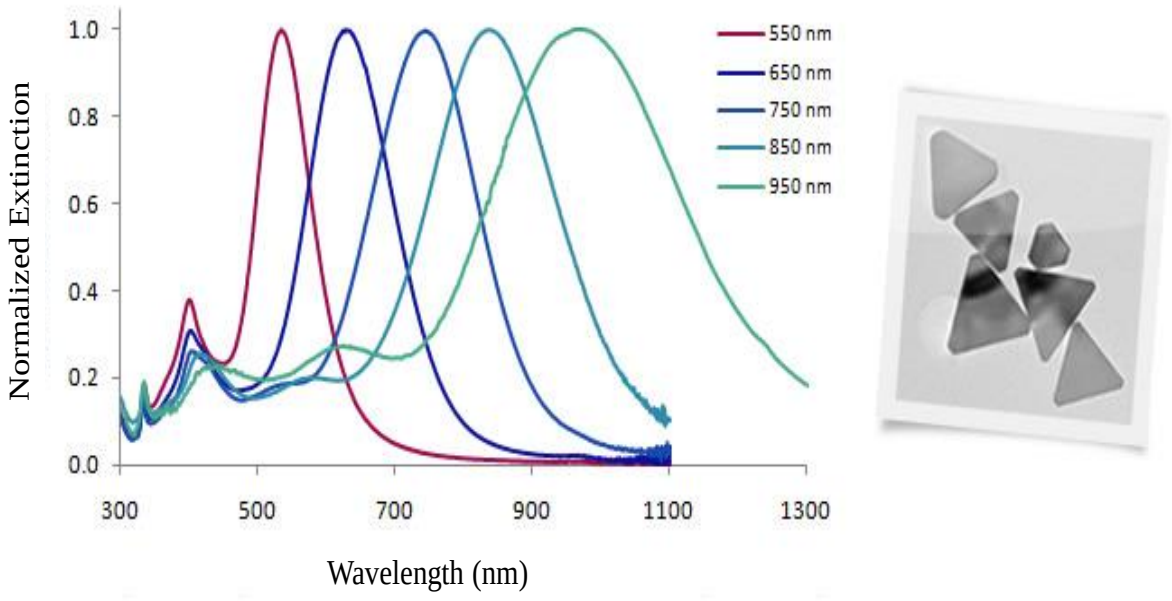

Figure 2.9: Excitation spectra changes with the size of the nanoparticles. The increase in the size of the nanoparticles leads to broader spectrum and redshift in the resonance (left). SEM images of the Silver nanoparticles (right) [43].

LSPR is mostly used for sensing applications due to their high sensitivity to the changes in the refractive index of the surrounding mediums. Fig. 2.9 shows the LPSR of Silver (Ag) nanoparticles which change due to the change in the particle's shape and size. It is observed that the resonance shifts at a longer wavelength with a broader spectrum, as the size of the particle increases. Due to LPSR, sub-wavelength devices such as optical nanoantennas allow strong confinement of the electric field. The electrons on the surface of the nanoantenna collectively oscillate as the same frequency of the incident light wave, producing a highly concentrated electric field called the feed point of the antenna [48].

The local field is confined in the feed gap, tips and around the structure, as shown in Fig. 2.10. The field decays significantly as the distance increases from the structure.

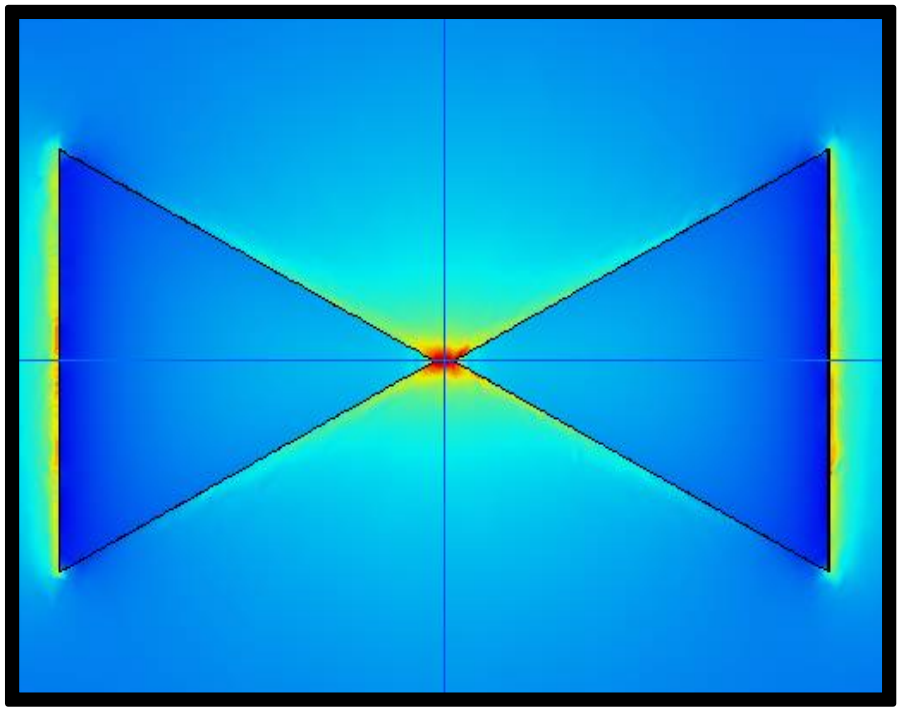

Figure 2.10: Local field enhancement at the gap, tips, and around edges of the bowtie nanoantenna.

2.3.5. Applications of Optical Nanoantenna

Optical nanoantenna has many applications in various spheres of human activity such as medicine, photovoltaics, spectroscopy, near-field microscopy, and photonics. Nanoantenna has already been employed in some operating devices i.e. spectroscopy and also expected to be employed in some others, i.e. medicine, very soon in near future. The

recent and potential applications of the optical nanoantenna have been discussed briefly in this section.

- **Photovoltaics**

One of the recent developments of solar power engineering is the employment of thin film solar cells to harvest energy from solar radiation. The employment of thin photosensitive films in solar cell may decrease the cost of electric power [49].

However, the huge amount of toxic waste which is formed in high-purity semiconductor manufacturing process is a major obstacle for further progress in solar power generation. Moreover, absorption of incident light by thin photosensitive layers is not effective enough. The use of an antireflection coating to obtain high-efficiency absorption in solar cells is not feasible since it is also necessary to prevent its passage through the optically thin photo absorbing layer [49]. Considering all these factors, the industrial production of the ultra-thin film based solar cells is slowed down.

These challenges can be addressed using optical nanoantenna. Since optical nanoantenna can strongly confine solar radiation in sub-wavelength devices, a successful confinement will prevent the reflection of the incident wave from the surface and its passage through the photosensitive layer.

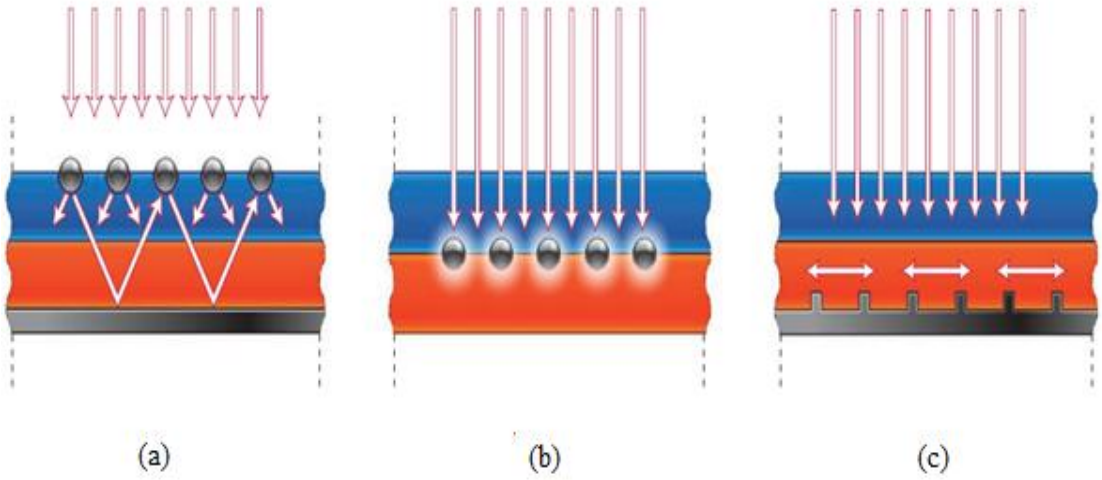

Figure 2.11: (a) Light trapping by using metallic nanoparticle in the solar cell. (b) Light trapping by embedding metallic nanoparticles as nanoantennas in the solar cell. (c) Light trapping by embedding metal film on the back surface of the photovoltaic absorber layer [50].

Recently, researchers are focusing their attention to improve the absorption of the photovoltaic devices by a plasmonic design based approach which can be called the plasmonic solar cell. This plasmonic design allows a considerable reduction in the physical thickness of the absorber layer while keeping their optical thickness constant by light-trapping nanostructure. This plasmonic nanostructure allows the shrinkage of the physical thickness of the absorber in three different ways [50]:

- An array of metallic nanoparticles can be employed as sub-wavelength scattering elements on the surface of the solar cell. It allows to couple and traps freely

propagating electromagnetic radiation in the semiconductor thin film. Therefore, it results in an increase in effective optical wavelength, as shown in Fig. 2.11(a).

- Metallic nanoparticles can be employed as sub-wavelength nanoantennas in the solar cell. It couples the plasmonic near-field and traps the propagating light into the semiconductor, as shown in Fig. 2.11(b).
- Metallic film can be employed on the back surface of the thin photovoltaic layer. It couples sunlight into surface plasmon polariton (SPP) modes at the metal-semiconductor interface and guided modes in semiconductor slab, as shown in Fig. 2.11(c).

- **Near-Field Microscopy**

Optical nanoantenna has potential application as specialized probe in near-field microscopy [49]. Conventional near-field probes work based on the electromagnetic field enhancement near the tip of the metal. Though the design of the near-field probes based on optical nanoantennas is sophisticated, the efficiency increases dramatically. Bowtie based probes [51] show an increase in the signal to noise ratio by almost two orders of magnitude with better images resolution compared to the other classical rounded aperture probes, as shown in Fig. 2.12.

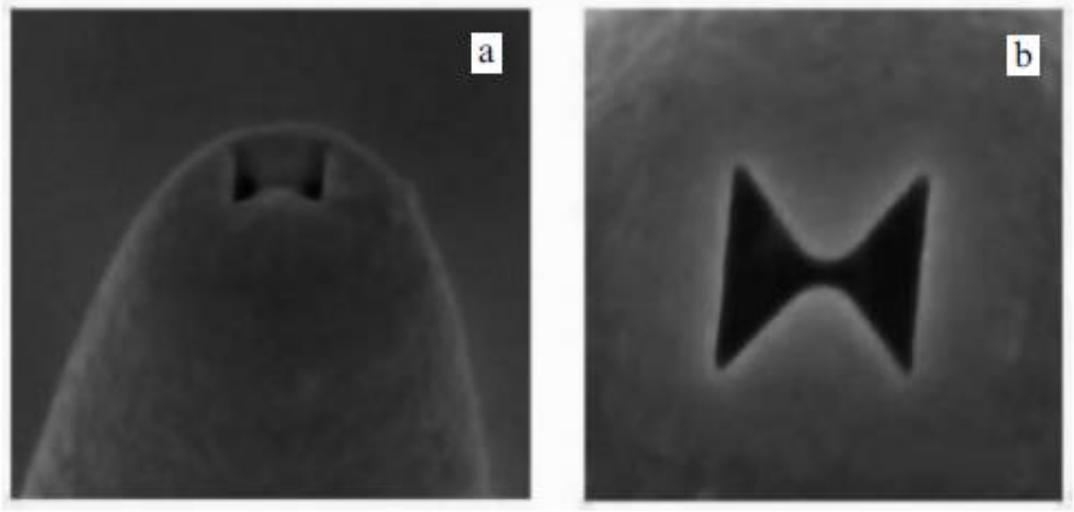

Figure 2.12: A near field probe based on bowtie (right) has a better signal to noise ratio than classical rounded aperture (left) [50].

- **Medicine**

Optical nanoantenna has potential applications in imaging and detection of different diseases which require biomarkers. Metal nanoshells were the first nanoparticles which have been used to demonstrate photo-thermal cancer therapy [52]. Metal nanoshell is introduced at the affected place of the body which gets irradiated by infrared light. The radiation gets absorbed by the nanoshells and causes thermal heat in nanoparticles. The heat is later transferred to the malignant tissue and kills the cancer cell [49], [52].

2.4. Rectifiers for Nanoantennas

When the antenna receives high-frequency EM waves, it creates a local electric field of high intensity. Consequently, high-frequency electrical current flows on the surface of the nanoantenna and gets rectified by a diode before being delivered the load, as shown Fig. 1.5. The rectification of the high-frequency current becomes very challenging with classical diodes. Most of the semiconductor diodes are RC time limited and cannot be employed to perform rectification at high frequency. Schottky diode is a fast switching diode; nevertheless, it becomes impractical when the frequency goes up to few THz or infrared range [53], [54]. The Tunnel diode which works based on quantum tunneling principle is a suitable candidate for rectification at high frequency. Tunnel diodes such as Metal-Insulator-Metal (MIM) diode [55], [56] is the most mature contemporary technologies to perform rectification at the high-frequency regime.

In this section, the operation mechanism of Tunnel diode and MIM diode operating at high frequency regime is discussed. In addition, the overall efficiency of the rectenna is discussed. Lastly, the fundamental limitations of the THz or infrared rectifiers are discussed.

2.4.1. Physical Interpretation of Quantum Tunneling

Quantum Tunneling refers to a quantum mechanical phenomenon where a particle tunnels through a barrier. In classical physics, a particle with low energy does not have

the ability to go through or over the higher potential energy barrier, whereas in quantum mechanics a particle with low energy has a possibility to go through the higher potential barrier. The thickness of the potential barrier plays an important role while tunneling.

For example, if the energy of the particle is E and the potential of the barrier is $V(x)$, where the potential varies with space. In classical physics, there is simply no way for the particle to travel across the other side of the barrier, if the energy of the particle $E < V(x)$. However, in quantum mechanics, there is a certain probability for the particle with energy E to penetrate through the potential barrier $V(x)$ even though $E < V(x)$, as shown in Fig. 2.13. This quantum mechanical phenomenon is called Tunneling [57].

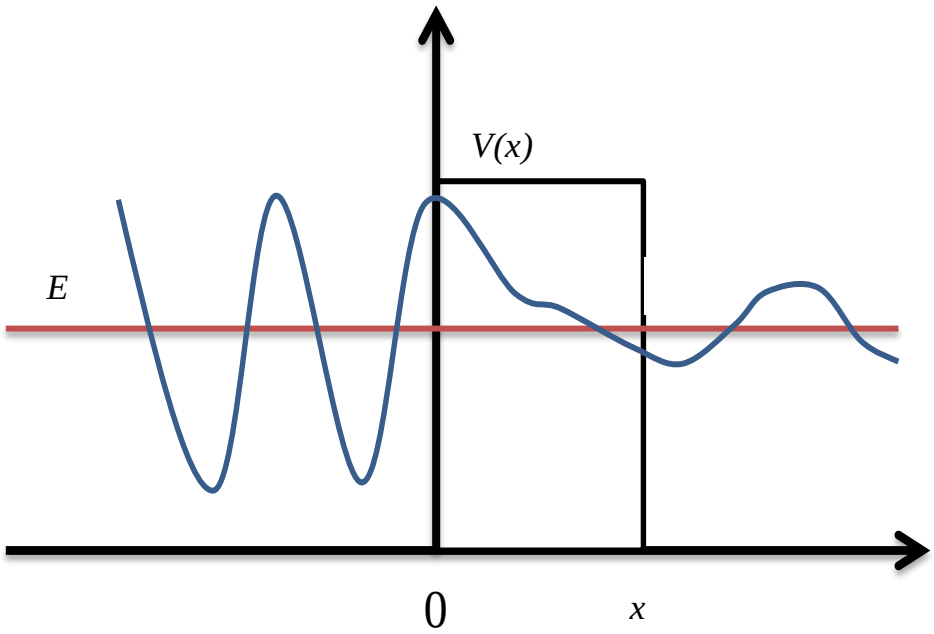

Figure 2.13: Quantum mechanical tunneling a particle through the potential barrier.

The thickness of the potential barrier is an important issue. Usually, the tunneling takes place for very thin barrier i.e. 1~3 nm. If the thickness increases, the probability of an electron to tunnel through the barrier decreases exponentially [17].

2.4.2. Tunnel Diodes

The tunnel diode, also named as Esaki diode, has a PN junction where both p and n type semiconductors are degenerately doped. Therefore, the Fermi level for n-type semiconductor is inside the conduction band and the Fermi level for p-type semiconductor is inside the valence band. That means electrons will exist in the conduction band and holes will exist in valence band even at equilibrium. The energy band diagram of a PN junction in the thermal equilibrium for degenerately doped semiconductor is shown in Fig. 2.14. The depletion width decreases as the doping increases. The probability of tunneling through the barrier gets higher as the potential barrier gets thinner [57].

If a positive bias is applied to the PN junction, there will be tunneling current flowing through the junction. The current-voltage characteristic curve due to the tunneling effect is shown in Fig. 2.18, which is divided into several regions. The tunneling mechanism in the diode can be explained in a simple way. The tunneling current in forward bias of the diode is divided mainly into three different regions:

- Region I: Tunneling Current Region.
- Region II: Differential Negative Current Resistance.
- Region III: Diffusion Current Region.

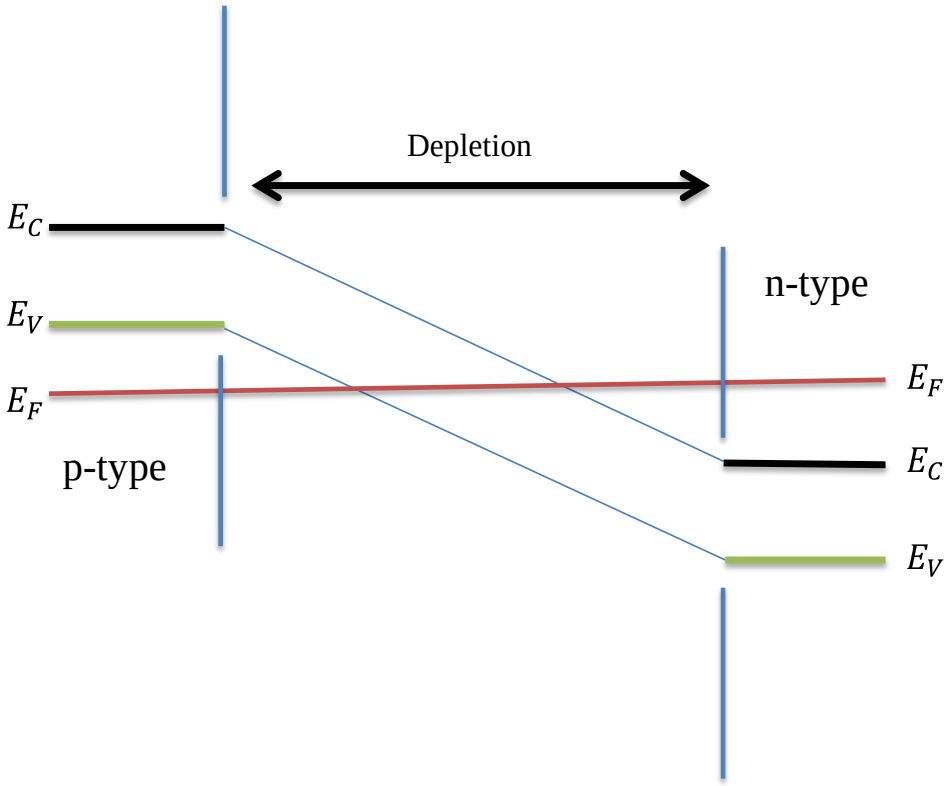

Figure 2.14: Degenerately doped semiconductor at thermal equilibrium.

- **Region I: Tunneling Current Region**

The electrons in the conduction band of the n-type semiconductor are directly opposite to the empty states of the valence band of p-type. Therefore, when a small forward bias voltage is applied to the junction, there is a finite probability for the

electrons to tunnel directly into the empty states, as shown in Fig. 2.15 (a). If the forward bias voltage is increased then the depletion region decreases and there will be a maximum amount of electrons tunneling through the junction resulting in maximum tunneling current as shown in Fig. 2.15 (b).

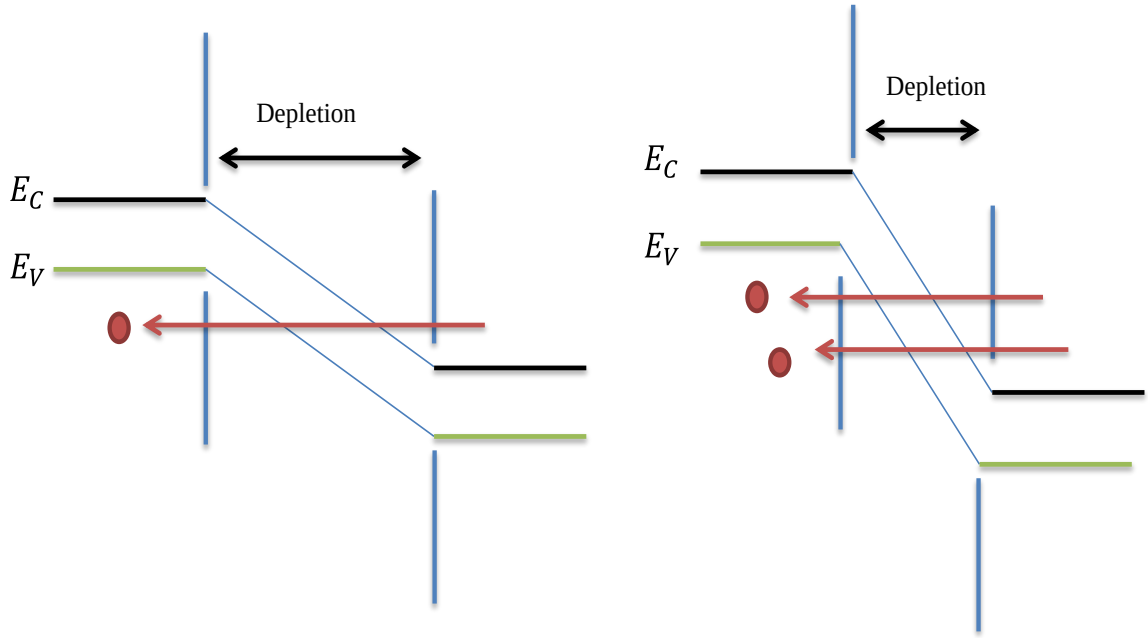

(a) (b)

Figure 2.15: (a) Tunneling current due to forward bias. (b) Tunneling current increases with the increase in the forward bias (since depletion region decreases).

- **Region II: Differential Negative Resistance Current Region**

When the forward bias voltage is increased, the number of electrons on the n-type directly opposite to the p-type decreases because there was a large flow of electrons

previously. Therefore, over time, the tunneling current decreases with an increase in the voltage in the forward bias, as shown in Fig.2.16. The region where the current decreases with an increase in the voltage is called differential negative resistance. Tunnel diode exhibits negative resistance which can be used for other applications as well.

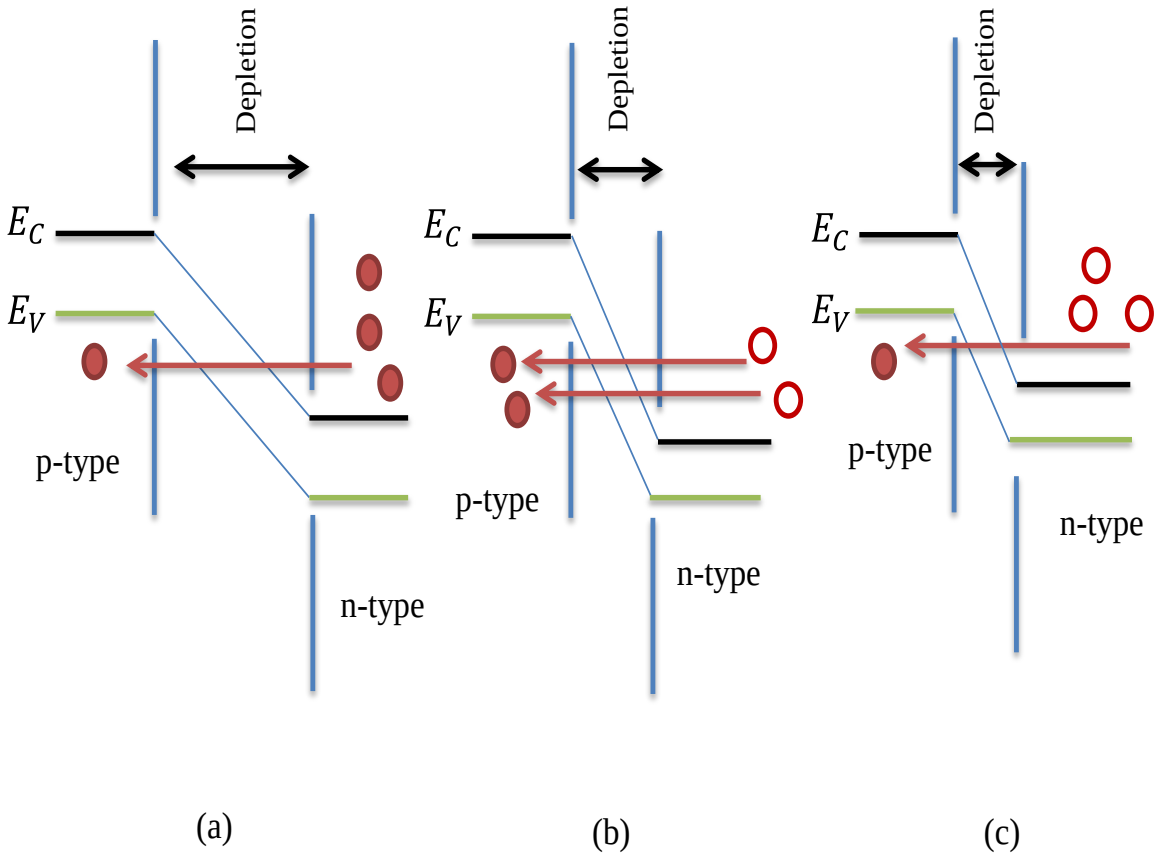

Figure 2.16: (a) Tunneling current due applied forward bias. (b) Tunneling current increases due to increase in the forward bias and creating holes in n-type. (c) Tunneling current decreases since a number of electrons in n-type decrease (differential negative resistance).

- **Region III: Diffusion Current Region**

Once the tunneling current decreases the normal diffusion current begins to rise with the increase of the forward voltage due to the low barrier potential, as shown in Fig. 2.17.

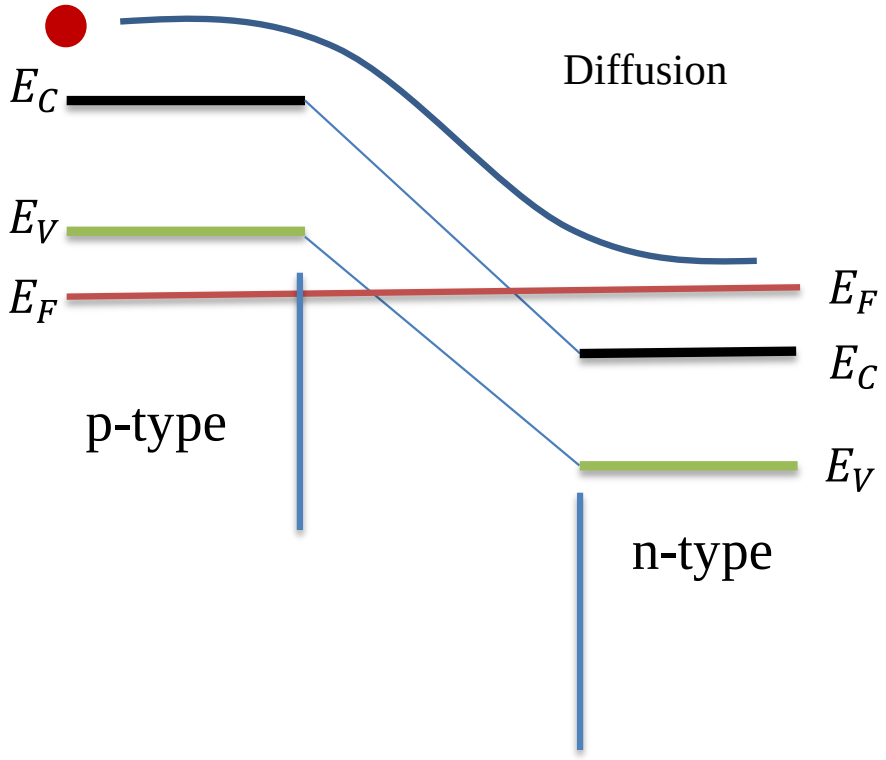

Figure 2.17: Diffusion Current flows through the potential barrier.

In the reverse bias voltage, electrons in the valence band on the p-type are directly opposite to the empty states in the conduction band on the n-type. Therefore, electrons can tunnel directly from p-type to n-type resulting in a large reverse bias tunneling current, as shown in Fig.2.19.

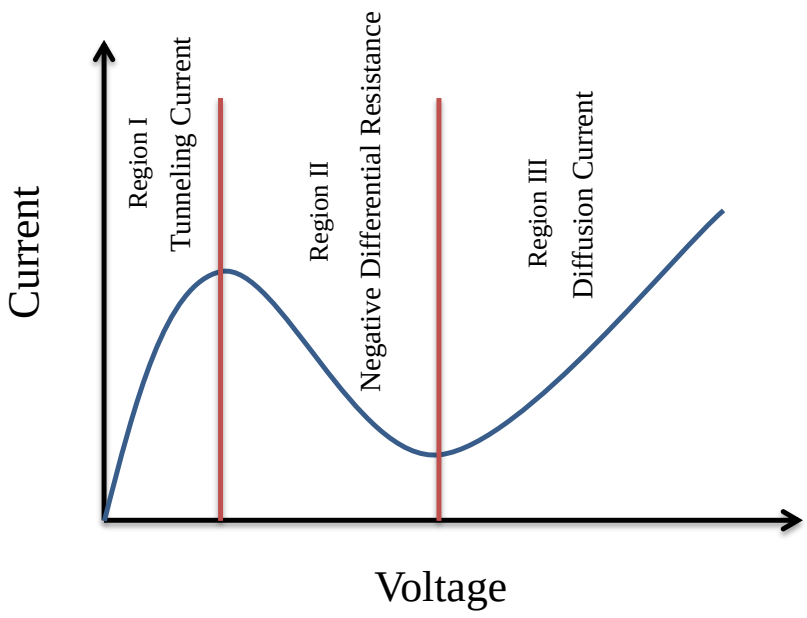

Figure 2.18: Tunneling current in forward bias direction subdivided into three regions.

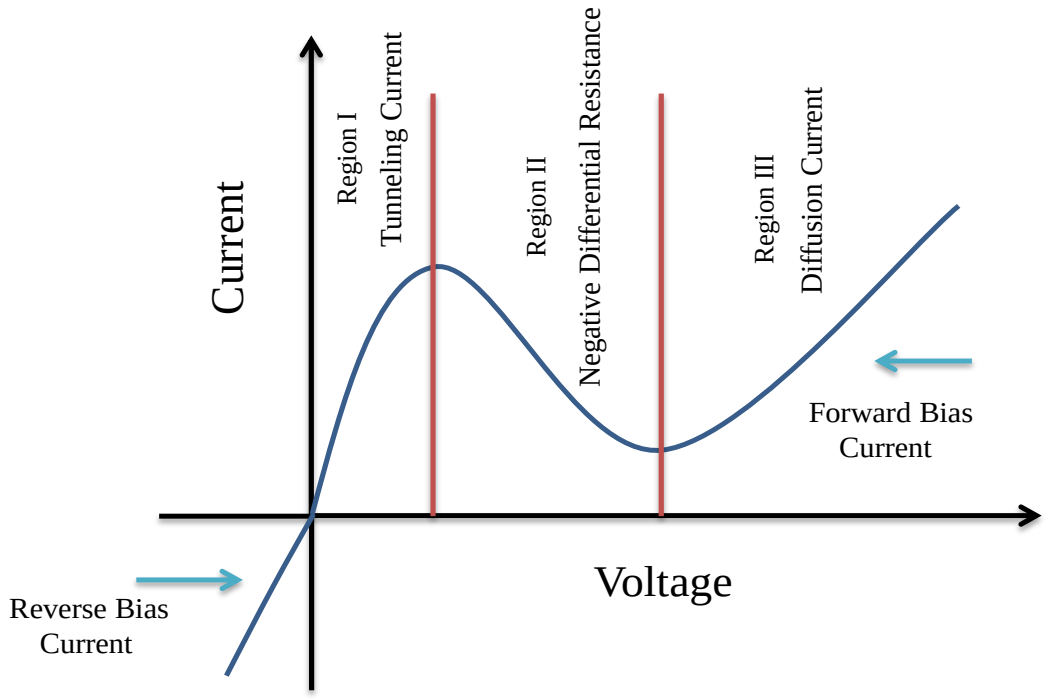

Figure 2.19: Tunneling current for reverse bias voltage.

2.4.3. Metal-Insulator-Metal (MIM) Diode

Metal-Insulator-Metal (MIM) diodes have shown promising characteristics in the high-frequency application such as frequency measurement in infrared [58] and infrared detectors [13]. Quantum tunneling is the predominant carrier transport mechanism in MIM diodes.

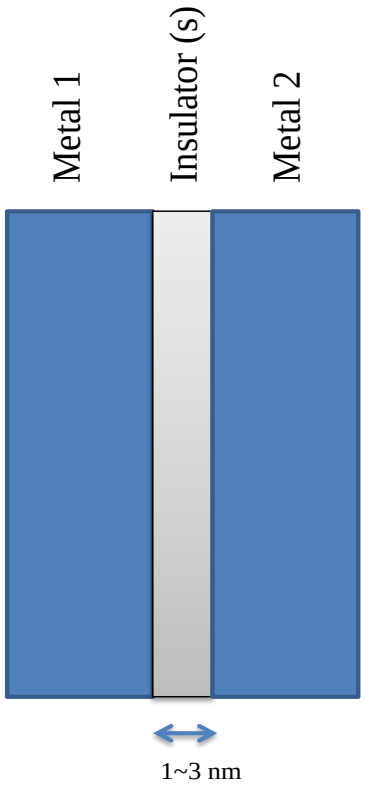

Figure 2.20: Physical structure of Metal-Insulator-Metal (MIM) diode.

The tunneling of the charges takes place between two metals which are spatially displaced from each other by nanometers of insulator or stack of insulators, as shown in Fig. 2.20. The work function of the two metals can be different from each other. The

insulator can be the native oxide of one of the metals employed in the diode. The properties of the insulator and shape of the potential barrier work as a function of the tunneling current [59].

To understand the tunneling mechanism in MIM diode, it is necessary to observe the energy band diagram of the MIM diode. The shape of the energy band diagram of an ideal MIM diode, as shown in Fig. 2.21, is determined by four different quantities [55] :

- Work function of Metal 1, Φ_1
- Work function of Metal 2, Φ_2
- Electron affinity of the insulator, χ_{ox} and
- Bandgap energy of the thin insulator layer, E_g

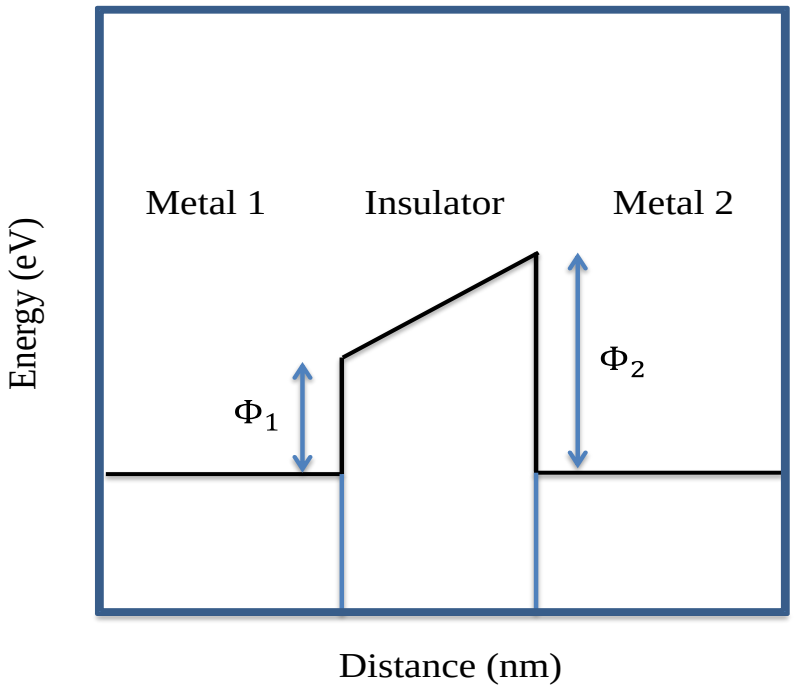

Figure 2.21: Energy band diagram of a MIM diode.

The potential barrier changes according to the externally applied voltages to the diode. Upon applying voltage, the electrons will tunnel from one metal to the other through the insulator. However, at this point, it is important to determine the probability of an electron to tunnel from one energy state to the other through the forbidden band of the insulator. Therefore, tunneling probability of the electron is a function of applied voltage.

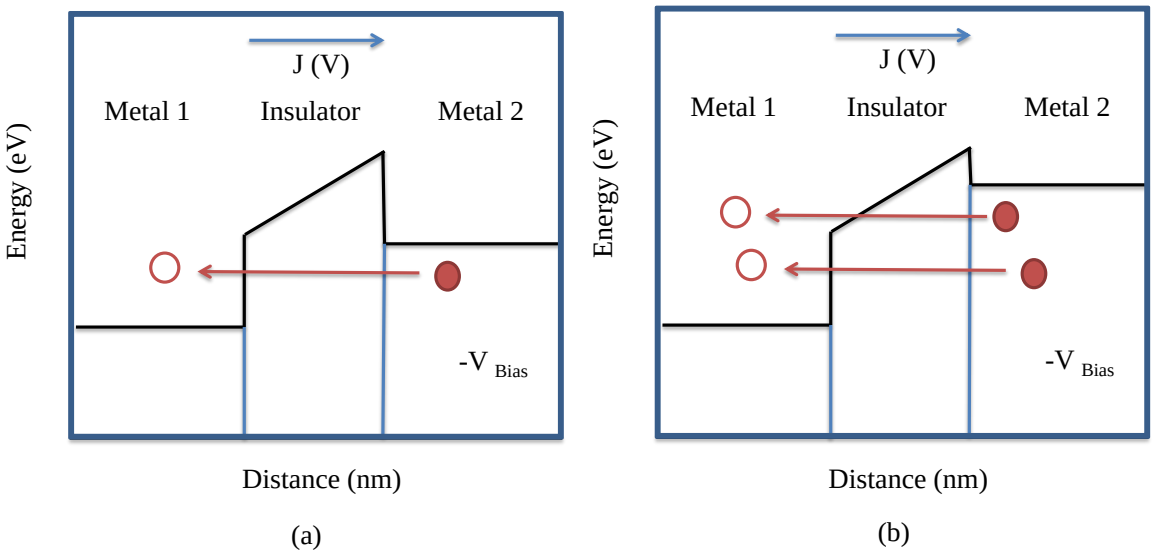

Figure 2.22: (a) Band diagram of MIM diode with a negative bias voltage. (b) Band diagram of MIM diode with further increase in the applied voltage. Tunneling current gets higher due to the decrease in effective thickness of the insulator.

Once the negative voltage is applied on Metal 2, as shown in Fig. 2.21, the band diagram changes i.e. the Fermi level for Metal 2 increases. Therefore, the electrons in Metal 2 tunnel through the insulator to the opposite empty states of Metal 1, as shown in Fig. 2.22(a). As the applied voltage is increased further, there is a decrease in the effective region of the insulator which makes the tunneling distance shorter, as shown in

Fig. 2.22 (b). Consequently, the tunneling current flowing from Metal 1 to Metal 2, increases to a great extent.

However, if a positive voltage is applied on Metal 2, then the shape of the potential barrier will change otherwise and the tunneling current will flow from Metal 2 to Metal 1. Since there is a difference in the work function between the two metals; therefore, the current-voltage characteristic of MIM diode is asymmetric in nature.

2.5 Coupling Efficiency of Rectenna

The rectenna consists of an antenna which receives the EM radiation and generates AC output, followed by a diode which rectifies AC to DC output. Fig.2.23 shows, the small signal model of the rectenna circuit. The conversion efficiency of the rectenna depends on several factors and is given by [13] –

$$\eta = \eta_a \eta_s \eta_c \eta_j, \qquad (2.34)$$

where, η_a is coupling efficiency of incident EM radiation to nanoantenna, η_s is coupling efficiency of propagation energy to the junction of the nanoantenna and diode, η_c is the coupling efficiency of the nanoantenna to diode, and η_j is the efficiency of the rectification by the diode. In fact, η_a and η_s are the efficiencies related to nanoantenna and η_j is the efficiency related to the diode only. In this section, the coupling efficiency of the nanoantenna to the diode η_c is discussed in detail.

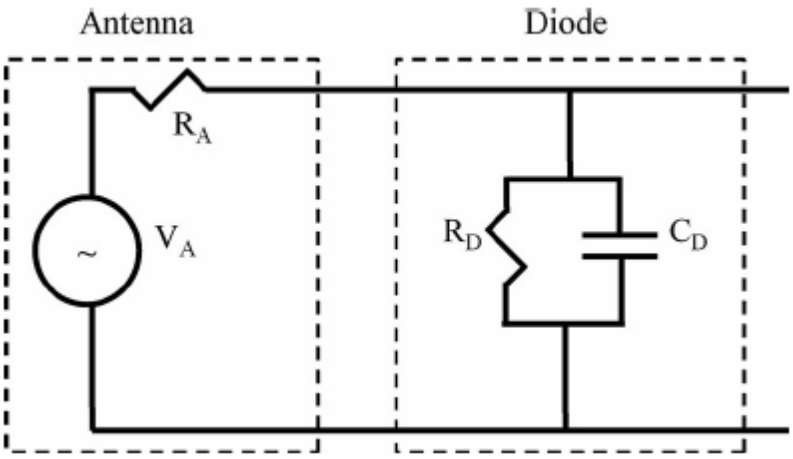

Figure 2.23: The Small signal model of rectenna. The antenna is designed as a voltage source with series resistance and the diode is modeled as parallel RC circuit [58].

The coupling efficiency of the nanoantenna to diode is given by as follows [13], [60]:

$$\eta_c = \frac{P_{AC}}{P_A}, \tag{2.35}$$

where, P_{AC} is the ac power delivered to the diode and P_A is the power of the voltage source of the nanoantenna. The above equation can be written as follows:

$$\eta_c = \frac{\frac{4R_A R_D}{(R_A + R_D)^2}}{1 + \left(\frac{\omega R_A R_D C_D}{R_A + R_D}\right)^2}, \tag{2.36}$$

where, R_A is the resistance of the antenna, R_D is the resistance of the diode, and C_D is the capacitance of the diode.

The parameters such as diode area *A*, the resistance of the nanoantenna R_A, and material composition of the diode can be varied to achieve different conditions leading to different efficiencies. If $R_A = R_D$ and $\omega(R_A||R_D)C_D \ll 1$, these conditions results in unity coupling efficiency, $\eta_c = 1$. It is observed in equation (2.36) that the effect of the impedance matching is characterized by the nominator and the cutoff frequency can be characterized by the denominator of η_c [13].

If the ideal case is considered i.e. $R_A = R_D$ and $\omega(R_A||R_D)C_D = 0$, unity coupling efficiency for different edge length of the diode is shown in Fig. 2.24. The two curves, $\omega(R_A||R_D)C_D$ and R_D/R_A, shown in Fig. 2.24, signifies separately the effect of impedance matching and cutoff frequency. The maximum efficiency occurs at the intersection of the two curves, where the diode edge length is around 10 nm.

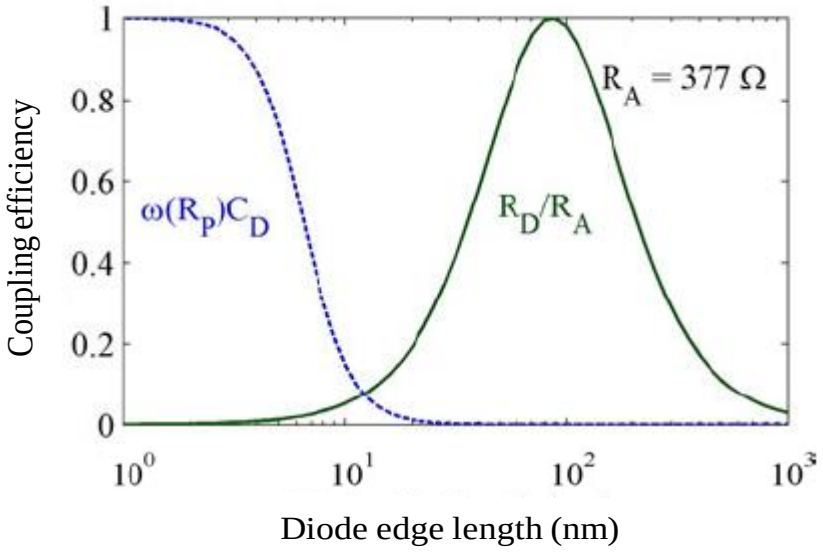

Figure 2.24: Coupling efficiency of the antenna to the diode as a function of diode edge for R_A= 377Ω [56], [13]. R_p is defined as the equivalent resistance of $(R_A \,||\, R_D)$.

In essence, a diode with small resistance gives higher coupling efficiency η_c since it matches with the impedance of the nanoantenna. However, the small resistance of the diode leads to low efficiency in rectification [13]. An increase in the impedance of the nanoantenna allows a higher value of R_D for the diode. Consequently, the area of the diode gets small resulting in a small diode capacitance. However, the equivalent *RC* time constant increases, since R_A is higher. There is no significant improvement in the coupling efficiency, even for higher values of resistance of the antenna, as shown in Fig. 2.25.

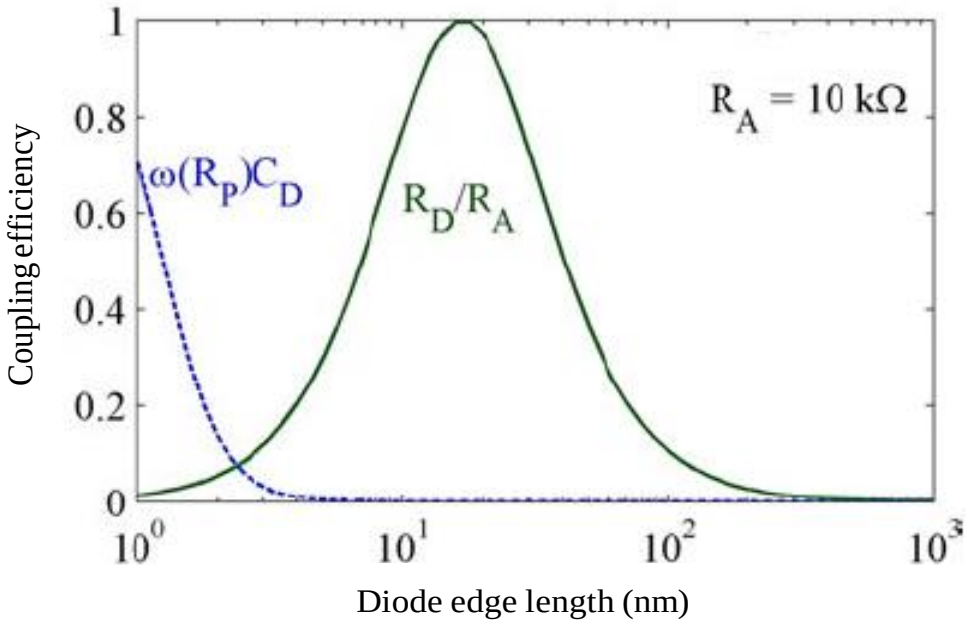

Figure 2.25 : Coupling efficiency of the antenna to the diode as a function of diode edge for R_A=10 kΩ [56], [13]. R_p is defined as the equivalent resistance of $(R_A \,||\, R_D)$.

It can be observed in Fig. 2.25 that for a higher value of R_A , there is no improvement in the efficiency rather the peak-efficiency value shifts (on the left), i.e. to the smaller edge length of the diode.

In order to improve the coupling efficiency, the intersection for both of the curves needs to be at higher value. The $\omega(R_A||R_D)C_D$ curve needs to be shifted to the right and R_A/R_D curve needs to be shifted to the left. In this circumstance, the higher coupling efficiency can be obtained by combining both $R_A = R_D$ and $\omega(R_A||R_D)C_D \ll 1$.

Therefore,

$$\omega(R_A||R_D)C_D \ll 1, \tag{2.37}$$

$$\omega(R_D||R_D)C_D \ll 1, \tag{2.38}$$

$$R_D C_D \ll \frac{2}{\omega}, \tag{2.39}$$

For example, even if R_D of $10^{-8}\Omega.\,\mathrm{cm}^2$ and capacitance of $10^{-7}\mathrm{F/cm}^2$ is assumed, this results in $R_D C_D$ to be around 10^{-15}second or 1.0 femtosecond (fs). However, for visible regime around 428 THz (700 nm), $\frac{2}{\omega}$ results in 0.7 femtoseconds, which theoretically does not show efficient means of coupling at the visible regime.

2.6 Recent Development on Rectennas

The rectenna consists of a nanoantenna as energy collector and a rectifier to rectify the AC output into DC output. Various configurations of the nanoantenna, shown in Fig.2.26, integrated with suitable diodes have been proposed in the literature for energy harvesting applications. The improvement in the efficiency of the rectennas involves the development of antenna design, rectification of the diode, and strong coupling between antenna and diode. Different kinds of nanoantenna that are employed for energy harvesting application are discussed in Table 2.2. Later in this section, we briefly discuss the recent development of the rectenna for energy harvesting applications.

Table 2.2: Different types of nanoantennas in the optical range

Types of Nanoantenna	**Advantages**	**Limitations**	**Incorporated Diode(s) for Energy Harvesting**
1. Dipole	1. High E-field enhancement. 2. Easy to fabricate. 3. Fine tuning.	1. Limited flexibility to increase the E-field.	MIM diode.
2. Bowtie	1. Allows array configuration. 2. More flexibility to increase E-field. 3. Reduces no. of	-	Metal-Oxide-Metal (MOM) diode, MIM diode.

	rectifiers embedded. 4. Wider bandwidth.		
3. Spiral	1. Highest E-field enhancement compared to dipole and bowtie. Capture large amount of E-field with more antenna arms. 2. Polarization: Linear and Circular. 3. For the same gain, square spiral has 75% size of the circular one.	1. Difficult to configure an array. 2. Difficult to lessen no. of rectifier per unit. 3. Difficult to combine E-field in one feeding point.	MIM diode, Esaki diode.

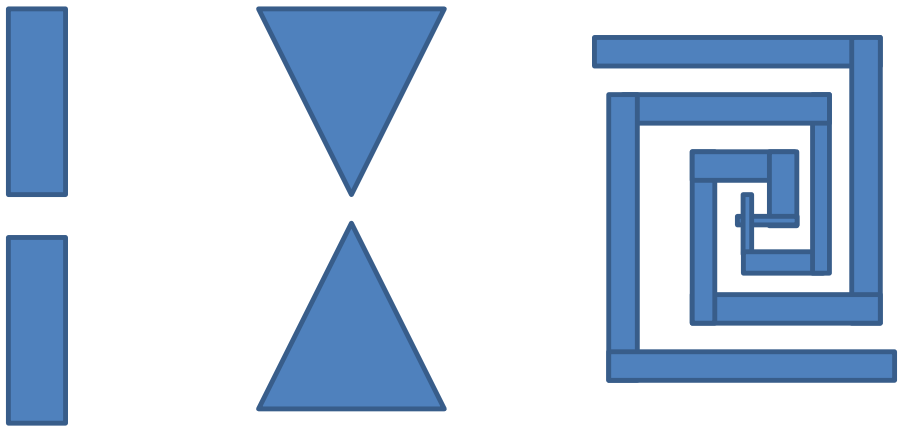

(a) (b) (c)

Figure 2.26: Different structure of nanoantennas (a) Dipole (b) Bowtie (c) Spiral.

Extensive research is still in the exploration phase for the improvement in the efficiency of the rectennas. Some of the research on rectennas based on these types of nanoantenna configurations (i.e. dipole, bowtie, and spiral) has been provided in table 2.3, 2.4, 2.5 as an overview.

Table 2.3: Rectenna based on dipole nanoantenna for IR energy harvesting

Ref.	**Type of Rectifier**	**Materials & Dimension for Nanoantenna & Rectifier**	**Op. Freq.**	**Results/Improvements**
[61]	MIM diode	**Antenna:** Gold (Au) Length: 4.7 μm (inc. gap) **Rectifier:** Au-Insulator-Au (MIM) 50 nm-8.5nm-50 nm (overlapping area) Shown in Fig. 2.27(a)	30 THz	Study Type: Theoretical 1. An integral equation for finding current distribution on the surface of the antenna. 2. The method of Moment, FEM. 3. Parametric study on the effect of the diode's area on captured AC voltage.
[62]	Traveling wave (TW) MIM diode	**Antenna:** Metals. **Rectifier(s):** Ni-NiO-Ni Nb-Nb_2O_5-Nb Ta-Ta_2O_5-Ta 100 nm-2 nm-100nm	-	Study Type: Theoretical 1. Allows good impedance matching between antenna and diode. 2. Characteristic Impedance of the MIM diodes has been compared.

		(overlapping area) Shown in Fig. 2.27(b) &(c)		3. Nb-Nb_2O_5-Nb shows good performance in terms of responsivity.
[7]	Traveling wave (TW) MIM diode	**Antenna:** Gold (Au) & Silver (Ag). Length: $3400\ nm\ \times 2$ **Rectifier(s):** Vertical Coupled Strips (VCS) - 2 nm spacing. Lateral Coupled Strips (LCS) – 20 nm spacing. Shown in Fig. 2.27(d)	30 THz	Study Type: Theoretical 1. TW diode offers good impedance matching to the nanoantenna than the lumped localized rectifier. 2. TW length has to be longer than the plasmon decay to maintain the impedance characteristics of transmission lines. 3. VCS offers efficiency that is nine orders of magnitude higher than LCS due to spacing.

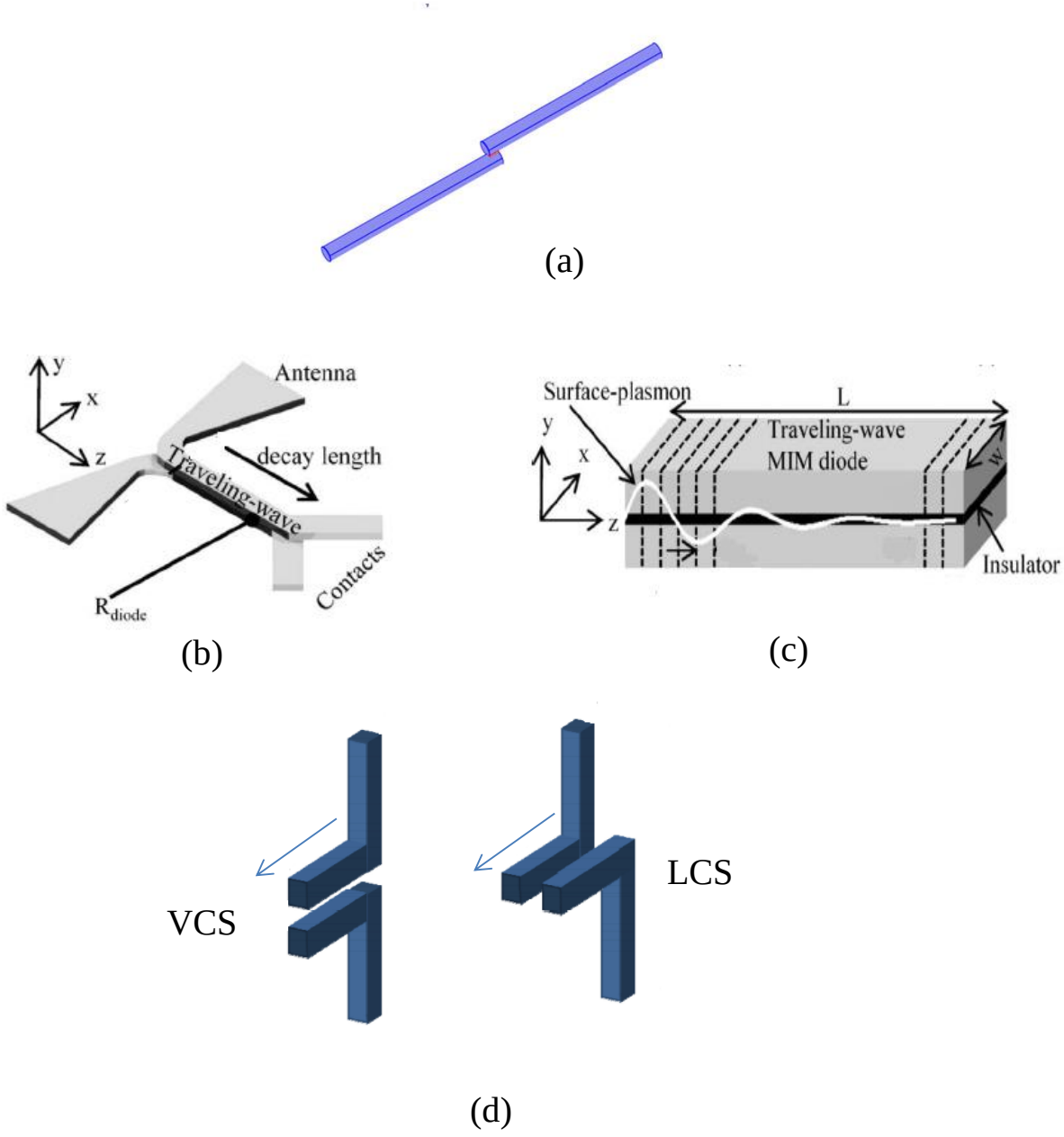

Figure 2.27: (a) Gold dipole nanoantenna incorporated with MIM diode, overlapping (red area) indicates the diode [61]. (b) Antenna integrated with Traveling Wave (TW) MIM diode [62]. (c) Vertical Coupled Strip (VCS) and Lateral Coupled Strips (LCS), blue arrow shows the decay length [7].

Table 2.4: Rectenna based on bowtie nanoantenna for IR energy harvesting

Ref.	Type of Rectifier	Materials & Dimension for Nanoantenna & Rectifier	Op. Freq.	Results/Improvements
[63]	MOM diode	**Antenna:** Gold (Au), Nickel (Ni). Thickness: 35 nm Length & Width: 987 nm, 840 nm. Flare angle: 60°. (misaligned bowtie) **Substrate:** SiO_2 Thickness: 100 nm. **Rectifier:** Ni-NiO-Au Shown in Fig. 2.28 (a).	100 THz	Study type: Theoretical 1. Parameters for the MOM diode have been optimized which improves the efficiency. 2. Ni-NiO-Ni diode shows poor rectification due to impedance mismatch and weak nonlinear I-V characteristics. 3. Ni-NiO-Au offers strong nonlinearity and improves rectification.
[17]	MIM diode	**Antenna:** Gold (Au) Thickness: 100 nm Above Substrate: Chromium (Cr) as an adhesion layer (3 nm). **Substrate:** SiO_2 Thickness: 1.5 μm Below Substrate: Si Thickness: 375 μm	28.3 THz	Study type: Theoretical and Fabrication. 1. A theoretical study has been performed to observe the field enhancement at the gap of the bowtie nanoantenna. 2. Offers high zero bias responsivity (4 A/W) compared to other MIM diode

		(loss reduction) Reflector: Gold (Au) Thickness: 200 nm. **Rectifier:** Au-CuO-Cu (MIM) 95 nm-0.7 nm-100 nm Area: 67 nm × 67 nm. Shown in Fig. 2.28 (b).		(10^{-3} A/W). 3. Offers lower impedance mismatch.
[64]	MIM diode	**Antenna:** Gold (Au) Length: 2.7 μm Thickness: 100 nm **Substrate:** SiO_2 Thickness: 1.5 μm **Rectifier:** Au-Al_2O_3-Pt (MIM) 100 nm-1.4 nm-100 nm Area: 100 nm × 100 nm. Shown in Fig. 2.29(a).	28.3 THz	Study type: Theoretical and Fabrication. 1. Offers high zero bias responsivity 10 A/W due to highly nonlinear I-V characteristics. 2. Optimization of bowtie by producing maximum enhancement at the gap.
[65]	MIM diode	**Antenna:** (Sector Bowtie) Gold (Au)-Titanium (Ti). Length: 3.9 μm. Thickness: 100 nm. Gap: 200 nm.	10-60 THz	Study type: Theoretical 1. Resonance frequency and local field enhancement are affected by the shape of the bowtie (sector).

		Rectifier: Au-TiO_x (5 nm)-Ti Shown in Fig. 2.29(b).		2. The substrate with larger refractive index (Si) leads to higher efficiency. 3. Work function difference between Au and Ti leads to strong nonlinear I-V characteristics. 4. The Higher permittivity of TiO_x leads to a red shift in resonance frequency. To operate at high-frequency permittivity should be reduced.
[66]	Geometric diode.	**Antenna:** Graphene. Length: 5.1 μm. **Rectifier:** Graphene based Inverse arrowhead geometric diode structure. Neck width: 75 nm. Shoulder width: 1μm. Diode length: 500 nm. Shown in Fig. 2.30(a) and (b).	28 THz	Study Type: Theoretical and Fabrication. 1. Requires the critical dimension of the diode should be on the scale of Mean Free Path Length (MFPL). 2. Asymmetric geometry of the diode leads to asymmetric I-V characteristics. 3. Does not suffer from RC time constant. 4. Zero bias responsivity is around 0.12 A/W.

Table 2.5: Rectenna based on spiral nanoantenna for IR energy harvesting

Ref.	Type of Rectifier	Materials & Dimension for Nanoantenna & Rectifier	Op. Freq.	Results/Improvements
[67]	Esaki & MIM diode	**Log periodic Spiral:** Outer radius: 3.6 μm. Bow Angle: 60° Shown in Fig. 2.31(a). **Square Spiral:** Seven Arms Thickness: 200 nm. Arm width: 200 nm. Shown in Fig. 2.31(b). **Archimedean Spiral:** Arm length: 12.4 μm. Width: 200 nm. Thickness: 200 nm. Arm spacing: 560 nm. Radius: 2.4 μm. Shown in Fig. 2.31(c). **Substrate:** SiO_2(1.3 μm) / Si **Rectifier:** n-InAs/AlSb/p-GaSb (Esaki) Al/Al_2O_3/Pt (MIM)	20-60 THz	Study type: Theoretical 1. Efficiency is in the order of 10^{-6} to 10^{-9}. 2. Antenna signal coupled with Esaki diode is 15 times stronger than that of the MIM diodes. However, due to the large capacitance in Esaki diode the efficiency drastically decreases. 3. Efficiency of the spiral nanoantennas coupled with- Esaki diode: 10^{-9} MIM diode: 10^{-12} And square spiral shows the best performance.

[68]	MIM diode	**Antenna:** Titanium (Ti) and Gold (Au) Arm width: 300 nm. Arm spacing: 1 μm (spacing is usually larger than arm's width). Thickness: 100 nm. No. of turns: 2 **Rectifier :** Au-TiO_x (5 nm)-Ti Area: 100 nm × 100 nm. Shown in Fig. 2.31(d).	10-60 THz	Study type: Theoretical 1. Significant redshift and high local field intensity at the resonance due to the increase in the width of the arm. 2. Significant redshift and high local field intensity at the resonance due to the increase in spacing between the arms. 3. Current flow depending on diode contact area- 50 nm × 50 nm: 24 nA. 200 nm × 200 nm: 4 nA. 4. The resonance frequency can be modulated by changes in the oxide level of the dielectric layer (TiO_x); since oxide level controls the conductivity of the layer.

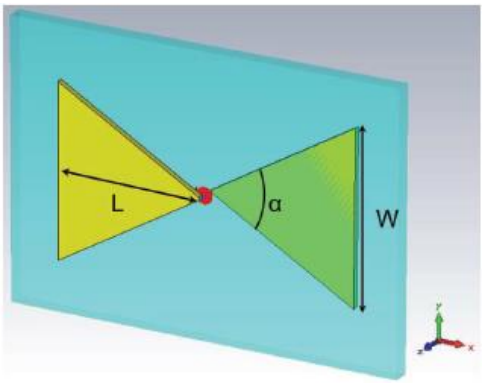

(a)

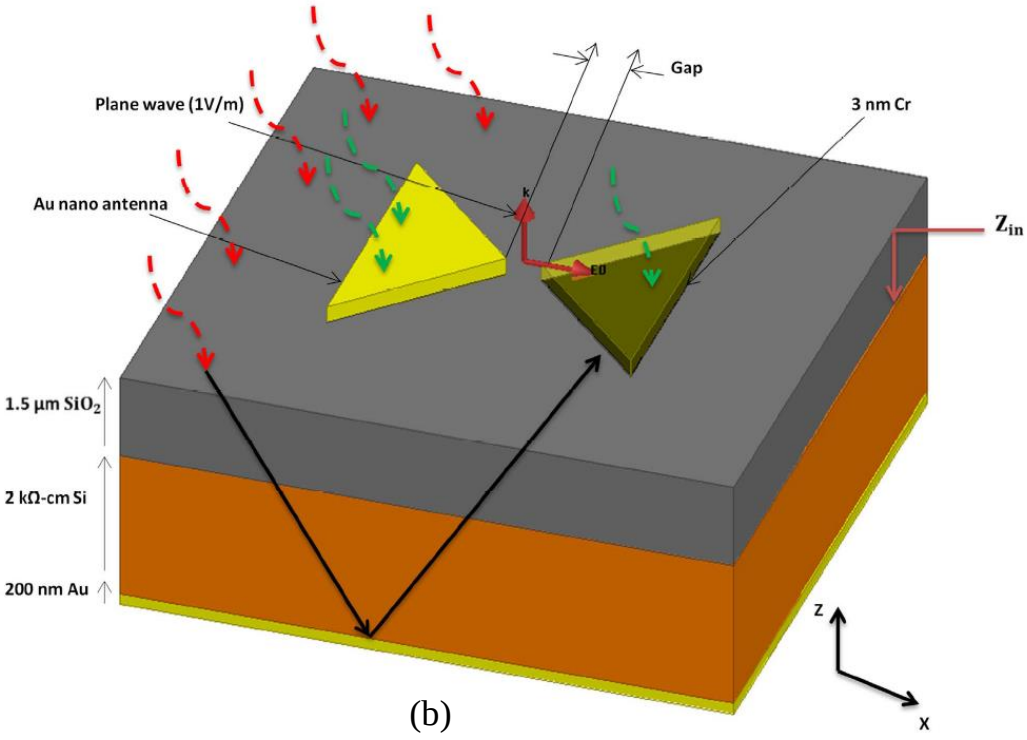

(b)

Figure 2.28: (a) Misaligned bowtie nanoantenna on Si substrate [63]. (b) Gold nanoantenna on chromium adhesion layer. SiO_2 is employed on the Si substrate as a matching section. Gold at the bottom of the substrate is working as a good reflector. The black arrow indicates the reflective wave, green arrows indicate the coupled wave and red arrows indicate the incident waves on the matching section [17].

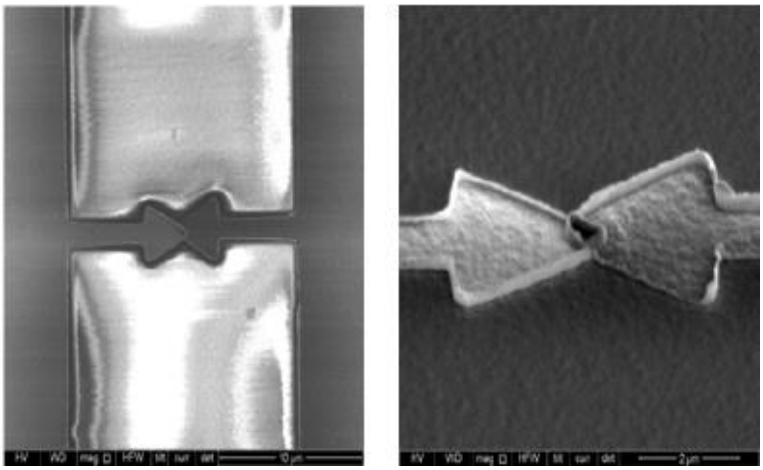

(a)

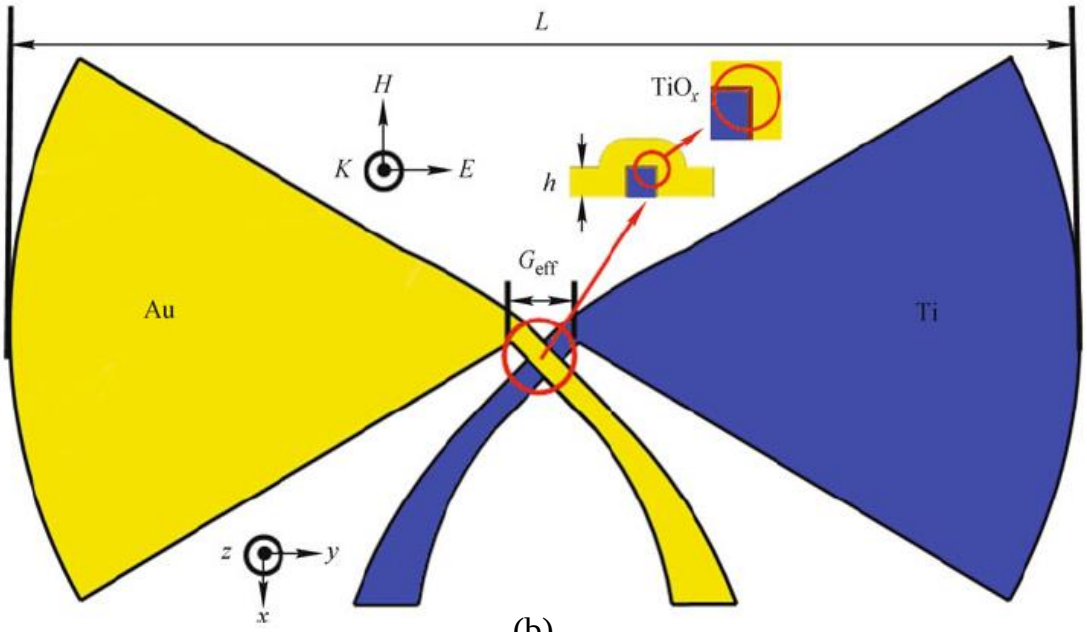

(b)

Figure 2.29: (a) SEM images for the overlapped bowtie with 2.7 μm arm length and 50° flare angle [64]. (b) The design of a sector bowtie nanoantenna incorporated with Au-TiO_x-Ti (MIM) diode [65].

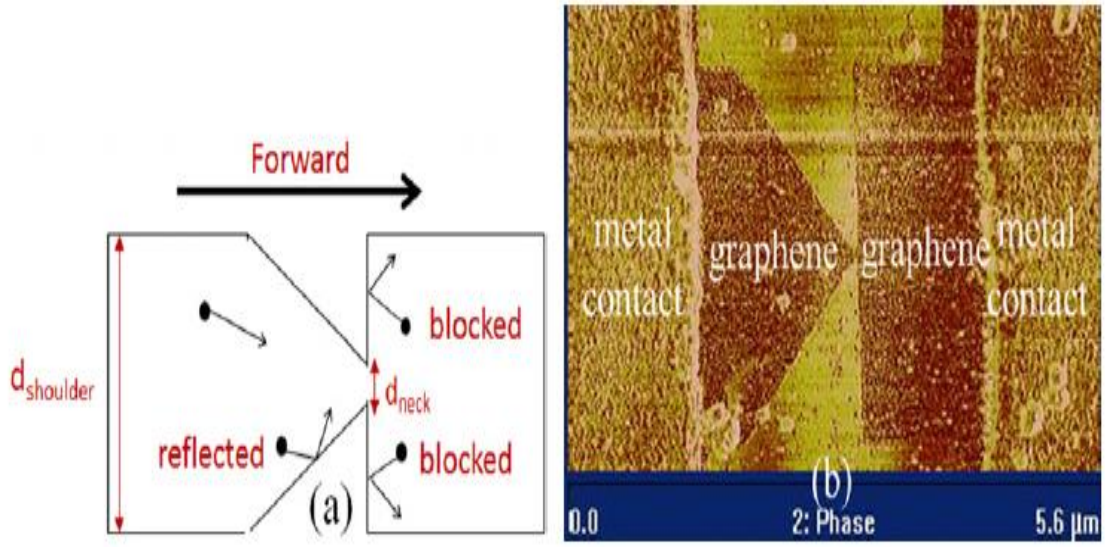

Figure 2.30: (a) Structure of inverse arrowhead geometric diode, the dimension of the neck region i.e. d_{neck} = 75 nm, is in the scale of the MFPL for the charge carriers, and $d_{shoulder}$ = 1µm. (b) AFM image of the fabricated graphene geometric diode. The thickness of the graphene between the two metal contacts is around 0.5 nm to 1 nm [66].

Recently, a novel structure, Crescent nanoantenna [69], is proposed for energy harvesting. Parametric studies, given in table 2.6, were performed to have an insight about the spectral response and optimization of the antenna.

Table 2.6: Recent development of crescent nanoantenna

Ref.	Materials & Dimension for Nanoantenna (NA)	Op. Freq.	Results/Improvements
[69]	**Antenna:** Gold Thickness: 30 nm. Overall Size: 800 nm × 800 nm. Narrow Gap: 20 nm. Outer circle radius: 670 nm. Inner circle radius: 430 nm. Shown in Fig. 2.32(a).	120 THz	Study Type: Theoretical 1. Two resonances occur at two different wavelengths. 2. The radius of the inner and outer circle controls the location of resonances. A big difference in the radius of inner and outer aperture results in isolated bands. 3. A Higher value of refractive index of the substrate leads to redshift and enhancement at the resonance.
[70]	**Antenna:** Gold Thickness: 30 nm Narrow Gap: 20 nm. Inner patch: Major axis: 430 nm Outer aperture: Major axis: 670 nm Shown in Fig. 2.32(b).	125-300 THz	Study Type: Theoretical 1. Crescent nanoantenna with ellipse has been employed instead of circle. 2. Axial ratio is able to control the enhancement and bandwidth of the nanoantenna.

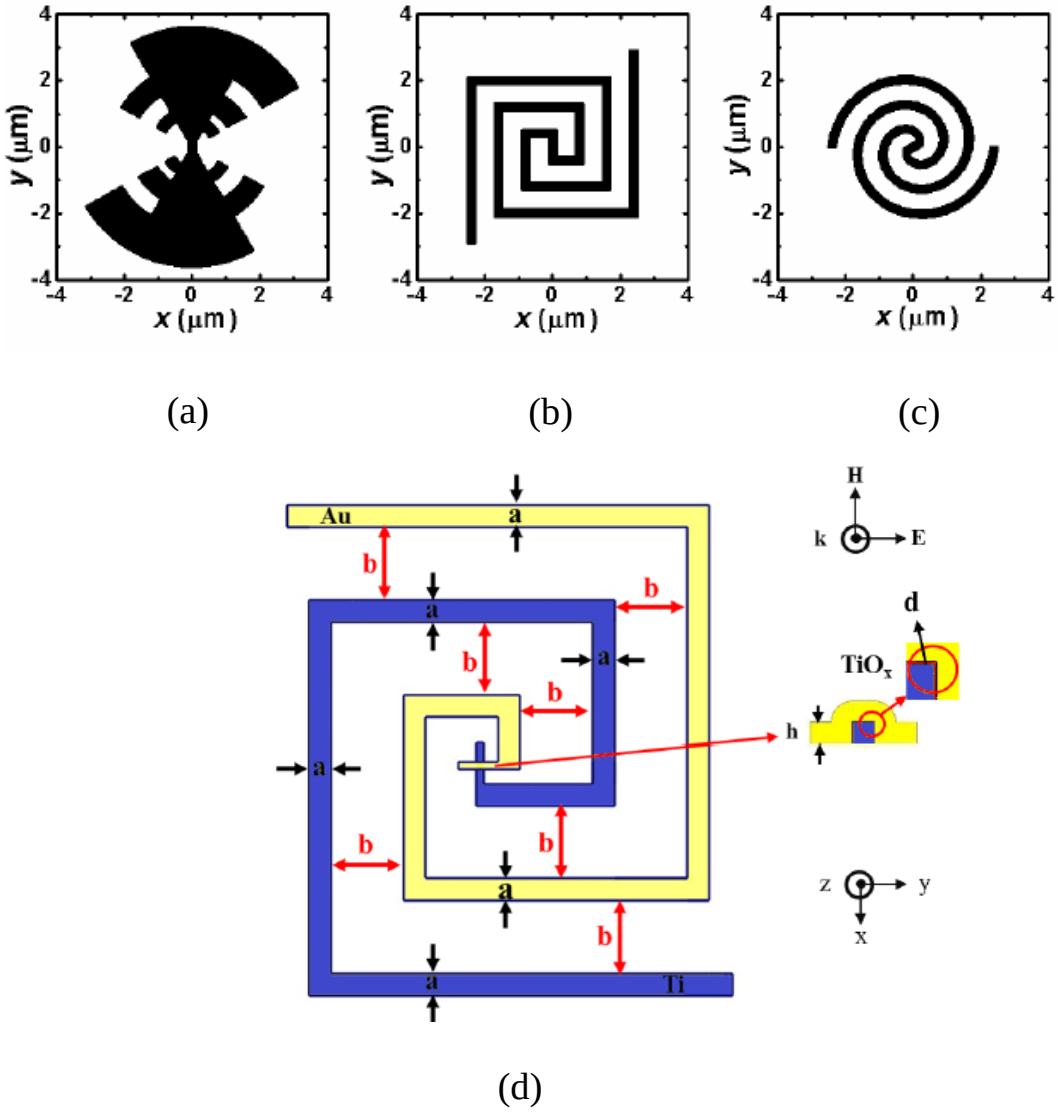

Figure 2.31: Structure of (a) Log Periodic Spiral Nanoantenna [67]. (b) Square Spiral Nanoantenna [67]. (c) Archimedean Spiral Nanoantenna [67]. (d) Square Spiral incorporated with Au-TiO_x-Ti (MIM) diode where a = 300 nm, b = 1μm, h= 100 nm and d = 5 nm [68].

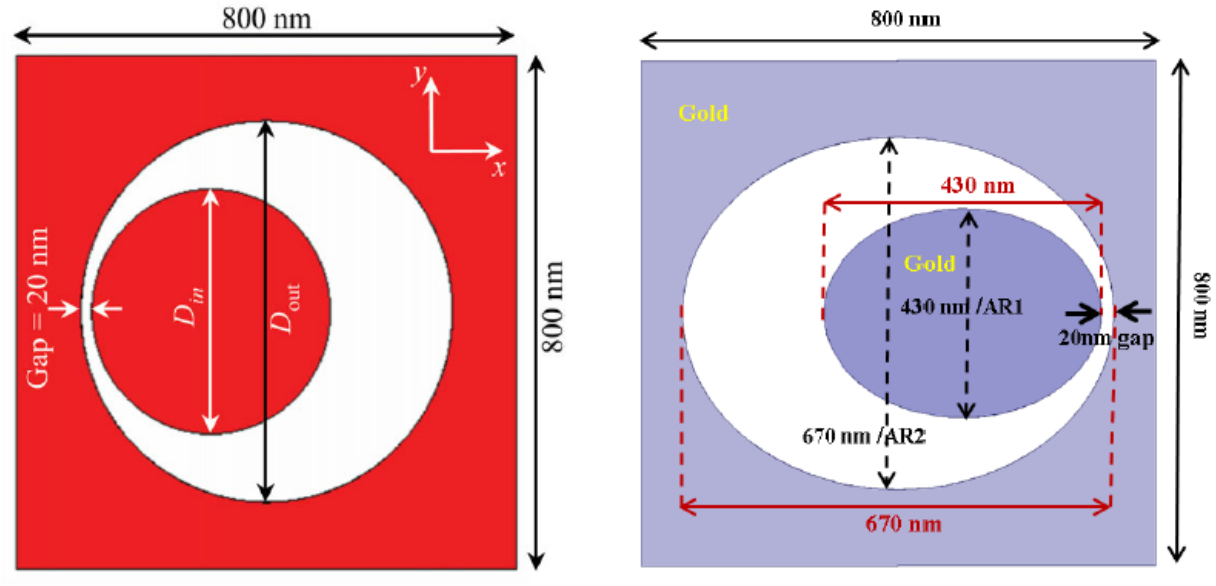

(a) (b)

Figure 2.32: Top view of (a) Crescent nanoantenna with inner circular patch, D_{in} = 430 nm and D_{out} = 670 nm [69]. (b) Crescent nanoantenna with inner elliptical patch, major axis for outer and inner ellipse is 670 nm and 430 nm [70].

2.7 Fundamental Limitation of MIM Diodes

There are some fundamental trade-offs between the electrical parameters of the MIM diodes. Changing one of the parameters might affect other parameters in such a way that changes the overall characteristics of the MIM diode. Some of the fundamental trade-offs and limitations of MIM diode are discussed in this section. The operating frequency is related to the electrical parameters of the diode and nanoantenna.

The operating frequency is expressed in terms of electrical parameters as follows:

$$f = \frac{1}{2\pi R_p C_D}, \qquad (2.40)$$

where, f is the operating frequency, R_p is the equivalent resistance, C_D is the capacitance. Here, $R_p C_D$ is called the equivalent time-constant. The parameter R_p can be written as $(R_A \parallel R_D)$.

The operating frequency is inversely proportional to the time-constant. The tunneling process for an electron takes femtoseconds (10^{-15} sec.). Therefore, in order to perform rectification at the high-frequency regime, the time-constant needs to be in the scale of femtoseconds (10^{-15} sec.).

However, there are some trade-offs of the MIM diodes, they are as follows:

- The quality of the rectification depends on the resistance of the MIM diode R_D. A diode with high resistance results in high efficiency rectification, whereas diode with small resistance shows low efficiency. The resistance of the diode can be increased by increasing the thickness of the insulator layer of the MIM diode. However, the probability of tunneling of an electron exponentially decreases with the increase in the thickness of the insulator.

- Impedance matching becomes another challenge while performing rectification at high-frequency regime using MIM diodes. The nanoantenna collects the incident EM waves and produces highly localized electric field. In order to transfer the

maximum power from nanoantenna to diode and to perform efficient rectification, it is very crucial to match the impedance of the nanoantenna to the MIM diode. However, to perform rectification in an efficient way, the resistance of the MIM diode needs to be high whereas the typical resistance of the nanoantenna is few hundred ohms. Therefore, impedance matching becomes a serious problem.

- In order to reduce the resistance of the diode, the thickness of the insulator of MIM diode needs to be reduced. However, the small thickness of the insulator results in large capacitance which apparently affects the equivalent time-constant.

- The $R_p C_D$ time constant can be made small to operate at high frequency by making both the resistance and capacitance as small as possible of the MIM diode. Thin insulator layer and junction area of the MIM diode leads to both small resistance and capacitance. This also serves the purpose of impedance matching. However, the practical realization of small contact area and the very thin insulator layer is often challenging in the fabrication process.

Due to these limitations in the rectenna; especially, in the rectification part, the efficiency of the rectenna for energy harvesting is very low compared to its microwave counterpart. It is very important to improve the rectification part of the rectenna in order to obtain higher efficiency. Therefore, in this report, we have proposed a novel approach

to harvest energy using nanoantenna without using MIM diode. A detailed discussion on our proposed novel energy harvester is discussed in the next two chapters.

CHAPTER 3

3. Parameterization of Dual Polarized Nanoantenna

There are some major challenges and limitations facing THz and infrared rectennas. Firstly, one of the major challenges involved with rectennas is the rectification process. In order to perform rectification at high-frequency regime, the equivalent RC time-constant of the MIM diode needs to be on the scale of femtoseconds. Secondly, the efficiency of the rectification depends on the impedance matching between nanoantenna and diode. High efficiency rectification is obtained by using a diode of high resistance, whereas the resistance of the nanoantenna is usually small. Due to the limitation of equivalent RC time-constant and impedance matching, MIM-based rectennas results in low efficiency at high frequency. Recent reports demonstrated improved performances of $Au/CuO/Au$ symmetric MIM diode [17] and $Au/Al_2O_3/Pt$ asymmetric MIM diode [64] by making small contact area i.e. $67\ nm \times 67\ nm$ and a very thin oxide layer i.e. 3 nm of MIM diode. MIM diode of small dimension leads to small RC time-constant. Nevertheless, it results in low efficiency rectification with small resistance. Finally, the realization of a small contact area and thin oxide layer makes it practically very challenging in the fabrication process. Since, these challenges cannot be addressed completely with the existing technologies, there is a demand for a new approach to perform rectification at THz, infrared, or visible regime.

We propose a novel energy harvester which converts solar electromagnetic radiation at high frequency into DC energy without using MIM diodes. The proposed device consists of a dual polarized nanoantenna loaded with an anisotropic material of nonlinear electrical conductivity at its gap. The dual polarized nanoantenna focuses the randomly polarized radiation into its gap resulting in a high electric field. The anisotropic material at the gap converts the dual polarizations into a DC voltage difference across the terminals of the nanoantenna. A detailed discussion on our proposed energy harvester is provided in the next chapter.

The theory of the proposed energy harvester depends on the utilization of dual polarized nanoantenna. Cross bowtie nanoantenna is used for proposed energy harvester. Therefore, in this chapter, we carry out a parametric study to investigate the resonance characteristics of the dual polarized cross bowtie nanoantenna. The effect of the geometrical parameters on the local field enhancement at the gap for dual polarized nanoantenna is also investigated. The local field enhancement at the gap for single and dual polarized bowtie nanoantennas is compared for specific dimension.

The fine features of the optical nanoantenna make numerical analysis challenging. The nano-sized rectenna and strong dispersion of the metals at IR and visible regime become demanding for numerical simulation and computation. Therefore, the selection of software to simulate nanoantennas is critical at the initial stage; especially, when the spatial separation between the structures is few nanometers. Nowadays, numerous commercial software packages are used to simulate the properties of nanoantennas in

THz, infrared, and visible regime. COMSOL Multiphysics software [71] that works based on Finite Element Method (FEM) is used to simulate our proposed energy harvester in infrared regime.

3.1. Operation Principle of Bowtie Nanoantenna

Bowtie nanoantenna consists of two nanostructured triangles facing each other tip-to-tip with a spatial separation gap in between, as shown in Fig. 3.1. The local electric field is typically concentrated at the gap of the bowtie nanoantenna [49]. Bowtie nanoantenna offers several advantages over other types of structures. It offers broad bandwidth and lower confinement factor [72]. Moreover, bowtie nanoantenna of the same configuration can be employed as an array. This allows the electric field from each element to combine at array feeding point.

The operation mechanism of bowtie nanoantenna can be discussed as follows: Here, at first, we discuss the reception function of the nanostructured device. In essence, when an incoming plane wave illuminates perpendicularly on the bowtie nanoantenna, shown in Fig. 3.1, it creates Surface Plasmon Polaritons (SPPs) i.e. free electron oscillation which propagates along the interface between the metal and the surrounding dielectric region. Consequently, strong local field confinement is achieved at the gap of the bowtie nanoantenna. This gap is utilized either as an electrical feeding point or reception point for the nanoantenna. High-frequency current flows on the surface of the nanoantenna towards this point.

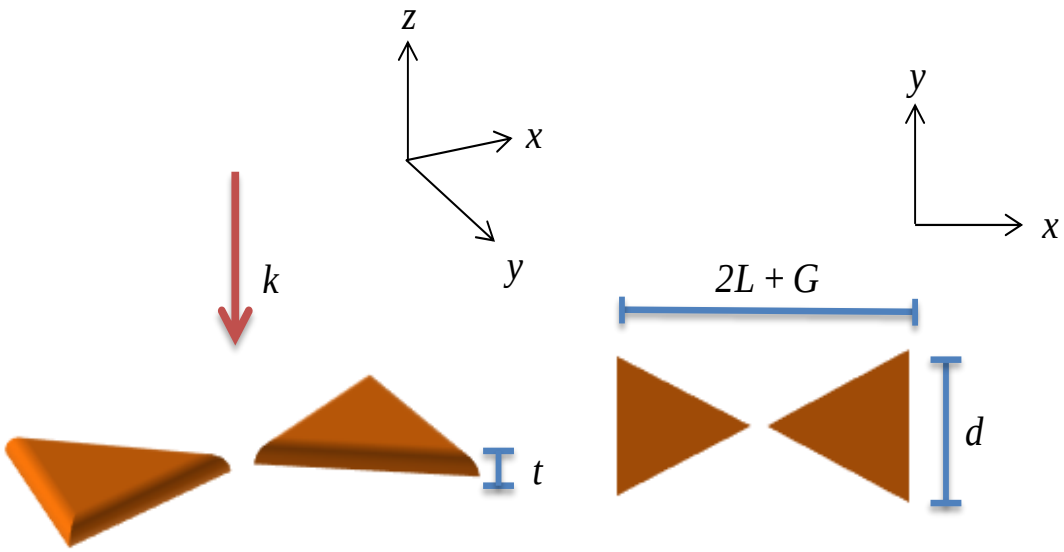

Figure 3.1: Structure of a regular bowtie nanoantenna (a) side view (b) top view.

However, bowtie nanoantenna is polarization-dependent and it focuses electromagnetic radiation into localized electric field when the polarization is parallel to the dipole axis.

The local electric field enhancement at the gap of the bowtie nanoantenna is investigated using RF module of COMSOL Multiphysics, version 5.1 [71]. The simulation is performed using frequency domain analysis. The geometrical dimensions of bowtie nanoantenna for our simulation are given in Table 3.1. The relative permittivity of the metal becomes dispersive i.e. a function of frequency at high frequency regime. Therefore, Drude model [38] is used to estimate the complex permittivity of the metal. The nanoantennas in our simulation are composed of gold. Therefore, Drude-parameters for gold are given in Table 3.2.

Table 3.1: Dimensions for the bowtie nanoantenna

Geometrical Parameters of Bowtie Nanoantenna	**Parameter Values**
Length, *L*	1.0 μm
Width, *d*	1.0 μm
Gap size, *G*	50 nm
Thickness, *t*	30 nm

Fig. 3.2 shows that the resonance frequency of the bowtie nanoantenna is around 95 THz with a local field enhancement of 50 V/m. We excited the bowtie nanoantenna using *x*-polarized plane wave in our simulation. Therefore, the local field enhancement at the gap is only parallel to *x* axis.

Table 3.2: Drude-parameters for gold

Drude Parameter	**Parameter Values**
Relative Permittivity, $\boldsymbol{\varepsilon_r}$	9.069
Plasma Oscillation Frequency, $\boldsymbol{\omega_p}$	1.354×10^{16} rad/s
Plasma Collision Frequency, γ	1.2×10^{14} rad/s

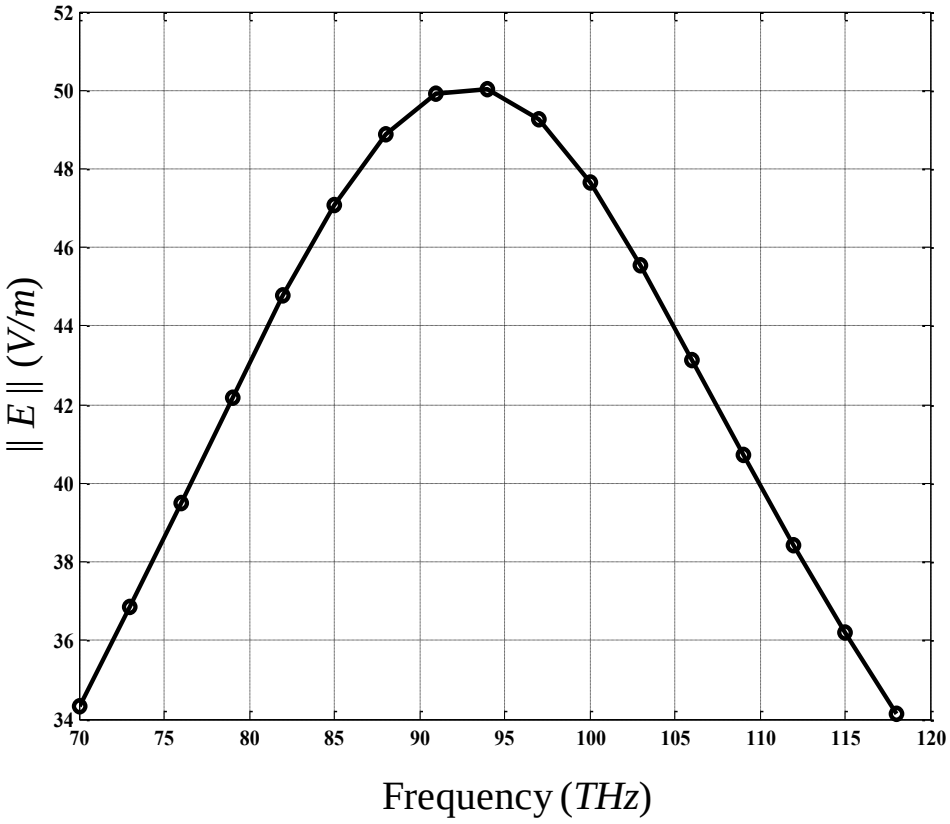

Figure 3.2: Local field enhancement at the gap of the bowtie nanoantenna for L = 1.0 μm, d = 1.0 μm, and G = 50 nm.

The bowtie nanoantenna focuses the polarized, i.e. *x* polarization, electromagnetic radiation into strong localized electric field at the gap. Most of the electric field is concentrated at the gap and a small portion of the electric field is found at the edges of the bowtie structure. The intensity of the local field at the gap of the bowtie nanoantenna for the same specified dimension is shown in Fig. 3.3. The intensity of the local field is found to be 2500 V^2/m^2 at the resonance frequency.

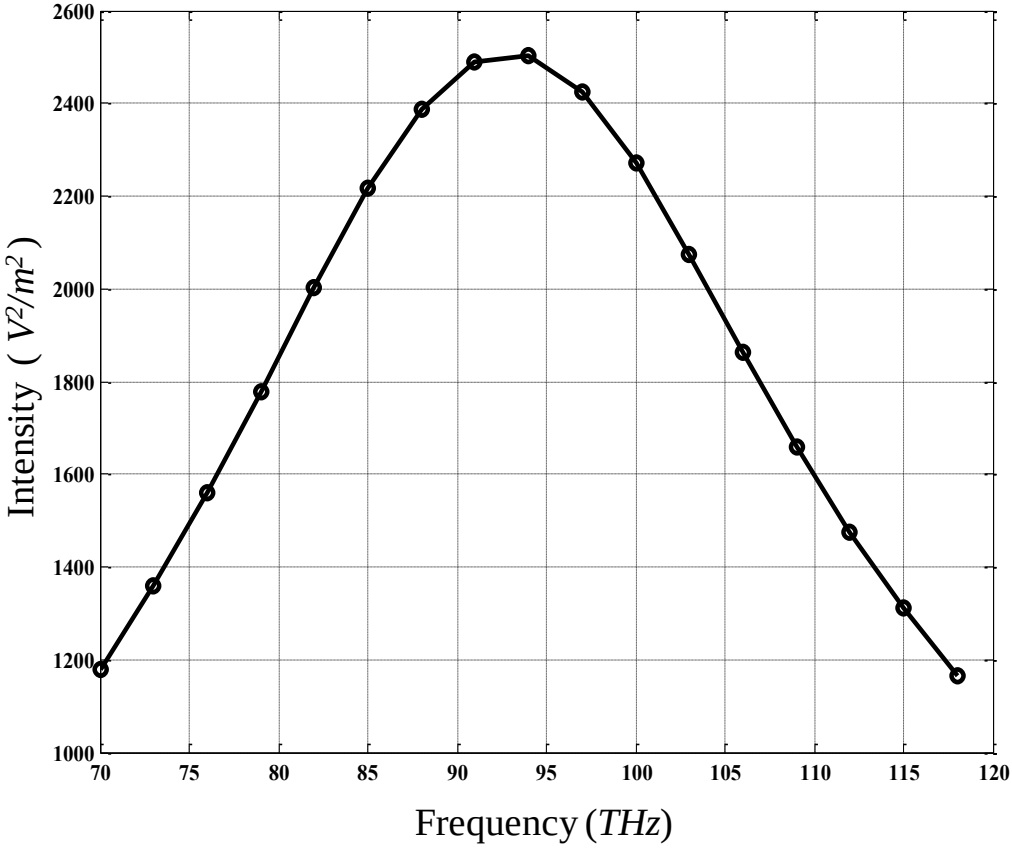

Figure 3.3: Intensity of the local field enhancement at the gap of the bowtie nanoantenna for L = 1.0 μm, d = 1.0 μm, and G = 50 nm.

Since the bowtie nanoantenna is polarization-dependent, different kind of structures of bowtie nanoantenna [72] have been proposed to harvest energy efficiently from solar electromagnetic radiation. Recently, it is reported that the cross bowtie nanoantenna shows the best performance [73] for solar energy harvesting in the optical and infrared regime compared to the other nanoantennas of different shapes. Fig. 3.4 shows the comparison of field enhancement at the gap for different kind of nanoantennas operating at infrared regime. However, there are not much research works in the literature on cross

bowtie nanoantenna for energy harvesting applications. In this chapter, we, therefore, focus on dual polarized cross bowtie nanoantenna and its resonance characteristics for energy harvesting in an efficient way.

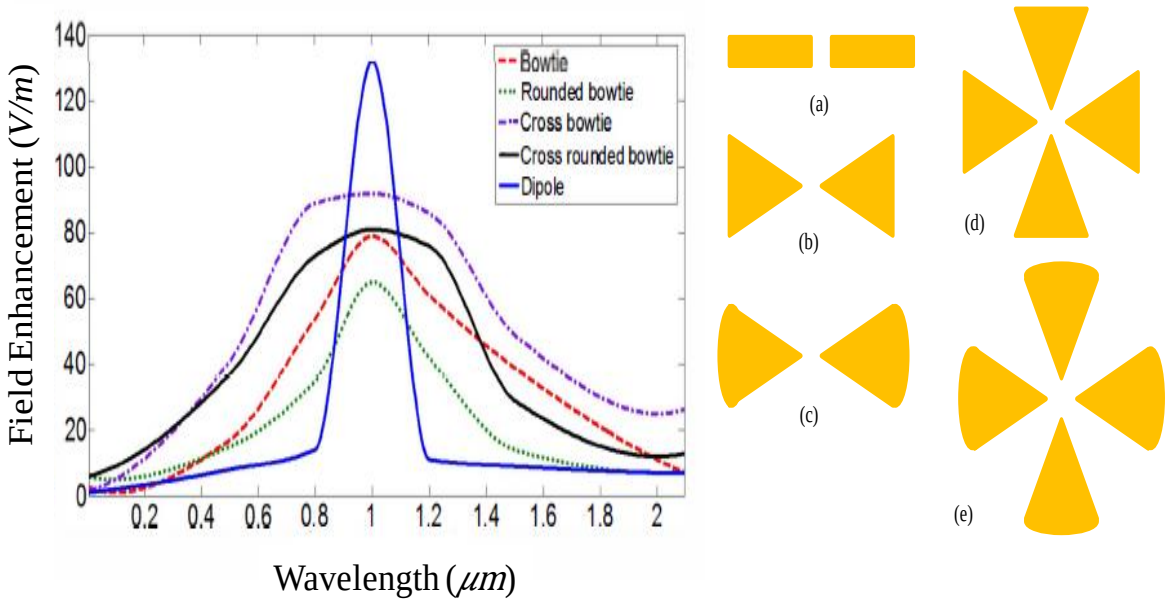

Figure 3.4: Local field enhancement at the gap for different shapes of nanoantenna; top view of (a) dipole (b) Bowtie (c) Rounded-Bowtie (d) Cross Bowtie (e) Cross Rounded-Bowtie [73].

3.2. Dual Polarized Cross Bowtie Nanoantenna

Cross bowtie nanoantenna consists of two pairs of bowtie which are spatially orthogonal to each other and sharing a common gap, as shown in Fig. 3.5.

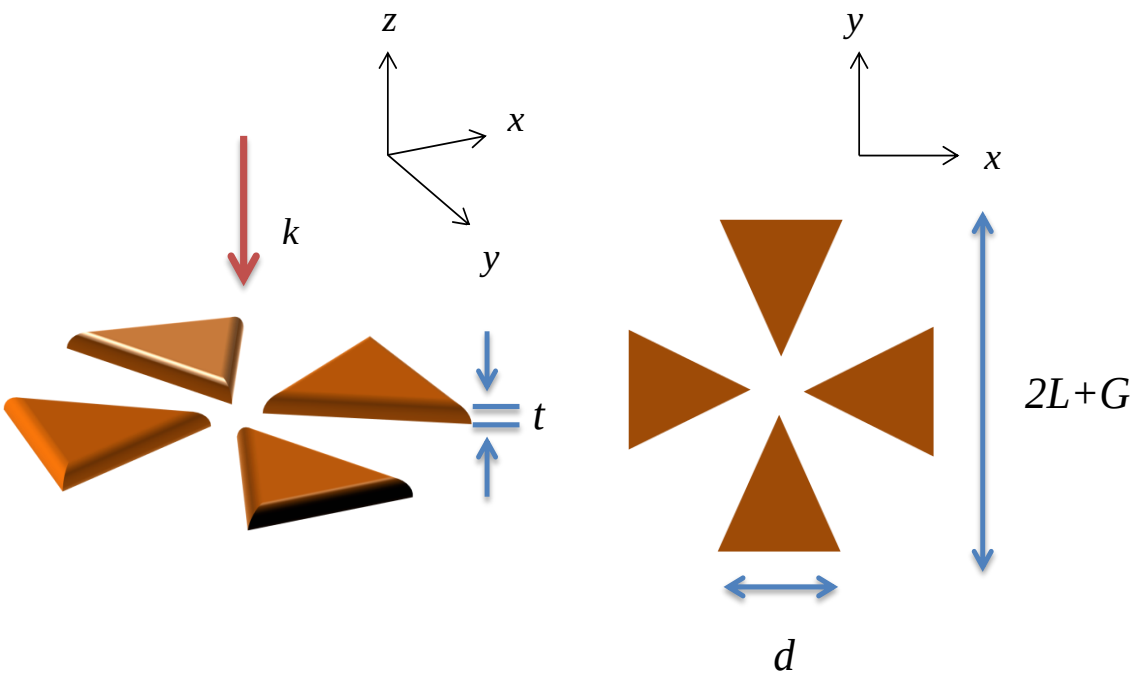

Figure 3.5: Structure of dual polarized cross bowtie nanoantenna (a) side view (b) top view.

The operation mechanism of cross bowtie nanoantenna is almost similar to the regular bowtie and can be discussed as follows: When an incoming plane wave of orthogonal polarization (*x* and *y* polarization) illuminates perpendicularly on the cross bowtie nanoantenna, as shown in Fig. 3.6, it creates Surface Plasmon Polaritons (SPPs) i.e. free electron oscillation which propagates along the interface between the metal and

surrounding dielectric region. As a result, strong local field confinement is achieved in the gap. One of the advantages which can be obtained by using the cross bowtie nanoantenna over the regular bowtie is it focuses randomly polarized electromagnetic radiation into its gap. It does not depend on the polarization of the incoming light.

We investigate the local electric field enhancement at the gap for dual polarized cross bowtie nanoantenna using RF module of COMSOL Multiphysics, version 5.1. The geometrical dimensions of the dual polarized cross bowtie nanoantenna are given in Table 3.3. Drude model is used to estimate the complex permittivity of the gold since it becomes dispersive, i.e. frequency-dependent, in THz or infrared regime. The Drude-parameters for gold are given in Table 3.2.

Table 3.3: Dimensions for the cross bowtie nanoantenna

Geometrical Parameter of Cross Bowtie Nanoantenna	**Parameter Values**
Length, *L*	1.0 μm
Width, *d*	1.0 μm
Gap size, G	50 nm
Thickness, t	30 nm

Fig. 3.6 shows that the resonance frequency for the dual polarized cross bowtie nanoantenna is around 100 THz with a maximum local field enhancement of 64 V/m for

specified dimensions. Most of the electric field is concentrated at the gap and a very small portion of the electric field is found surrounding the structure.

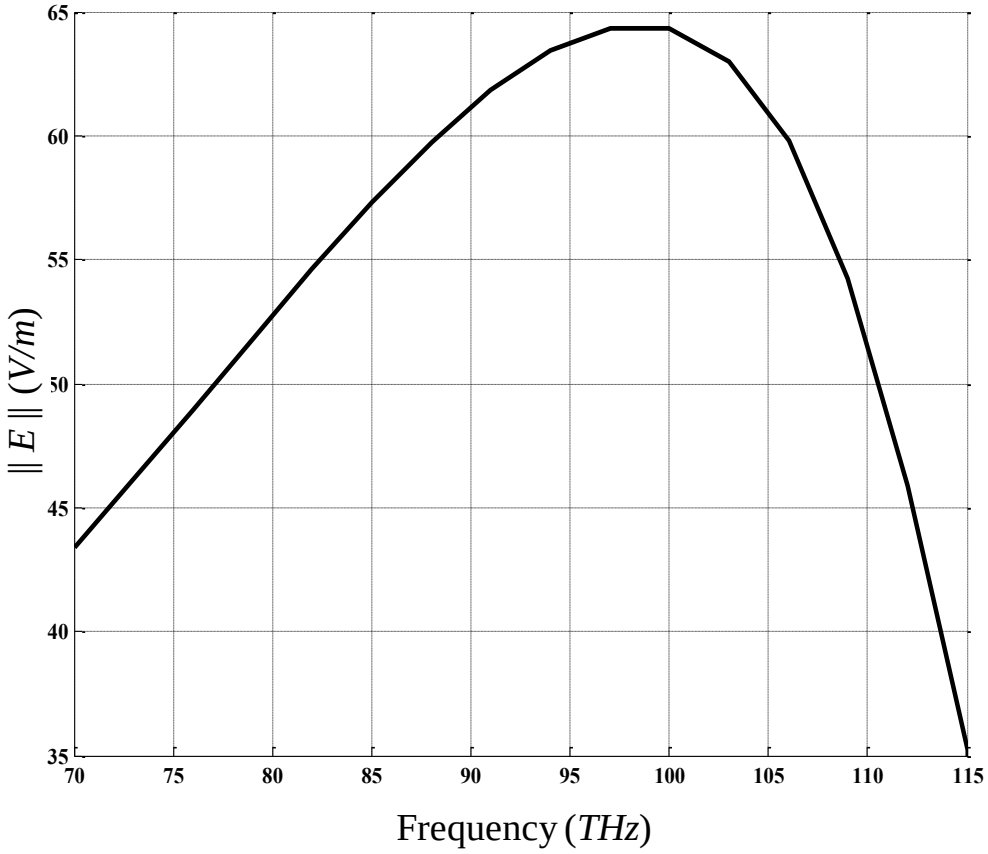

Figure 3.6: Local field enhancement at the gap of the dual polarized cross bowtie nanoantenna for L = 1.0 μm, d =1.0 μm, and G = 50 nm.

Fig. 3.7 shows the intensity of the dual polarized cross bowtie nanoantenna. The intensity of the local field is around 4000 V^2/m^2 at the resonance frequency.

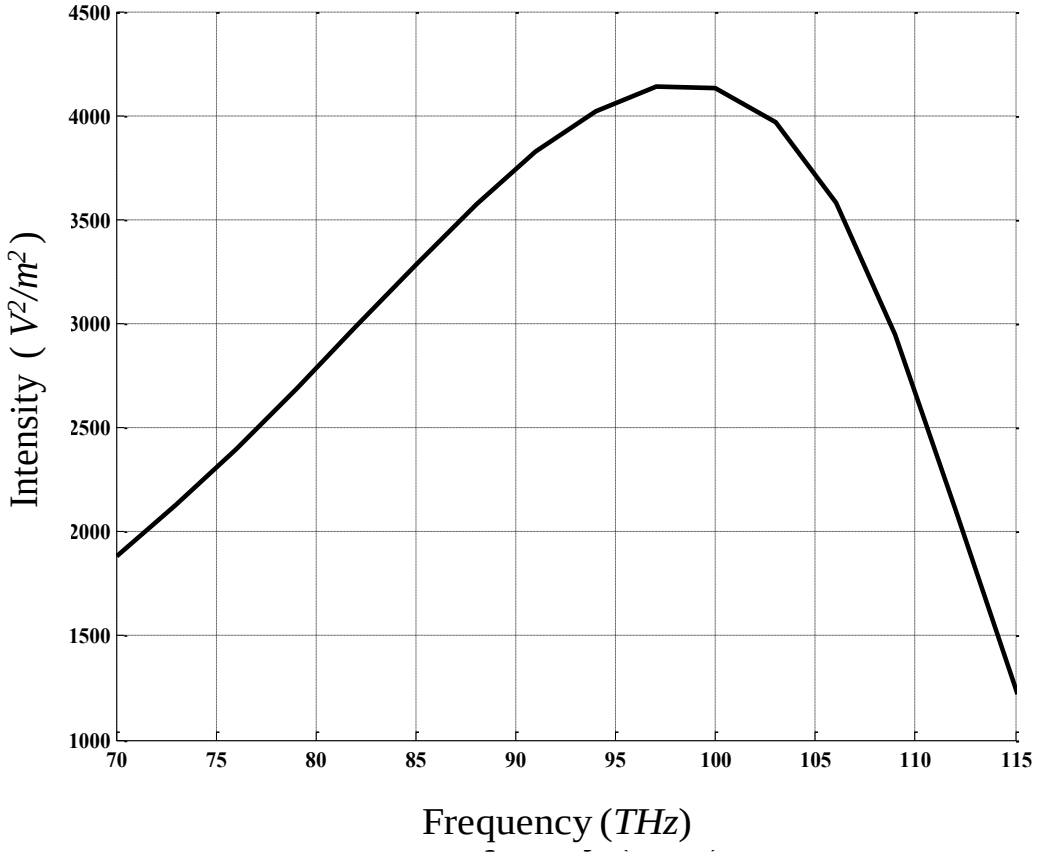

Figure 3.7: Intensity of the local field enhancement at the gap of the dual polarized cross bowtie nanoantenna for L = 1.0 μm, d = 1.0 μm, and G = 50 nm.

3.3. Comparison of Local Field Enhancement at the Gap

We investigated the local field enhancement at the gap for both bowtie and cross bowtie nanoantenna in the previous section. In this section, we compare the local field enhancement at the gap for these two different nanoantenna for the dimensions specified in Table 3.2.and Table 3.3.

Fig. 3.8 shows that the local field enhancement at the gap for cross bowtie nanoantenna is much higher than the regular bowtie nanoantenna. The local field enhancement for dual polarized cross bowtie is around 65 V/m, whereas for single polarized bowtie nanoantenna, it is around 50 V/m. The resonance frequency for the dual polarized cross bowtie nanoantenna is shifted slightly to a higher frequency (to the right) compared to the resonance frequency of the single-polarized bowtie nanoantenna.

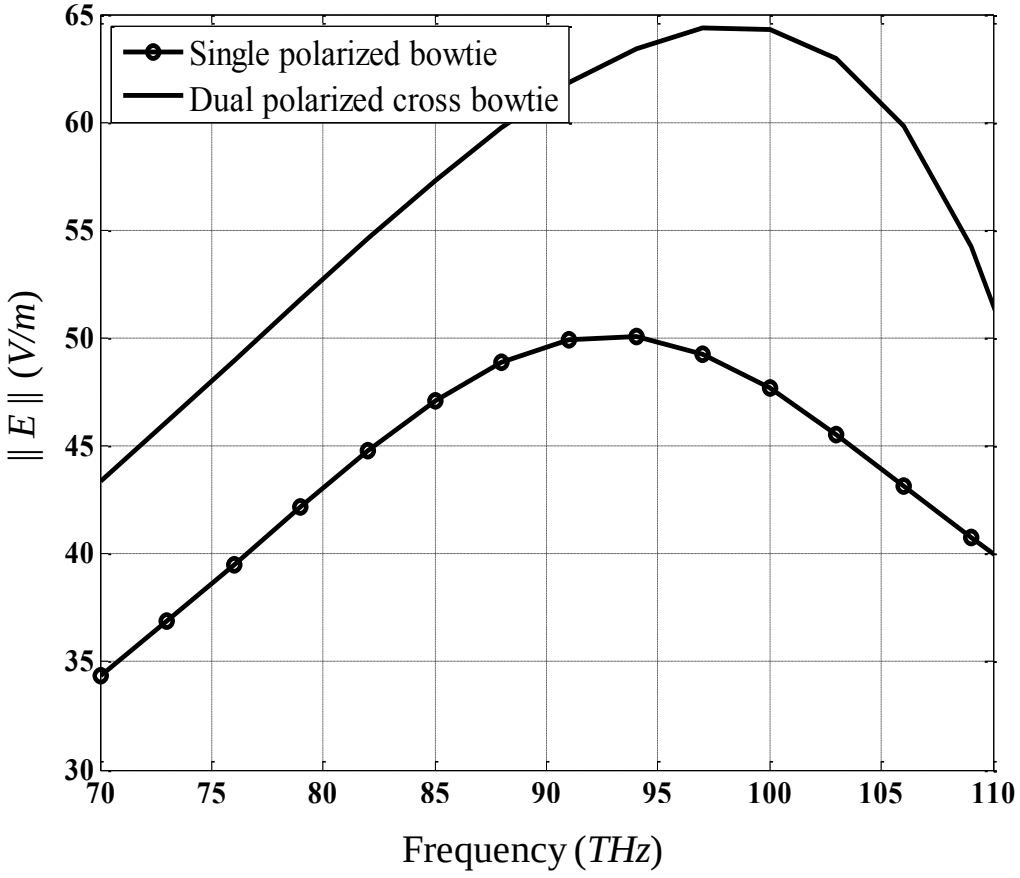

Figure 3.8: Comparison of local field enhancement at the gap for single polarized bowtie and dual polarized cross bowtie nanoantenna for L =1.0 μm, d =1.0 μm, and G = 50 nm.

Fig. 3.9 shows the comparison of the local field intensity at the gap between cross bowtie and regular bowtie nanoantenna. The intensity of the local field for dual polarized cross bowtie is around 4200 V^2/m^2, whereas for single polarized bowtie nanoantenna, it is around 2500 V^2/m^2 .

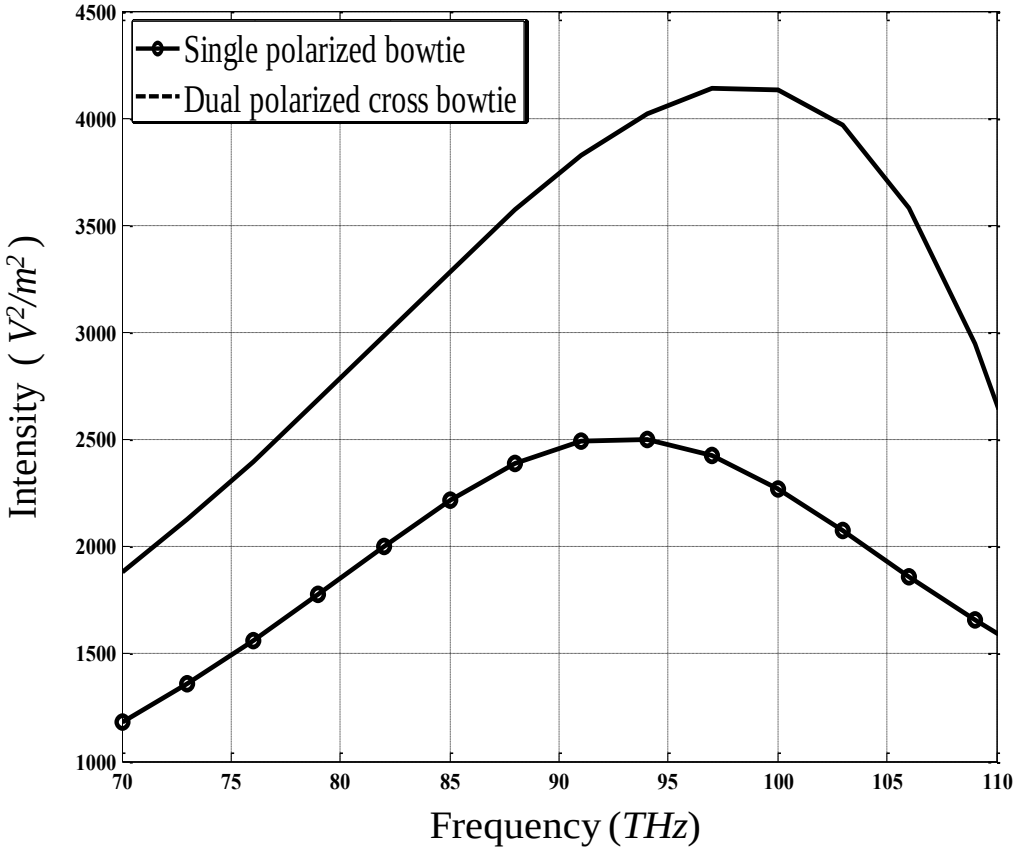

Figure 3.9: Comparison of local field intensity at the gap for single polarized bowtie and dual polarized cross bowtie nanoantenna for L = 1.0 μm, d = 1.0 μm, and G = 50 nm.

3.4. Parametric Studies of Dual Polarized Cross Bowtie Nanoantenna

The theory of the novel energy harvester depends on the utilization of the dual polarized cross bowtie nanoantenna. Therefore, we carry out a parametric study to investigate the effects of geometrical parameters, i.e. gap size, length, width, and tip-shape, on the local field enhancement at the gap of the cross bowtie nanoantenna in this section.

3.4.1 Gap-Size

Our study indicates that small gap size G with all the other parameters fixed (L, d) causes an enhancement in the local field at the gap. Fig. 3.10 shows that the local field enhancement at resonance for the dual polarized cross bowtie nanoantenna with a separation gap of 20 nm is significantly higher than the gap of 50 nm and 80 nm.

Moreover, a redshift is observed in the resonance as the gap becomes smaller. Since the local field increases with small gap-size, it is always better to design nanoantennas with small gaps in order to get strong field enhancement. However, this becomes one of the greatest challenges in the fabrication technique.

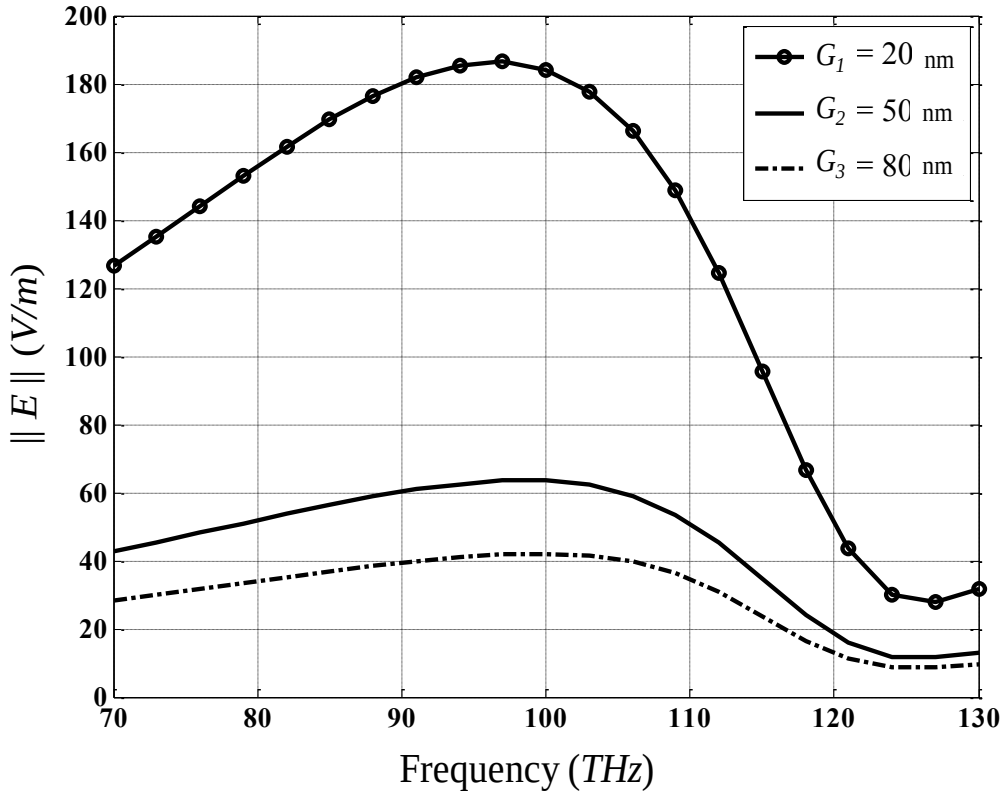

Figure 3.10: Variation in the local field enhancement with the change in the gap-size *G* of the cross bowtie nanoantenna.

3.4.2. Length

In microwave theory, the resonance wavelength changes linearly with the spatial length of the antennas. However, this is not the case for the antennas operating at THz, infrared, or visible regime. Therefore, we investigate the variation in the local field enhancement with the change in the length *L* of the cross bowtie nanoantenna.

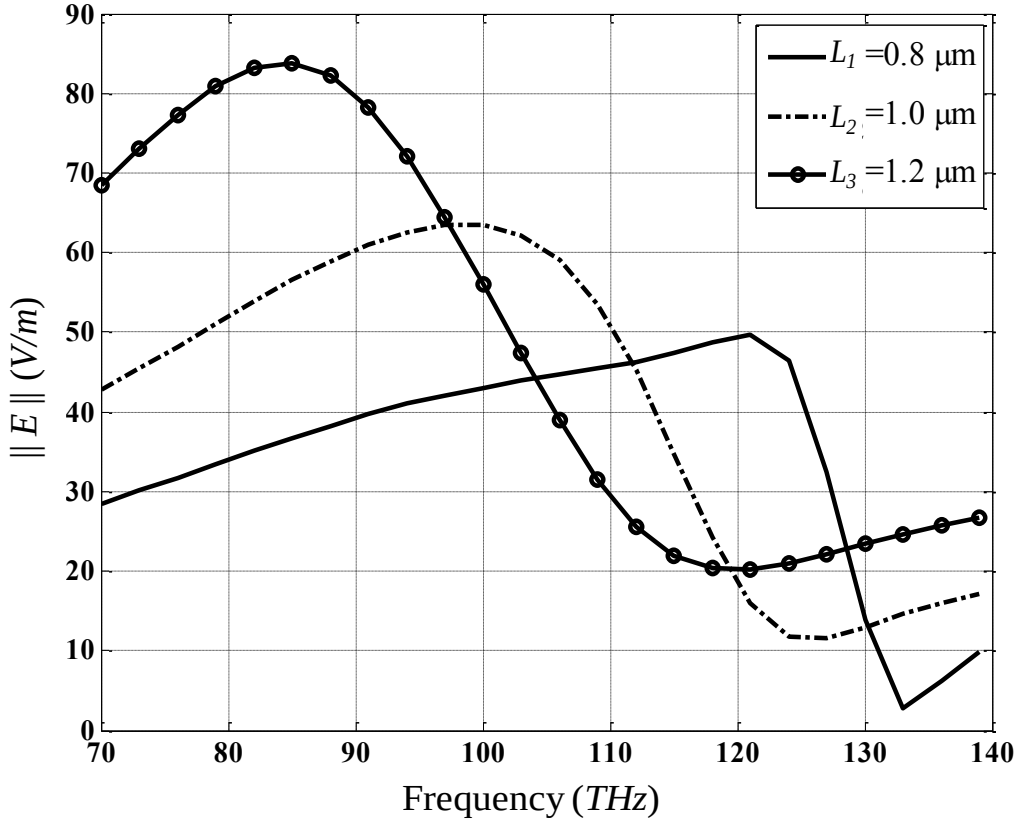

Figure 3.11: Local field enhancement at the gap of the dual polarized cross bowtie nanoantenna for different values of length *L*.

Fig. 3.11 indicates that when the length *L* increases from 0.8 μm to 1.2 μm with all other parameters (*d*, *G*) fixed, the resonance redshifts with a significant increase in the local field. This is expected because as increasing *L* with a fixed gap size *G* is effectively equivalent to a smaller gap-size. As a consequence, smaller gap-size leads to higher local field, as shown in previous subsection.

3.4.3. Width

We also investigate the variation in the local field enhancement with the change in the width *d* of the cross bowtie nanoantenna. Fig. 3.12 shows that an increase in the width *d* from 0.8 μm to 1.2 μm with the other parameters (*L*, *G*) fixed causes a decrease in the local field. The resonance slightly shifts at a shorter wavelength.

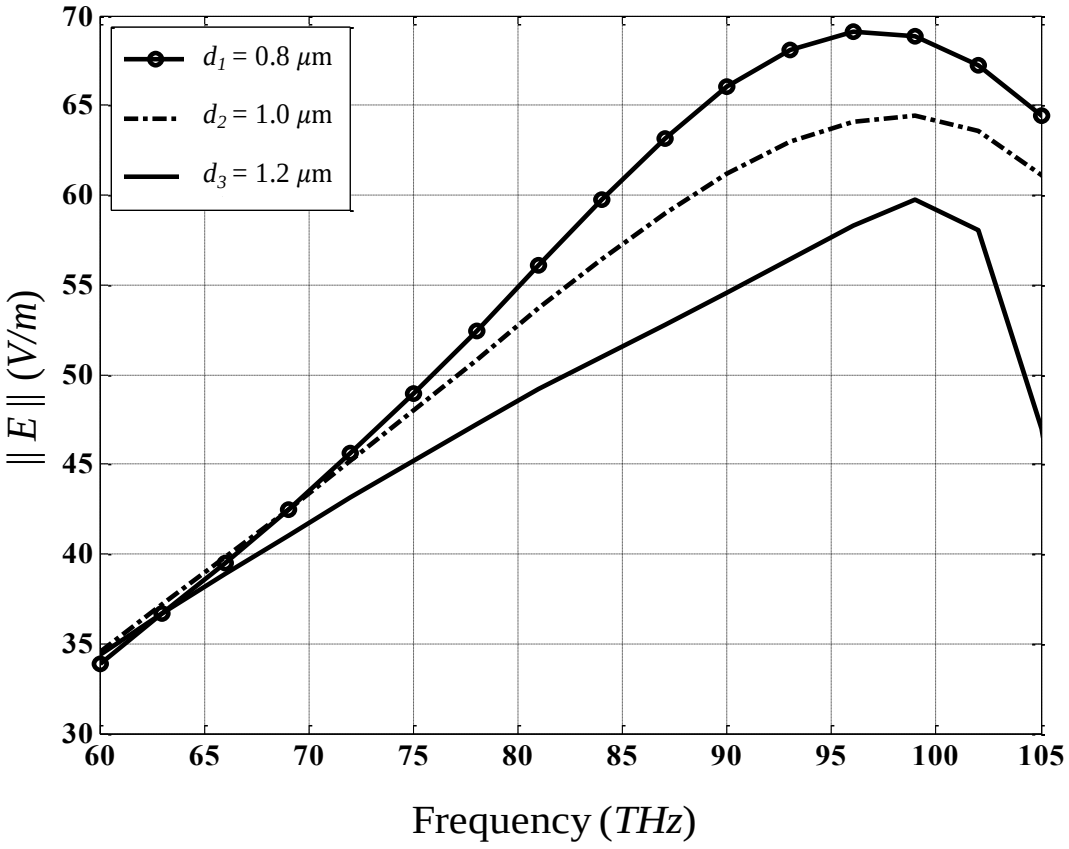

Figure 3.12: Local field enhancement at the gap of the dual polarized cross bowtie nanoantenna for different values of width *d*.

One important thing is to observe that as the length of the antenna *L* is fixed, the change in the width *d* of the antenna leads to a change in the tip-angle. Therefore, the tip angle has also an effect on the variation in local field enhancement at the gap for the cross bowtie nanoantenna. Our study indicates that the local field at the gap is more sensitive to the change of length *L* as compared to changes of the width *d* in terms of the resonance frequency and field enhancement.

3.4.4. Tip-Shape

It is very challenging to fabricate structure at nanoscale with the existing technologies. It becomes even more difficult to fabricate nanostructures with sharp tips as it requires nanometer precision. Therefore, we investigate the effect of the tip-shape on the local field enhancement at the gap of the cross bowtie nanoantenna.

Table 3.4: Design parameters for tip-shape

Geometrical Parameters	**Values**
Antenna Length, *L*	1.0 μm
Antenna Width, *d*	1.0 μm
Gap-size, *G*	100 nm
Thickness, *t*	30 nm

To carry out the investigation, we perform the simulations of the structure with sharp and curved-tips. In our simulation, the radius of curvature for curved-tips is around 70 nm and 100 nm. The other parameters i.e. length, width, and gap-size of the cross bowtie nanostructure are remained constant. The design parameters for this simulation are mentioned in Table 3.4. Fig 3.13 shows the variation in the field enhancement at the gap for the change in the shape of the tip of the cross bowtie nanoantenna. There is a significant amount of field enhancement at the gap for the sharp-tip.

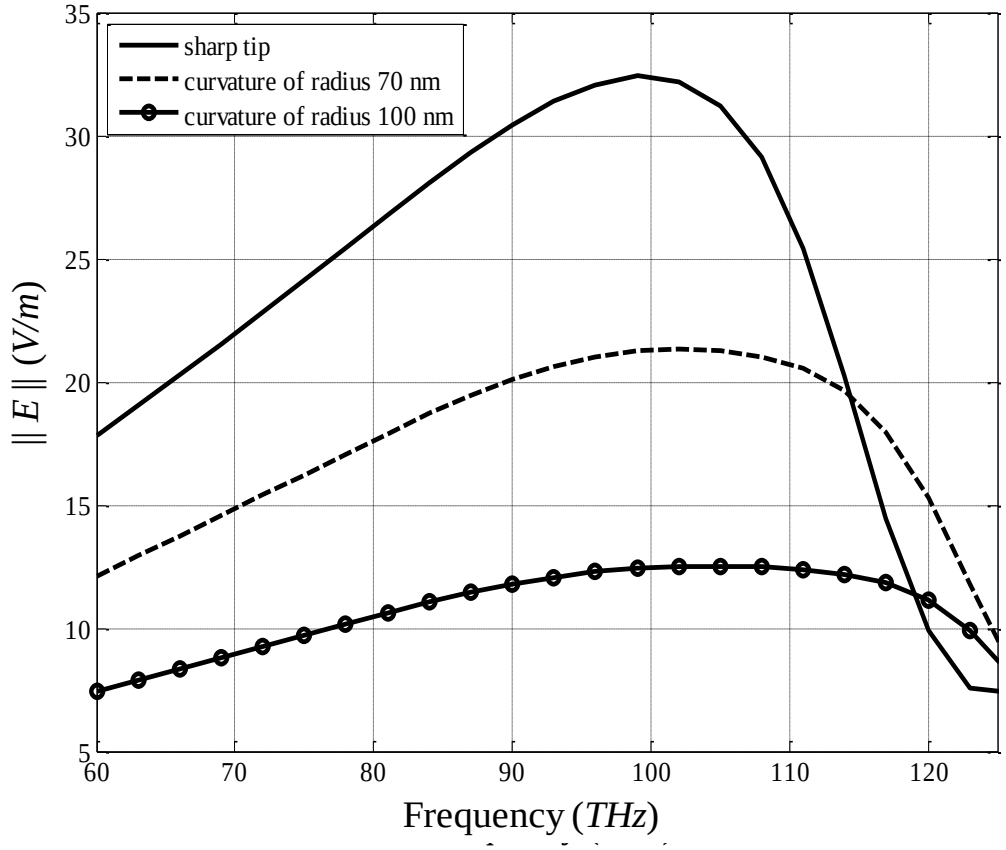

Figure 3.13: Variation in the local field enhancement with the change in the tip-shape of the cross bowtie nanoantenna.

On the other hand, the enhancement of the local field for curved-tips varies depending on the radius of the curvature of the tip. Our study indicates that the curved-tip leads to less enhancement of the local field at the gap compared to the sharp-tip.

Our parametric study shows that the cross bowtie nanoantenna is able to deal with dual polarized plane wave and produces high local field enhancement compared to the regular bowtie nanoantenna. Our investigation also shows that the resonance characteristic of the cross bowtie nanoantenna is affected by the geometrical parameters of the structure. Since rectification is a major challenge for rectennas operating at high frequency regime, we propose a novel design of an energy harvester which is able to generate DC energy from high-frequency electromagnetic radiation without a diode.

CHAPTER 4

4. The Novel Approach

In this chapter, we propose a novel energy harvester which converts solar electromagnetic radiation at high frequency into DC energy without using MIM diodes. The proposed device consists of a dual polarized nantenna loaded with an anisotropic material of nonlinear electrical conductivity at its gap. The dual polarized nantenna focuses the randomly polarized radiation into its gap resulting in high electric field. The anisotropic material at the gap converts the dual polarizations at the gap into a DC voltage difference across the terminals of the nanoantenna. By utilizing an array of such a device, significant DC voltage can be generated using ambient electromagnetic radiation. The novelty of the proposed design is in the rectification of the electromagnetic radiation without utilizing a MIM diode.

4.1. Novel Energy Harvester

Our proposed theoretical design for novel energy harvester consists of a dual polarized cross bowtie nanoantenna loaded with an anisotropic material with nonlinear electrical conductivity at its gap, as shown in Fig. 4.1.

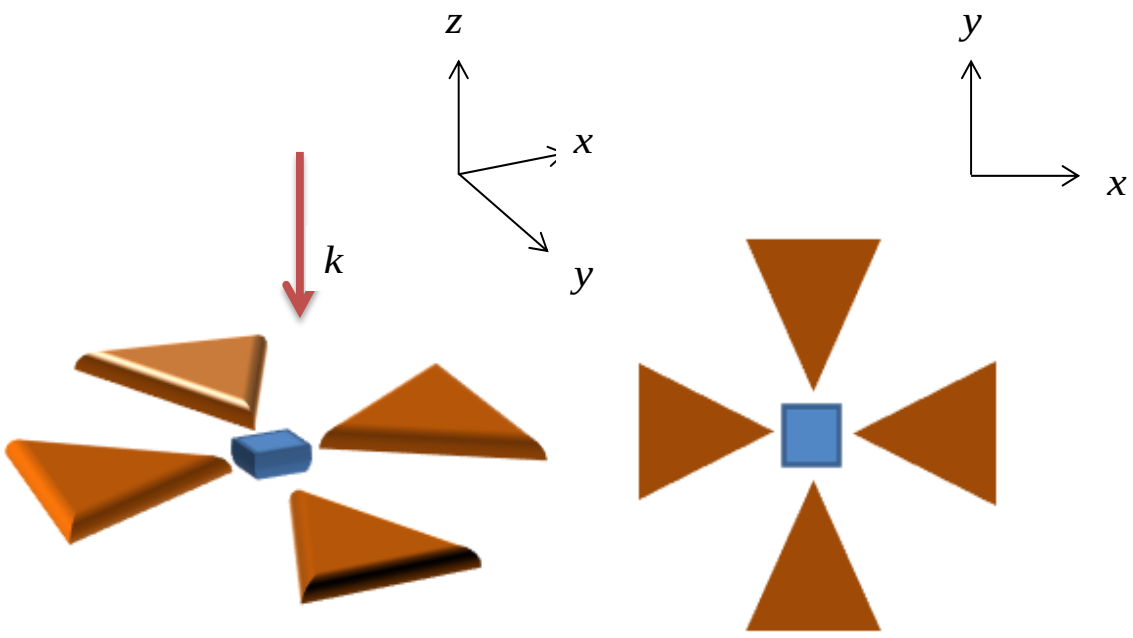

Figure 4.1: Dual polarized cross bowtie nanoantenna loaded with an anisotropic material in its gap.

When a randomly polarized incoming plane wave illuminates perpendicularly on the energy harvester, the cross bowtie nanoantenna focuses the high frequency radiation into its gap resulting in a high local electric field. The local electric field at the gap interacts with the anisotropic material. One of the orthogonal polarizations produces a high frequency electrical current which flows through the anisotropic material. Simultaneously, the other polarization modulates the conductivity of the anisotropic material nonlinearly in such a way that the anisotropic material converts the dual polarizations at the gap into DC voltage difference across the terminal of the nanoantenna.

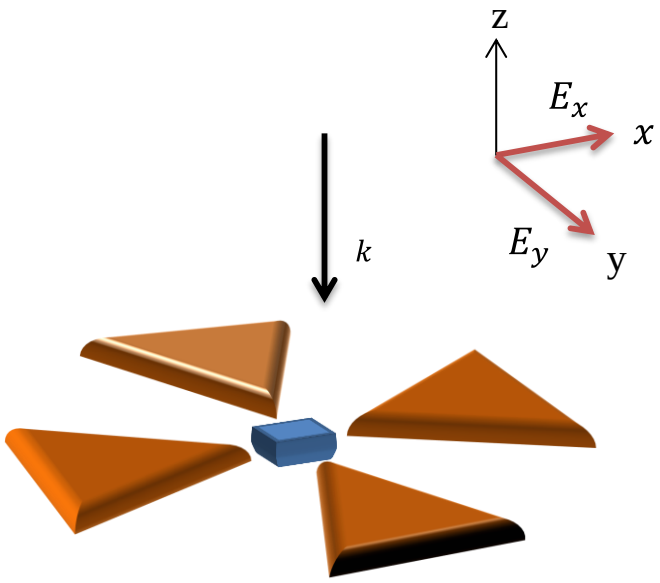

Figure 4.2: Orthogonally polarized (E_x,E_y) light wave illuminates perpendicularly (along z-axis) on the surface of the cross bowtie nanoantenna.

In our theoretical model, an incoming plane wave of orthogonal polarization, i.e. E_x and E_y, illuminates perpendicularly (along z-axis) on the surface of the cross bowtie nanoantenna, as shown in Fig. 4.2. The cross bowtie nanoantenna is able to focus randomly polarized radiation. Therefore, there is local field enhancement at the gap regardless of the polarization of the incoming light wave. The local field E_x and E_y enhance at the gap of the cross bowtie nanoantenna and interacts with the anisotropic material. One of the dual-polarization i.e. E_x produces high-frequency current which flows through the anisotropic material along x direction. The other polarization E_y modulates the conductivity of the anisotropic material. The anisotropic material converts the dual polarization at the gap into DC voltage difference across the terminal of

nanoantenna. The proof of concept is presented through the simulation of the energy harvester in infrared regime.

4.2 Conductivity Tensor of Anisotropic Material

In our theoretical model, the material loaded in the gap is assumed to be anisotropic and dispersive in nature. Since the material is anisotropic in nature, the strength of the electrical conductivity of the material is different in different directions. In our model, the anisotropic conductivity $\hat{\boldsymbol{\sigma}}$ of the loaded material is a tensor quantity and is given by –

$$\hat{\boldsymbol{\sigma}} = \begin{bmatrix} \sigma_{xx} & \sigma_{xy} & \sigma_{xz} \\ \sigma_{yx} & \sigma_{yy} & \sigma_{yz} \\ \sigma_{zx} & \sigma_{zy} & \sigma_{zz} \end{bmatrix}, \qquad (4.1)$$

where the elements $\sigma_{xx}, \sigma_{xy}, \sigma_{xz}, \sigma_{yx}, \sigma_{yy}, \sigma_{yz}, \sigma_{zx}, \sigma_{zy,}$,and σ_{zz} are components of anisotropic electrical conductivity. The non-diagonal components are referred as coupling conductivities. In our theoretical model, the coupling conductivities are defined by –

$$\sigma_{xy} = \sigma_{xz} = \sigma_{yz} = \sigma_{zx} = \sigma_{zy} = 0, \qquad (4.2)$$

The diagonal elements of the anisotropic conductivity are defined by –

$$\sigma_{xx} = \sigma_{yy} = \sigma_{zz} \neq 0, \qquad (4.3)$$

In our model, the component σ_{xx} changes nonlinearly as a function of y-polarized electric field E_y. Therefore, the expression of σ_{xx} for the anisotropic material is given by –

$$\sigma_{xx} = \sigma_{xxo} + \alpha\, \sigma_{xxo}\, E_{y,} \qquad (4.4)$$

where σ_{xxo} is the DC conductivity and α is defined as the nonlinear conductivity coefficient of the loaded anisotropic material. The conductivity along x direction σ_{xx} of the anisotropic material changes with orthogonally polarized wave E_y. The other diagonal elements i.e. σ_{yy} and σ_{zz} have been parameterized with some constant values in our model.

By substituting the values, we can rewrite equation (4.1) for our proposed model as follows:

$$\hat{\boldsymbol{\sigma}} = \begin{bmatrix} \sigma_{xxo} + \alpha\, \sigma_{xxo}\, E_y & 0 & 0 \\ 0 & \sigma_{xxo} & 0 \\ 0 & 0 & \sigma_{xxo} \end{bmatrix}. \qquad (4.5)$$

4.3 Proof of Concept

In this section, we present the proof of concept of our proposed model for novel energy harvester. Since the material loaded in the gap is anisotropic and possesses nonlinear electrical conductivity, Maxwell's equations allow very interesting physical phenomena once the EM wave interacts with the anisotropic material.

In principle, for the loaded material in the gap the relation between current density and localized electric field is given by:

$$\boldsymbol{J} = \hat{\boldsymbol{\sigma}}\boldsymbol{E}, \qquad (4.6)$$

where $\boldsymbol{J}$ is the current density, $\hat{\boldsymbol{\sigma}}$ is the anisotropic electrical conductivity distribution of the loaded material, and $\boldsymbol{E}$ is the localized electric field. In our model, the cross bowtie nanoantenna is exposed to an incoming plane wave of orthogonal polarization. Therefore, essentially, $E_z = 0$.

Thus, we can rewrite equation (4.6) as follows:

$$\begin{bmatrix} j_x \\ j_y \\ j_z \end{bmatrix} = \begin{bmatrix} \sigma_{xxo} + \alpha\, \sigma_{xxo}\, E_y & 0 & 0 \\ 0 & \sigma_{xxo} & 0 \\ 0 & 0 & \sigma_{xxo} \end{bmatrix} \begin{bmatrix} E_x \\ E_y \\ 0 \end{bmatrix}, \qquad (4.7)$$

where j_x, j_y, and j_z are current densities in x, y, and z direction respectively.

We can simplify equation (4.8) as follows:

$$\begin{bmatrix} j_x \\ j_y \\ j_z \end{bmatrix} = \begin{bmatrix} \sigma_{xxo}E_x + \alpha\, \sigma_{xxo}E_yE_x \\ \sigma_{xxo}E_y \\ 0 \end{bmatrix}. \qquad (4.8)$$

The above equation (4.8) shows that the current density along x direction j_x is comprised of two components; where the second component of j_x ensures the possibility of the existence of a non-zero average DC component.

The DC conductivity σ_{xxo} and electric field intensity $\boldsymbol{E}$ vary for a wide range of materials e.g. insulator, semiconductor, and metal. The enhancement of the electric field $\boldsymbol{E}$ at the gap of the nanoantenna depends on the properties of the loaded material. Different values of DC conductivity of the loaded material leads to different properties e.g. metal, semiconductor, and insulator. In order to make the second component of j_x more pronounced, proper selection of the DC conductivity of the loaded anisotropic

material is required. Therefore, we perform parametric studies on α and σ_{xxo} in our simulation model to investigate the nonlinear effect of the anisotropic material once randomly polarized radiation interacts with the novel energy harvester.

4.4 Simulation Setup in COMSOL Multiphysics

We validate the design of our novel energy harvester through the simulations by using standard commercial software COMSOL Multiphysics. It allows efficient estimation of the optical response for geometries at nanoscale. We perform time-domain analysis for the proposed energy harvester in RF module.

4.4.1. Time Domain Modeling in COMSOL

We perform transient analysis on our proposed energy harvester to investigate the nonlinear effects of the anisotropic material once the polarized light wave interacts with the nanoantenna. The cross bowtie nanoantenna is assumed to be located in free space. The cross bowtie nanoantenna is excited through a normally incident plane wave (along z- axis) of 30 THz with an electric field intensity of 1 V/m. Once the light illuminates on the surface of the energy harvester, the radiation gets focused by the nanoantenna resulting in strong electric field at the gap. The local electric field generated at the gap is alternating, i.e. varies with time, in nature. Since the conductivity of the anisotropic material changes nonlinearly with the orthogonally polarized wave E_y, the conductivity of the anisotropic material changes with time and is different at different time steps. To

put this in a simple way, the conductivity of the material is different in different directions (i.e. anisotropic) and also different at different time steps (i.e. modulation of the orthogonally polarized wave E_y). In order to investigate the nonlinear effects of the anisotropic material on the dual polarization at the gap, time-domain analysis is performed.

4.4.2. Geometries and Dimensions

COMSOL offers internal CAD software which is in 1D, 2D, and 3D. 1D and 2D models are simple and require less time to compute. However, 3D models require more boundary conditions which increase complexity and make computationally expensive. We design the 3D model of our proposed nanostructure. Our design consists of two pairs of bowtie nanoantennas and an anisotropic material in the gap. All the design parameters for our proposed model are mentioned in Fig. 4.3 and Table 4.1. The geometrical parameters of the energy harvester are optimized for 30 THz. The electric field enhancement at the gap depends on the dimension and the spatial orientation of the anisotropic material. The electromagnetic response of the symmetrically designed energy harvester is asymmetrical in nature due to the nonlinearity of the anisotropic material.

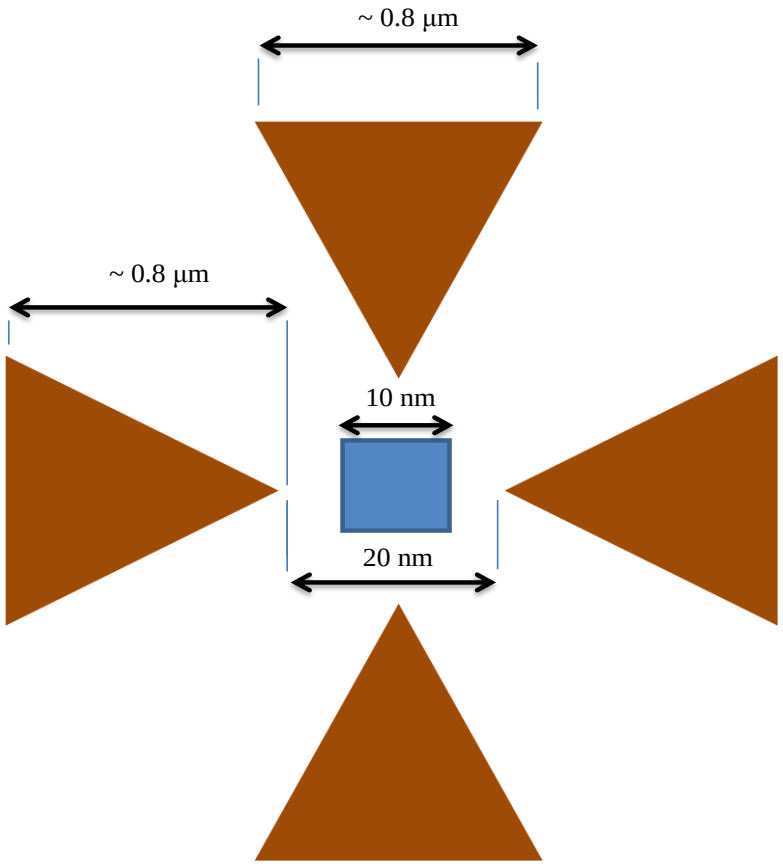

Figure 4.3: Our proposed novel energy harvester with design parameters (top view).

Table 4.1: Design parameters of the proposed model

Parameters	Values
Antenna length	~ 1.6 µm
Antenna width	~ 0.8 µm
Material length & width	10 nm
Antenna & Material thickness	20 nm
Gap	20 nm

4.4.3. Boundary Conditions

The boundary conditions for the 3D structure increase complexity in COMSOL. One of the major challenges in finite element modeling (FEM) is to treat the open boundaries as radiation problems. Perfectly matched layer (PML) can be added as a boundary condition which absorbs the incident radiation without producing any reflections. Since PML is not supported in the time-domain analysis in COMSOL, we use scattering boundary condition (SBC) in the time-domain simulation. This boundary condition makes the boundary transparent for the scattered wave. It also becomes transparent for incoming plane waves with any angle of incidence. SBC is applied on the top and bottom boundaries of the unit cell, as shown in Fig 4.4.

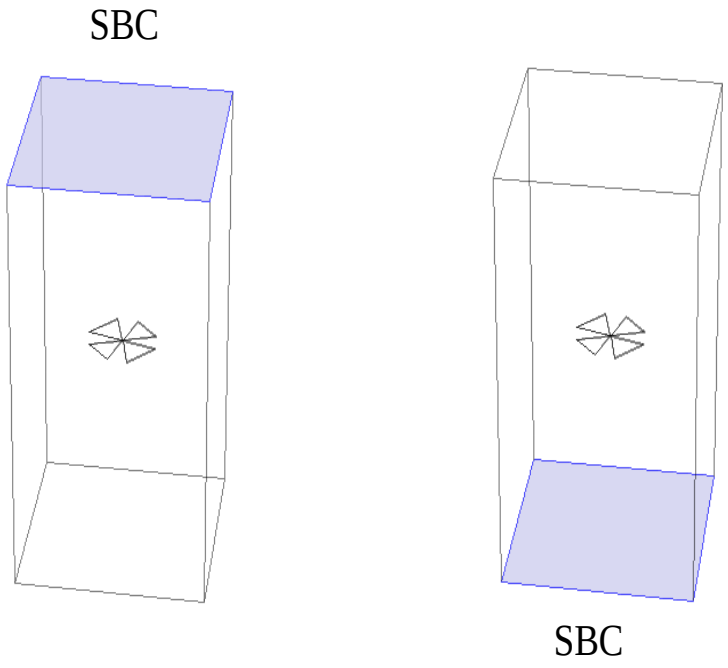

Figure 4.4: Scattering boundary condition (SBC) for the time-domain modeling.

Perfect Electric Conductor (PEC) and Perfect Magnetic Conductor (PMC) are also used as boundary conditions in our model. Since the plane wave is propagating in the symmetric periodic array of nanostructure, the proper conditions for the boundaries on the sides of the unit cell are PEC and PMC.

In essence, the tangential component of the electric field is zero for PEC wall and tangential component of the magnetic field is zero for PMC wall. For our 3D simulation, the setup of PMC and PEC as boundary conditions entirely depends on the polarization of the incoming EM wave. Fig. 4.5 shows the realization of both PMC and PEC for the single-polarized plane wave in 3D simulation.

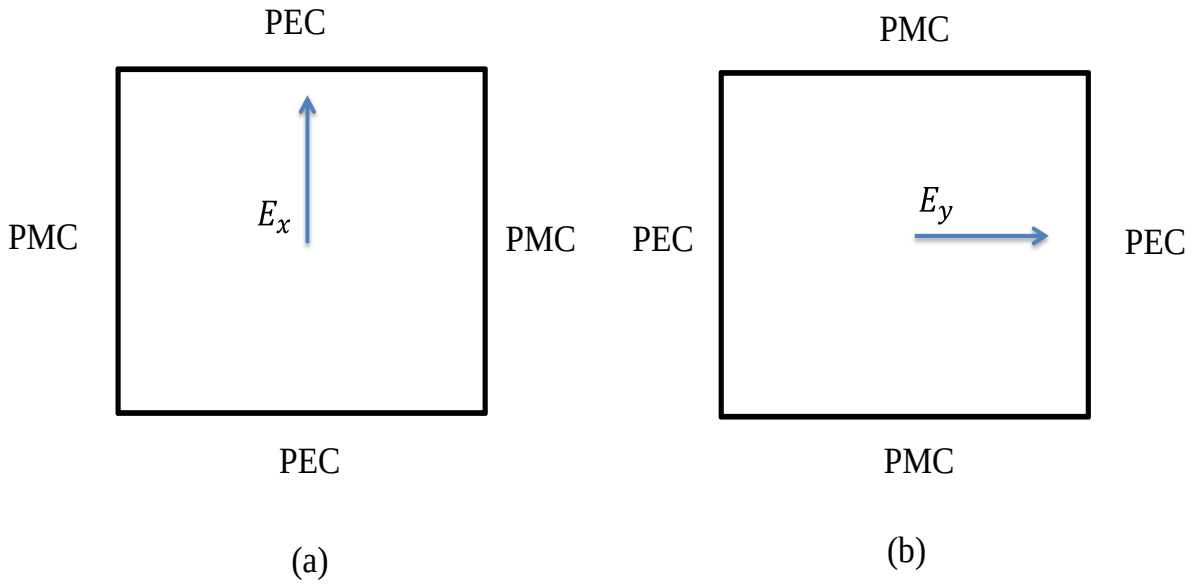

Figure 4.5: PEC and PMC setup for 3D simulation, if EM wave is only (a) *x*-polarized (b) *y*-polarized.

Since the electromagnetic radiation is dual polarized (E_x, E_y) in our model, the incoming light wave is diagonally polarized relative to the energy harvester. The PEC and PMC setup for our proposed 3D model is shown in Fig.4.6 and Fig. 4.7.

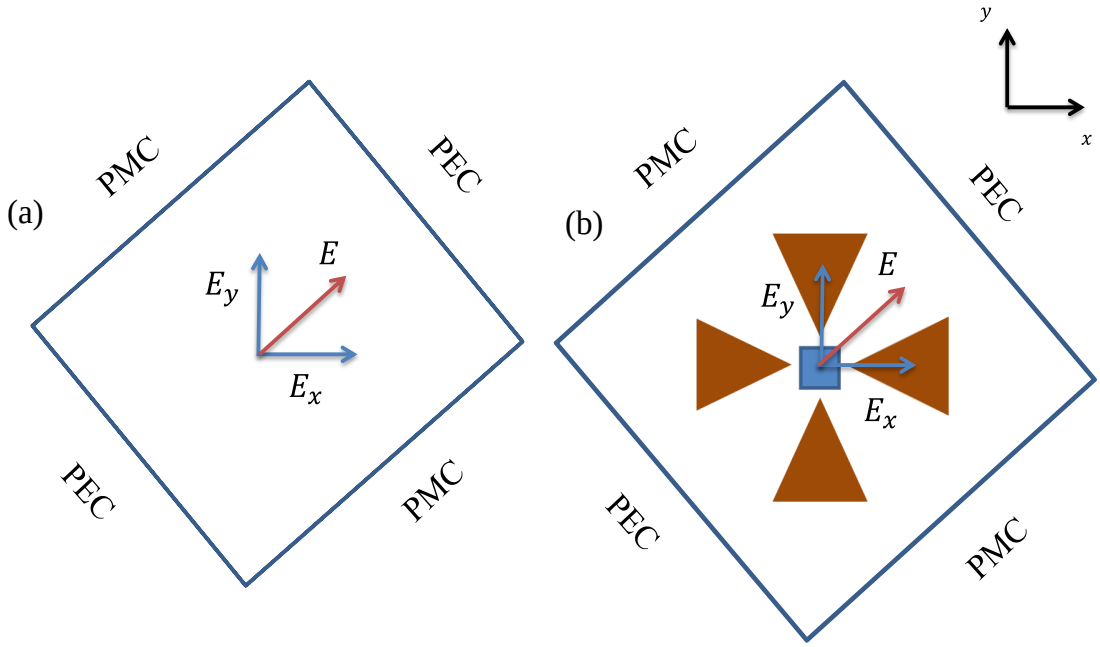

Figure 4.6: Realization of PEC and PMC setup for (a) dual polarized plane wave (b) proposed design.

4.4.4. Defining Materials

Since the noble metals are considered to be the best plasmonic materials [74], all the nanoantennas in our simulation model are composed of gold. The Drude model is used to estimate the complex permittivity of the gold since metals such as gold exhibits dispersive properties at infrared regime. Moreover, the conductivity of the anisotropic material used in the gap is a tensor quantity. The tensor is defined properly from the

material section of COMSOL. The coupling components in the tensor matrix are set to zero, whereas the diagonal components have been parameterized.

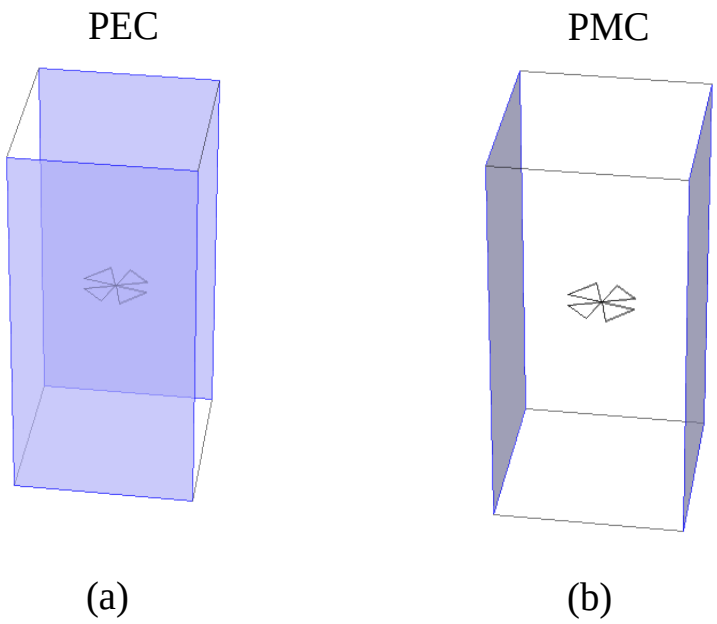

Figure 4.7: (a) PEC and (b) PMC setup in 3D simulation.

4.4.5. Mesh

In our transient simulation, there are six domains, where four domains are for the cross bowtie nanoantenna, one for the anisotropic material at the gap, and the other one is for the whole unit cell i.e. air surrounding the nanoantenna. Since the dimension of the nanoantenna and anisotropic material is significantly small compared to the unit cell, the mesh for the energy harvester needs to be much denser compared to the unit cell. There are different kinds of mesh e.g. coarser, normal, fine, finer, and extra fine available in

COMSOL which can be employed for different geometrics. It is always better to choose the mesh wisely so that it accurately represents solution of the geometry without having too many elements.

Conventionally, it requires at least ten elements per wavelength to obtain a result which is not too far away from the real solution. In our simulation, for the energy harvesting device and unit cell, we have used around 15 elements per wavelength, i.e. element size is around 0.7 μm. We have used even finer mesh, i.e. element size is around 0.005 μm, for the material at the gap.

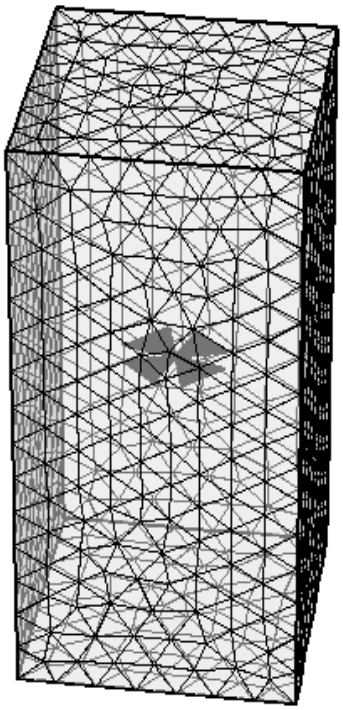

Figure 4.8: 3D Mesh of our proposed model in time-domain simulation.

4.5. Parameterization of Anisotropic Material & Simulation Results

We validate our model as a proof of concept by changing the governing parameters i.e. DC conductivity σ_{xxo} and the nonlinear conductivity coefficient α of the loaded material and obtained promising results.

We perform time-domain simulations using RF module in COMSOL Multiphysics software on Intel CPU at 3.6 GHz (96.0 GB of RAM and 64-bit operating system). The values of DC conductivity σ_{xxo} and nonlinear conductivity coefficient α for time harmonic simulations of the orthogonally polarized waves are presented in Table 4.2.

Table 4.2: Values of σ_{xxo} and α

DC conductivity, σ_{xxo}	**Nonlinear Conductivity Coefficient, α**
$\mathbf{2.5 \times 10^{-3}}$	0.04, 0.40
$\mathbf{2.5 \times 10^{1}}$	0.04
$\mathbf{2.5 \times 10^{2}}$	0.04
$\mathbf{2.5 \times 10^{3}}$	0.01, 0.02, 0.03, 0.04, 0.05
$\mathbf{2.5 \times 10^{4}}$	0.01, 0.04

We parameterize both the DC conductivity and the nonlinear conductivity coefficient to observe the effects of the nonlinear electrical conductivity of the anisotropic material once the high-intensity field is generated at the gap. In the following subsections the interesting results of the time-harmonic simulations of the orthogonally polarized waves

(x and y polarization) in the gap for a broad range of DC conductivity σ_{xxo} and different values of the nonlinear conductivity coefficient α (given in Table 4.2) are presented.

❖ $\sigma_{xxo} = 2.5 \times 10^{-3}$ S/m and $\alpha = 0.04$ m/V

In our simulation for the anisotropic material, at first we set a low value for DC conductivity i.e. $\sigma_{xxo} = 2.5 \times 10^{-3}$ S/m and simulated the device for $\alpha = 0.04$ m/V. No DC component in the orthogonally polarized waves is observed for a low value of DC conductivity, as shown in Fig. 4.9. Fig. 4.10 shows the normalized electric field at the gaps of the cross bowtie nanoantenna. It also indicates zero DC shift in the polarized waves.

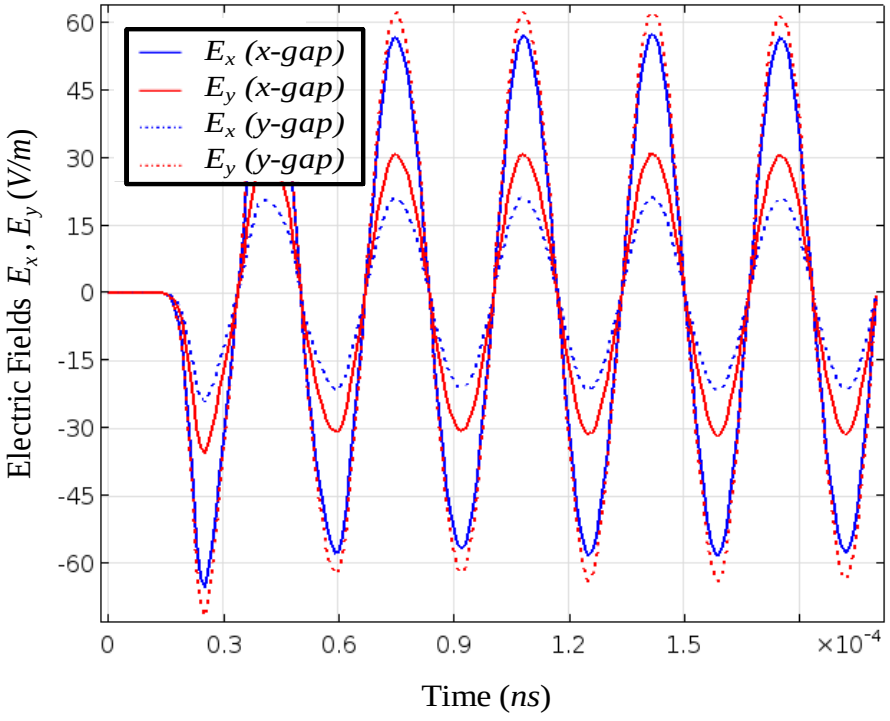

Figure 4.9: Electric field (E_x, E_y) at the gap for σ_{xxo}= 2.5 $\times 10^{-3}$ S/m , α = 0.04 m/V.

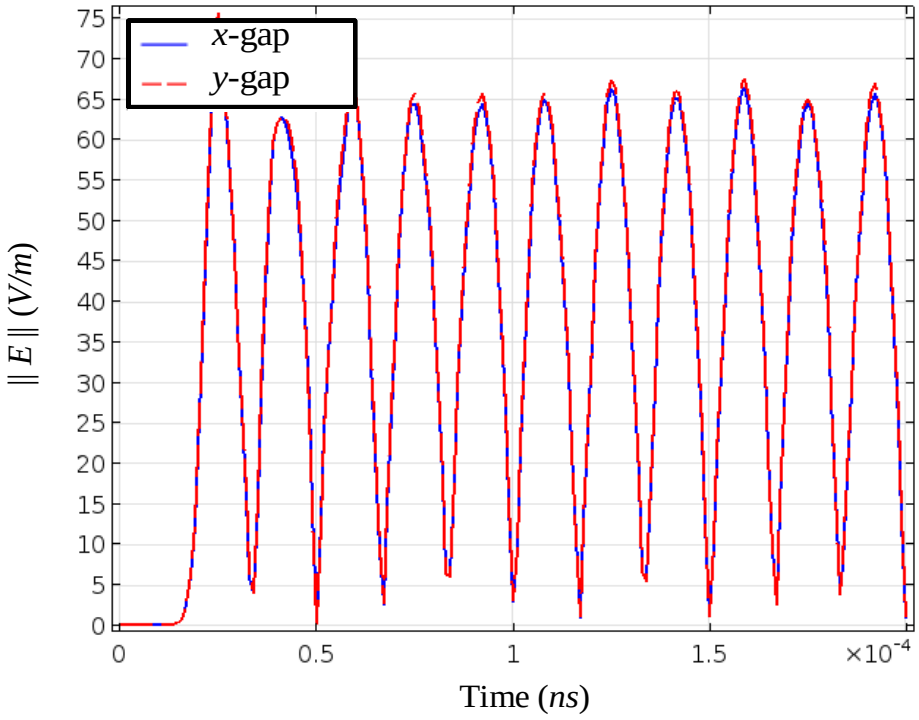

Figure 4.10: Normalized field at the gap for σ_{xxo} = 2.5 $\times 10^{-3}$ *S/m* and α = 0.04 m/V.

❖ $\boldsymbol{\sigma_{xxo} = 2.5 \times 10^{-3}}$ **S/m and** $\boldsymbol{\alpha = 0.40}$ **m/V**

We set a higher value for α = 0.40 m/V where the dc conductivity remains the same. No DC component in the orthogonally polarized waves is observed in this case also, as shown in Fig. 4.11. The normalized electric field at the gaps, shown in Fig. 4.12, indicates no DC component in the polarized waves.

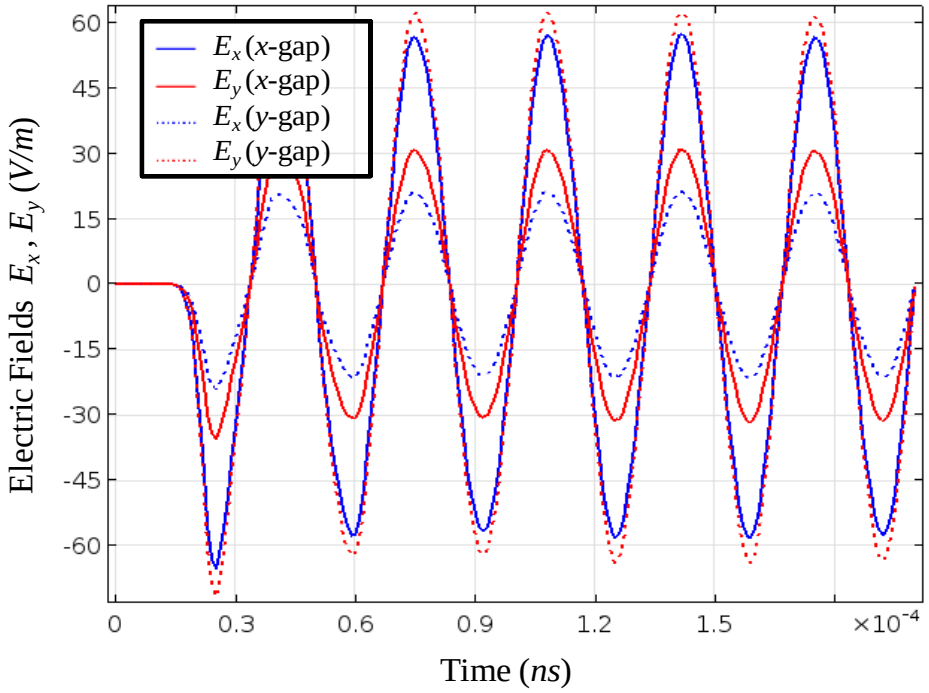

Figure 4.11: Electric field (E_x, E_y) at the gap for σ_{xxo} = 2.5 $\times 10^{-3}$ S/m, α = 0.40 m/V.

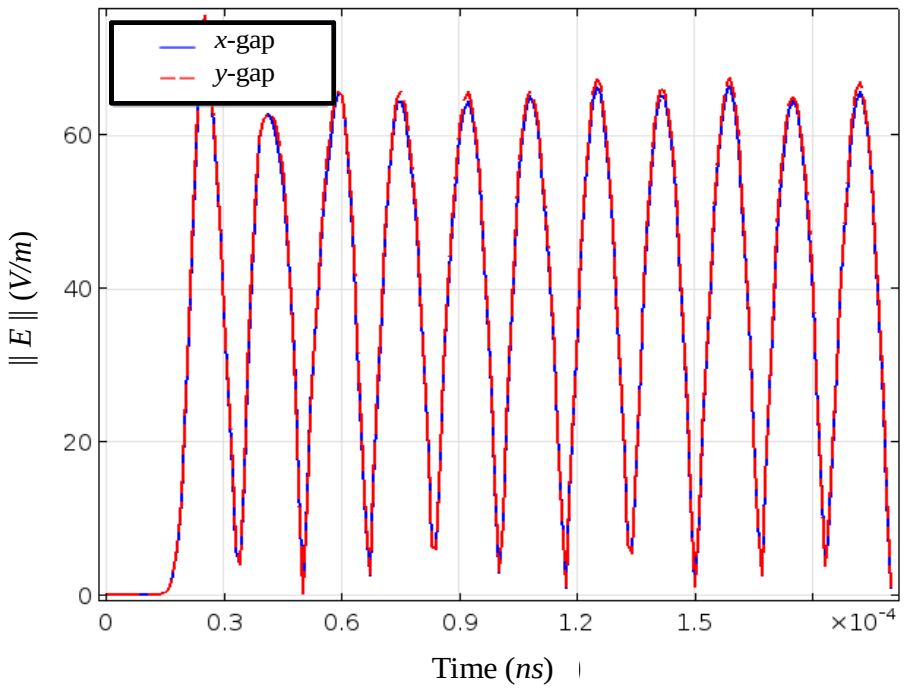

Figure 4.12: Normalized field at the gap for σ_{xxo} = 2.5 $\times 10^{-3}$ S/m, α = 0.40 m/V.

❖ $\boldsymbol{\sigma_{xxo} = 2.5 \times 10}$ **S/m and** $\boldsymbol{\alpha = 0.04}$ **m/V**

We set the value of the conductivity to $\sigma_{xxo} = 2.5 \times 10$ S/m and $\alpha = 0.04$ m/V. There is almost no significant DC component in the orthogonally polarized waves, as shown in Fig. 4.13. The normalized electric field distribution at the gaps, shown in Fig. 4.14, indicates no DC component in the polarized waves.

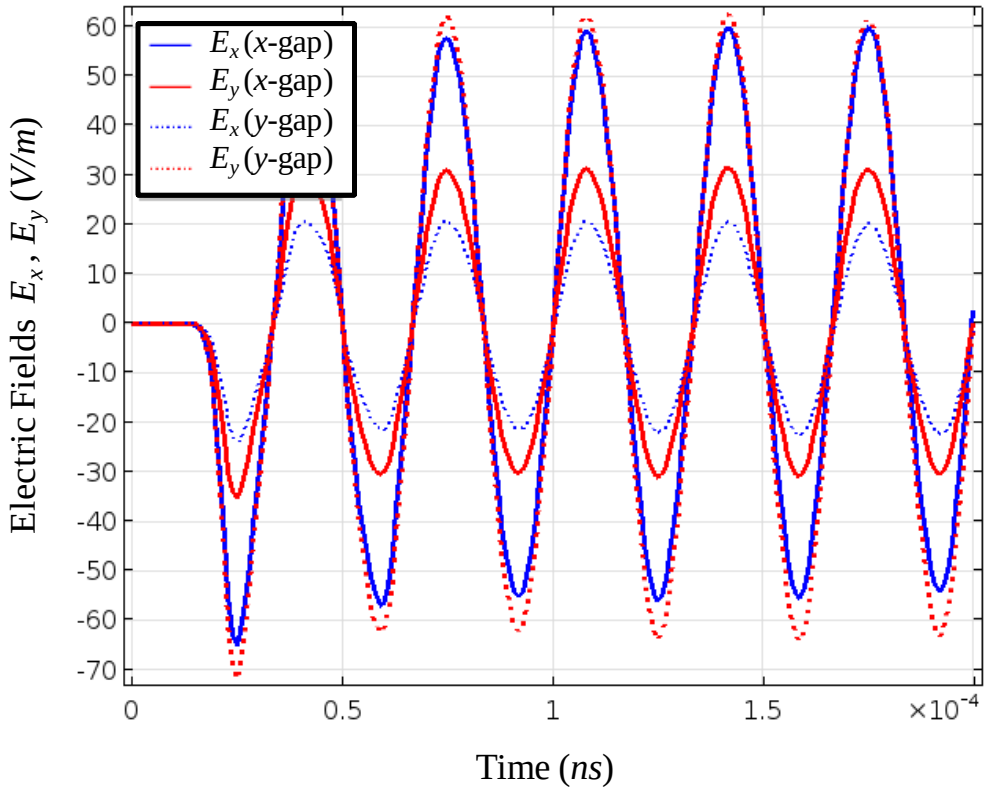

Figure 4.13: Electric field (E_x, E_y) at the gap for σ_{xxo} = 2.5 × 10 S/m and α = 0.04 m/V.

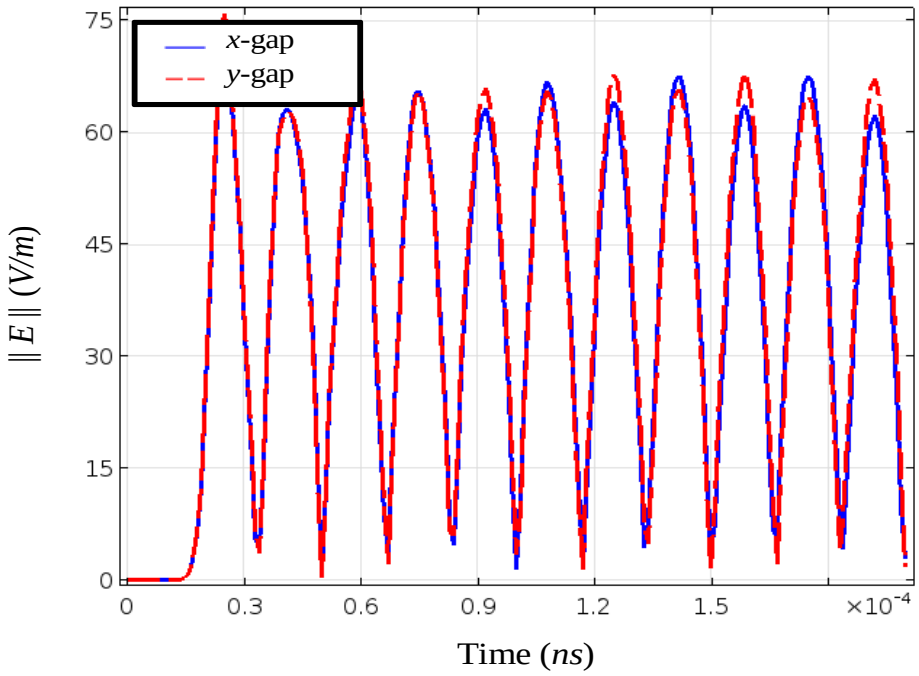

Figure 4.14: Normalized field at the gap for σ_{xxo} = 2.5 × 10 S/m and α = 0.04 m/V.

❖ $\sigma_{xxo} = 2.5 \times 10^2$ S/m and $\alpha = 0.04$ m/V

Since no change is observed in the previous cases, we set the value of DC conductivity to $\sigma_{xxo} = 2.5 \times 10^2$ and $\alpha = 0.04$ m/V. A small DC shift is observed in the x-polarized wave, as shown in Fig. 4.15. The x-polarized electric field E_x at x-gap shifts slightly upward. The positive peak of E_x is around 60 V/m, whereas the negative peak is around 45 V/m. The average of the polarized wave over a certain time gives a non-zero value. The normalized electric field distribution at the gaps, shown in Fig. 4.16, also indicates the presence of the DC component since the electric field at the gap along x direction is not uniform with time.

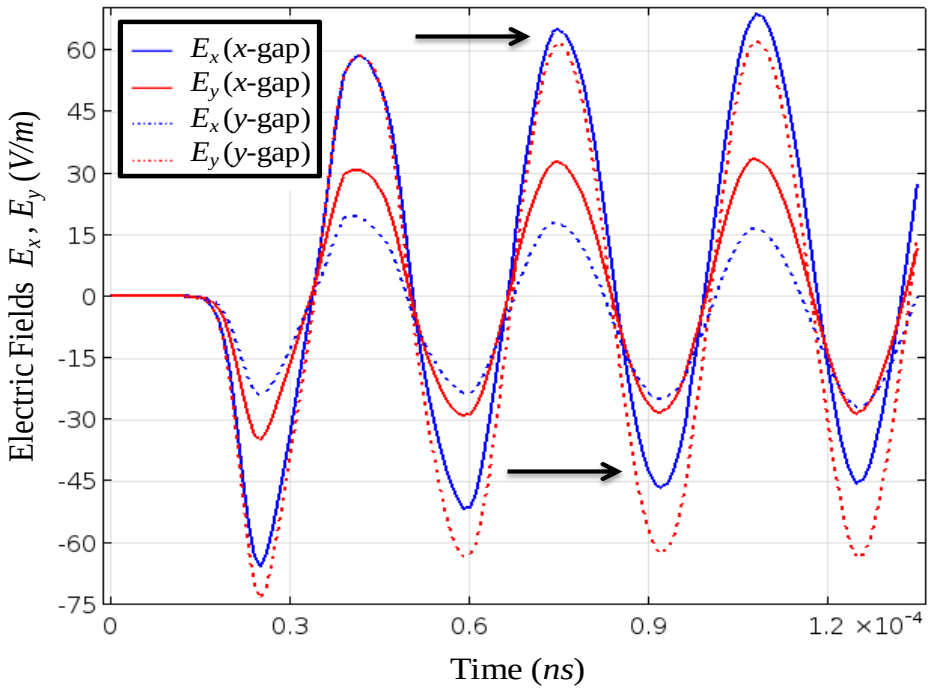

Figure 4.15: Electric field (E_x, E_y) at the gap for σ_{xxo} = 2.5 × 10^2 S/m, α = 0.04 m/V.

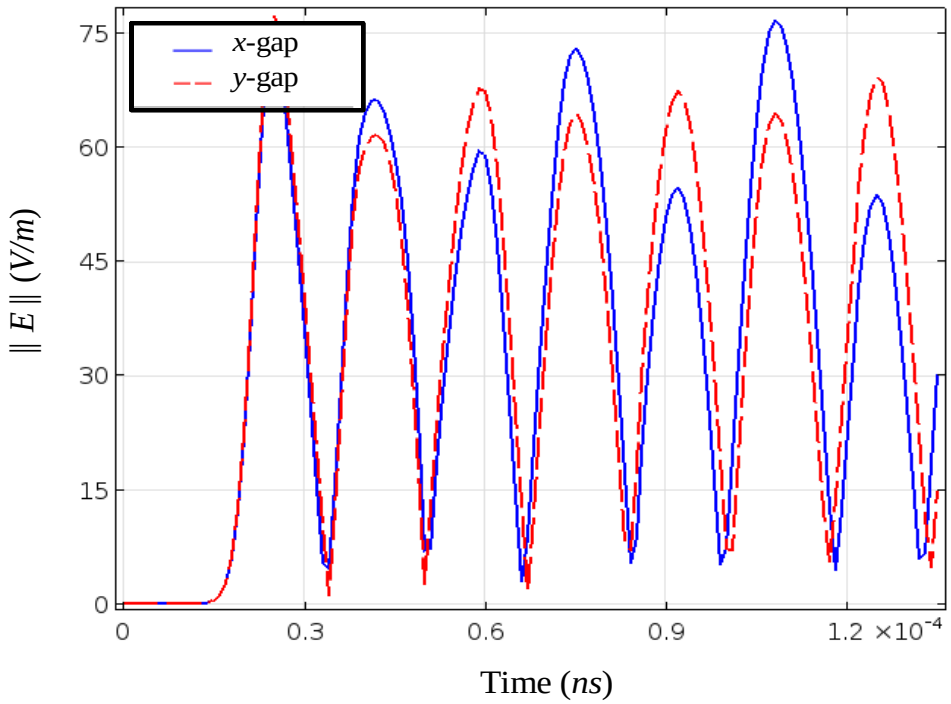

Figure 4.16: Normalized field at the gap for σ_{xxo} = 2.5 × 10^2 S/m, α = 0.04 m/V.

We estimate the generated voltage across the terminal of the nanoantenna. The generated voltage V_{gen} can be defined as a line integral of the electric field component $E_x$along x-direction at the gap. The small DC shift in the polarized electric field generates a voltage $V_{gen} = 40\ nV$.

❖ $\boldsymbol{\sigma_{xxo} = 2.5 \times 10^3}$ **S/m and** $\boldsymbol{\alpha = 0.01}$ **m/V**

We set the DC conductivity to $\sigma_{xxo} = 2.5 \times 10^3$ S/m and $\alpha = 0.01$. Fig. 4.17 shows the presence of a small DC shift in the x-polarized wave. The normalized electric field at the gaps, shown in Fig. 4.18, also indicates the presence of the DC component since the electric field at the gap along x direction is not uniform with time. From the small DC shift in the polarized electric field, the generated voltage is estimated i.e. $V_{gen} = 17.4\ nV$.

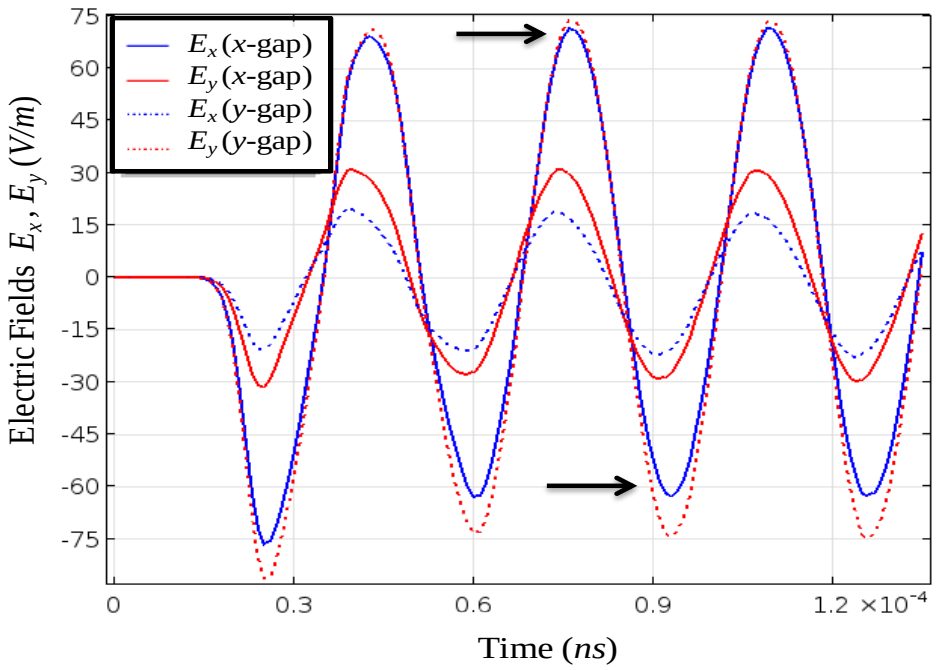

Figure 4.17: Electric field (E_x, E_y) at the gap for σ_{xxo} = 2.5 $\times 10^3$ S/m, α = 0.01 m/V.

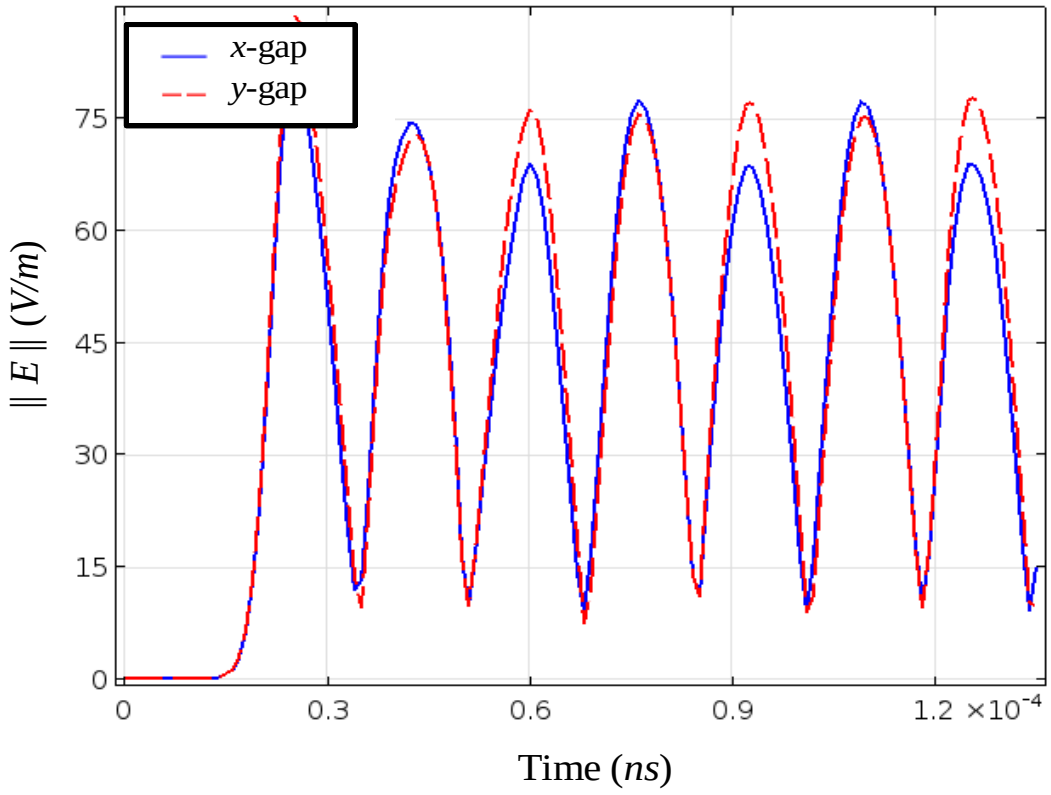

Figure 4.18: Normalized field at the gap for σ_{xxo} = 2.5 × 10^3 S/m, α = 0.01 m/V.

❖ $\boldsymbol{\sigma_{xxo} = 2.5 \times 10^3}$ **S/m and** $\boldsymbol{\alpha = 0.02}$ **m/V**

For the same value of conductivity, we set the value of α = 0.02 m/V. The presence of DC voltage is observed in the x-polarized wave, as shown in Fig. 4.19. The normalized electric field at the gaps, shown in Fig. 4.20, also indicates the presence of the DC component since the electric field at the gap along x direction is not uniform with time. The generated voltage is estimated i.e. $V_{gen} = 35\ nV$ across the terminal of the nanoantenna.

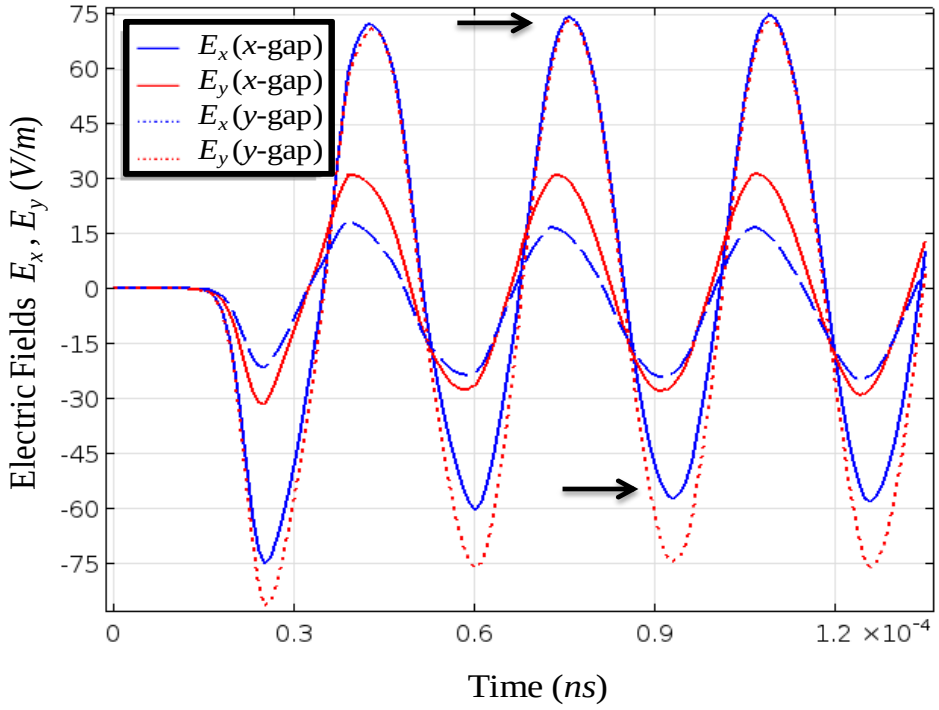

Figure 4.19: Electric field (E_x, E_y) at the gap for σ_{xxo} = 2.5 × 10^3 S/m, α = 0.02 m/V.

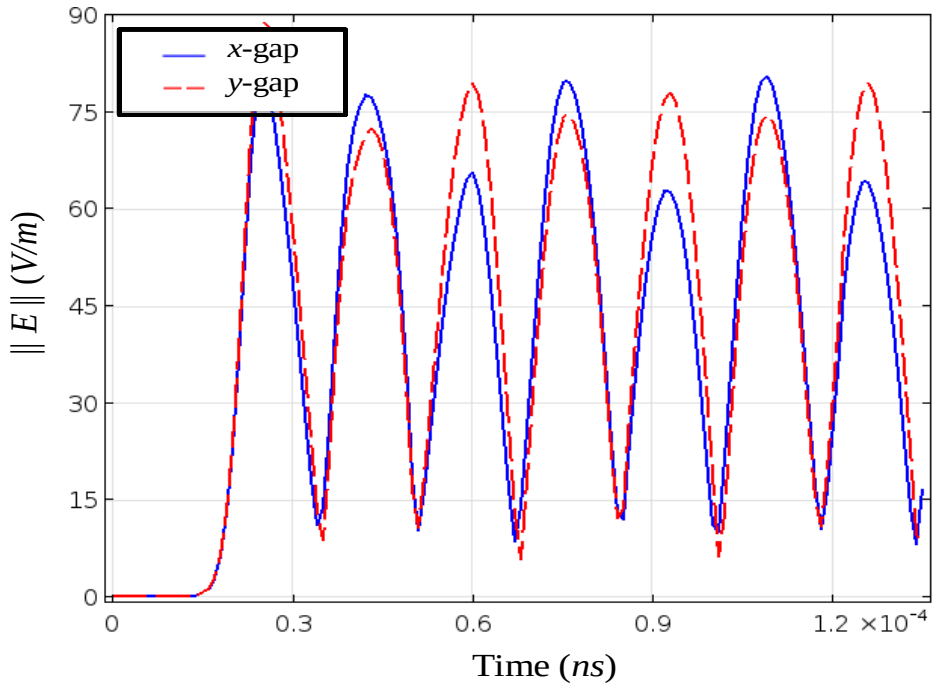

Figure 4.20: Normalized field at the gap for σ_{xxo} = 2.5 × 10^3 S/m, α = 0.02 m/V.

❖ $\sigma_{xxo} = 2.5 \times 10^3$ S/m and $\alpha = 0.03$ m/V

For the same value of conductivity, we set value of α to 0.03 m/V. The presence of DC voltage is observed in the x-polarized wave, as shown in Fig. 4.21. The x-polarized electric field E_x at x-gap shifts upward. The positive peak of E_x is around 75 V/m, whereas the negative peak is around 45 V/m. The average of the polarized wave over a certain time gives a non-zero value. The normalized electric field at the gaps, shown in Fig. 4.22, also indicates the presence of the DC component since the electric field at the gap along x direction is not uniform with time. The generated voltage V_{gen} estimated from the DC shift is $56\ nV$.

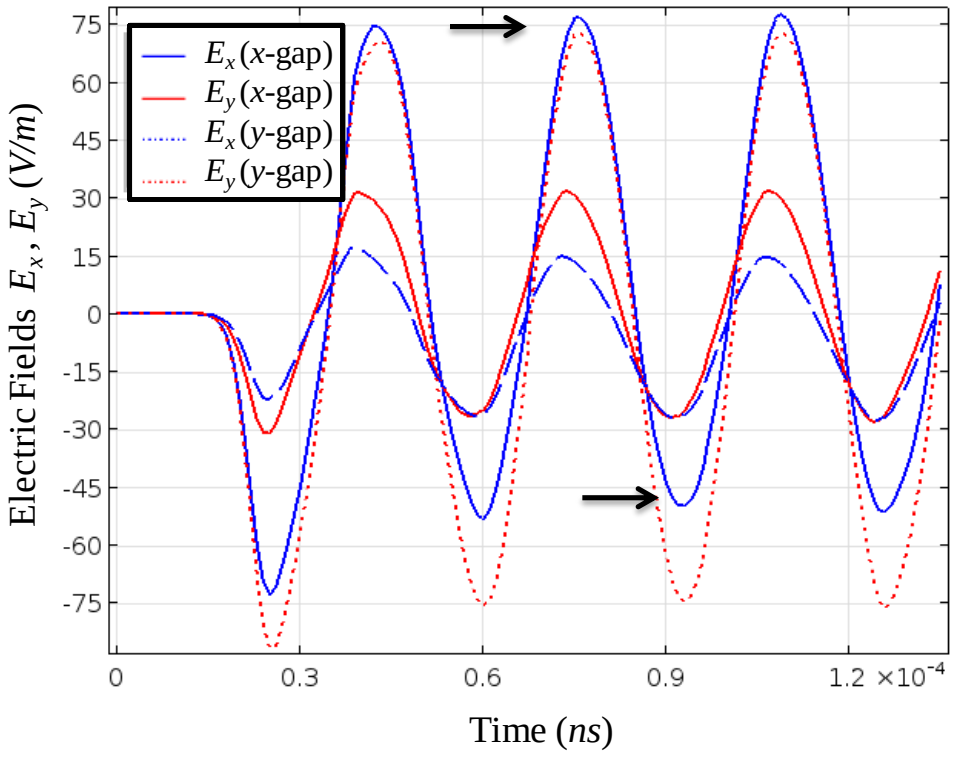

Figure 4.21: Electric field (E_x, E_y) at the gap for σ_{xxo} = 2.5 × 10^3 S/m, α = 0.03 m/V.

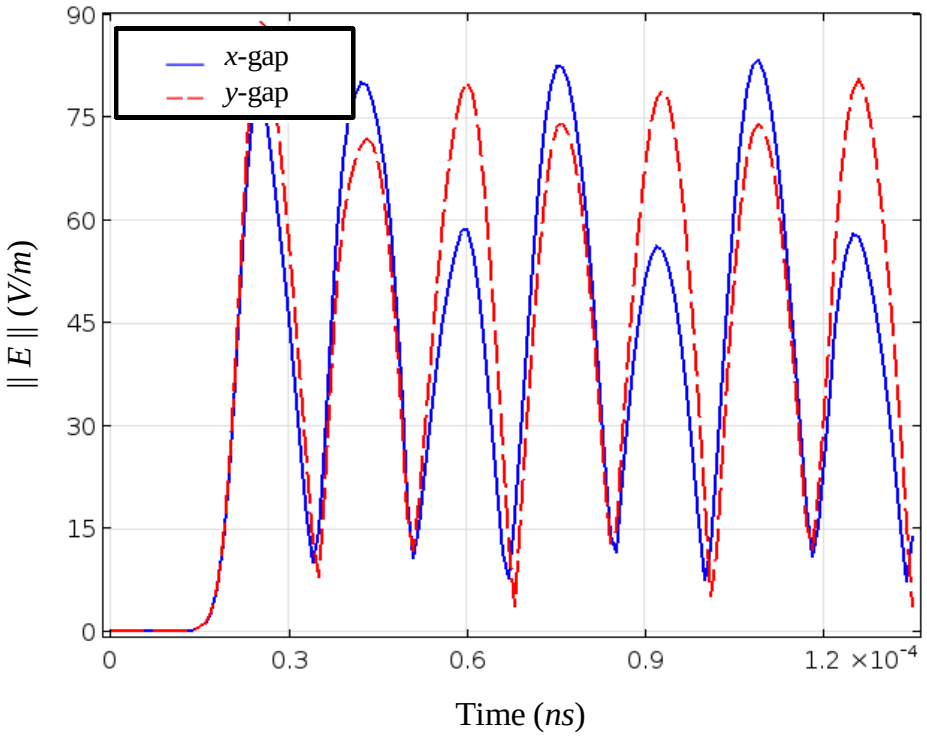

Figure 4.22: Normalized field at the gap for σ_{xxo} = 2.5 $\times 10^3$ S/m, α = 0.03 m/V.

❖ $\sigma_{xxo} = 2.5 \times 10^3$ S/m and $\alpha = 0.04$ m/V

We set $\alpha = 0.04$ m/V while the DC conductivity remains the same. Unlike other cases, there is a significant dc shift in the x-polarized wave in both x and y gap, as shown in Fig. 4.23. The x-polarized electric field E_x at x-gap shifts significantly upward. The positive peak of E_x is around 80 V/m, whereas the negative peak is around 40 V/m. The average of the polarized wave over a certain time gives a non-zero value. In addition, the x-polarized electric field E_x at y-gap shifts slightly downward. The normalized electric field at the gaps, shown in Fig. 4.24, also indicates the presence of the DC component since the electric field at the gap along x direction is not uniform with time. We estimate the generated voltage $V_{gen} = 82\ nV$ from the DC shift of the polarized wave.

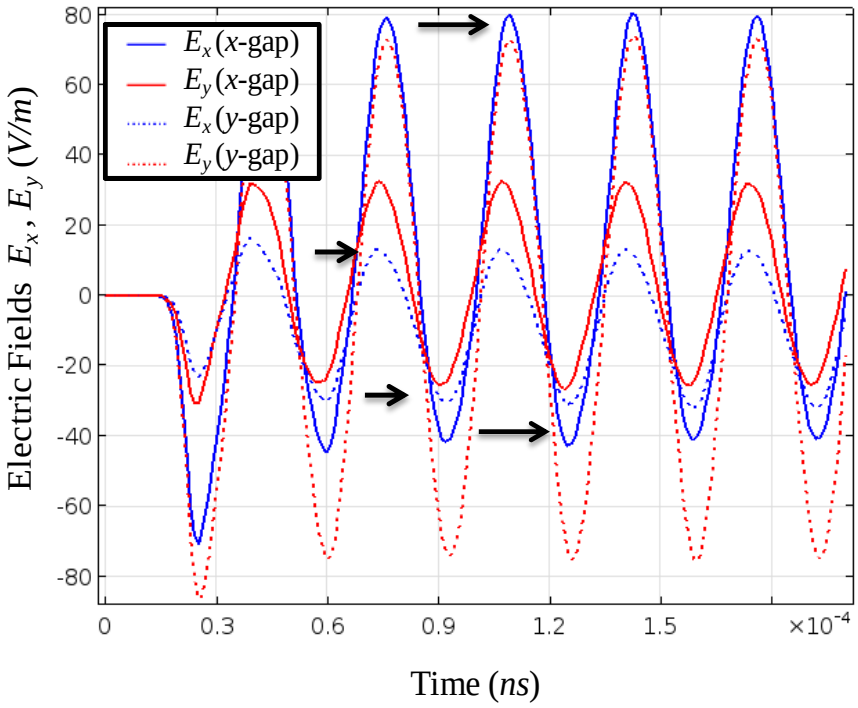

Figure 4.23: Electric field (E_x, E_y) at the gap for σ_{xxo} = 2.5 × 10^3 S/m, α = 0.04 m/V.

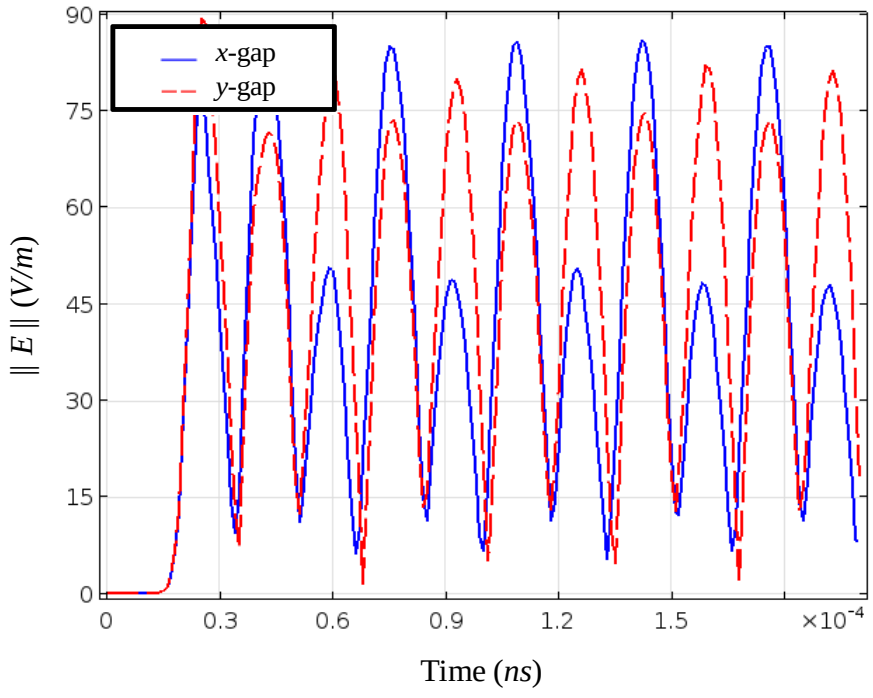

Figure 4.24: Normalized field at the gap for σ_{xxo} = 2.5 × 10^3 S/m, α = 0.04 m/V.

❖ $\sigma_{xxo} = 2.5 \times 10^3$ S/m and $\alpha = 0.05$

We set the value of DC conductivity to $\sigma_{xxo} = 2.5 \times 10^3$ S/m and α to 0.05 m/V. The presence of a significant DC shift is observed in the polarized wave, as shown in Fig. 4.25. The *x*-polarized electric field E_x at *x*-gap shifts significantly upward. The positive peak of E_x is around 80 V/m, whereas the negative peak is around 35 V/m. The average of the polarized wave over a certain time gives a non-zero value. In addition, the *x*-polarized electric field E_x at *y*-gap shifts downward significantly.

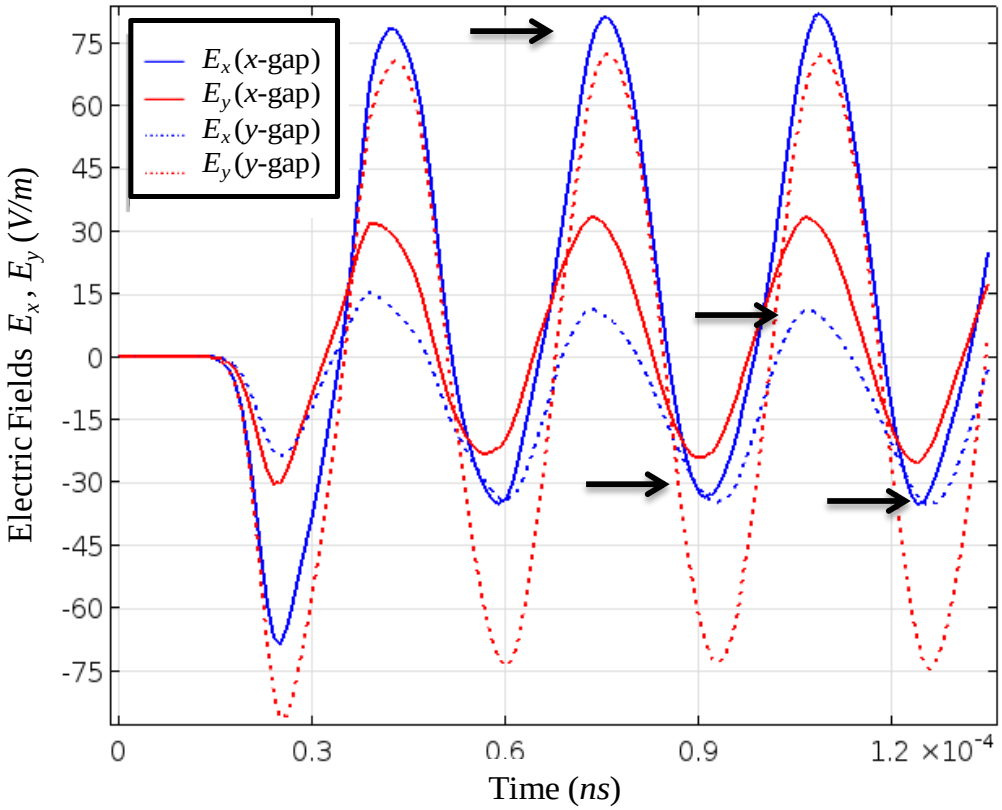

Figure 4.25: Electric field (E_x, E_y) at the gap for σ_{xxo} = 2.5 × 10^3 S/m, α = 0.05 m/V.

The positive peak of E_x at *y*-gap is around 15 V/m, whereas the negative peak is around 30 V/m. The normalized electric field at the gaps, shown in Fig. 4.26, indicates the

presence of the DC component since the electric field at the gap along x direction is not uniform with time. We estimate the generated voltage $V_{gen} = 106\ nV$.

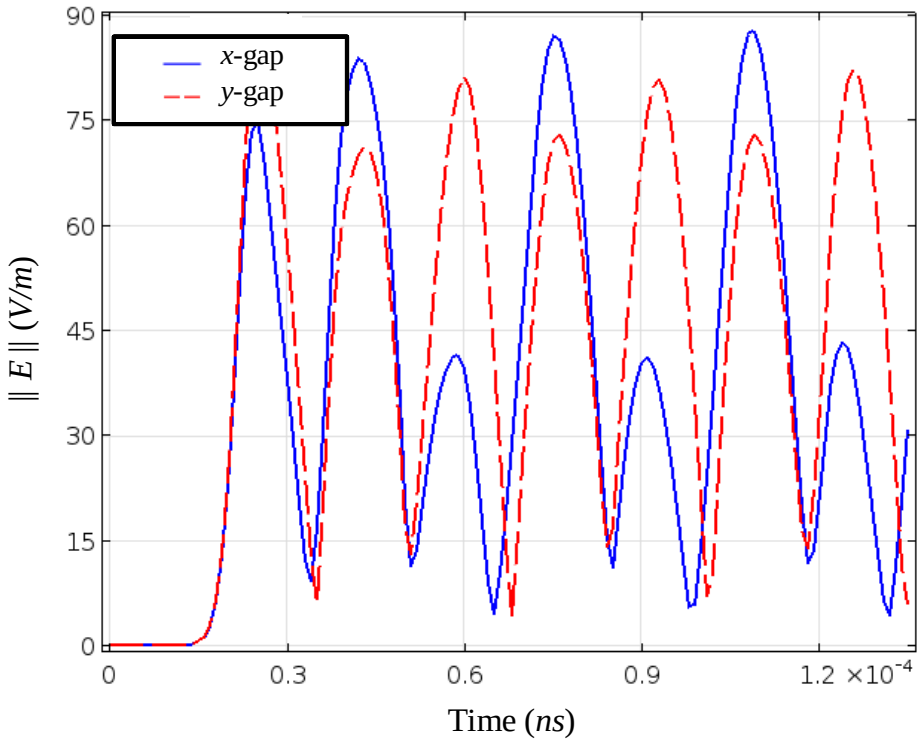

Figure 4.26: Normalized field at the gap for σ_{xxo} = 2.5 $\times 10^3$ S/m and α = 0.05 m/V.

❖ $\sigma_{xxo} = 2.5 \times 10^4$ S/m and $\alpha = 0.01$ m/V

To further investigate the effect of the anisotropic material on the polarized waves, we set the value of dc conductivity to $\sigma_{xxo} = 2.5 \times 10^4$ S/m and $\alpha = 0.01$ m/V. However, in this case, no DC shift is observed in the polarized waves, as shown in Fig. 4.27. The normalized electric field at the gaps, shown in Fig. 4.28, also indicates no DC component in the polarized waves since the electric field at the gap in both directions is uniform with time.

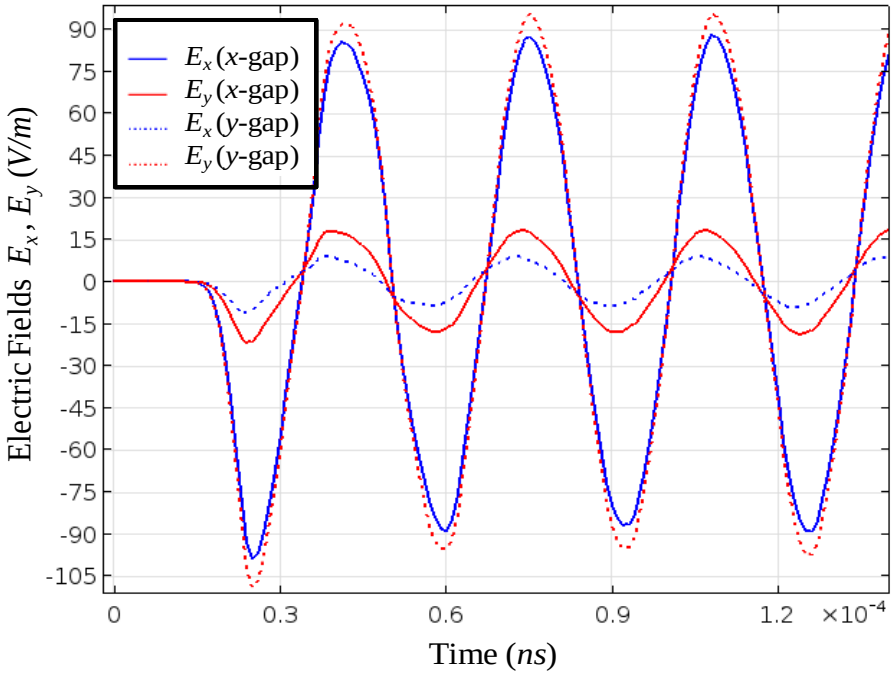

Figure 4.27: Electric field (E_x, E_y) at the gap for σ_{xxo} = 2.5 × 10^4 S/m, α = 0.01 m/V.

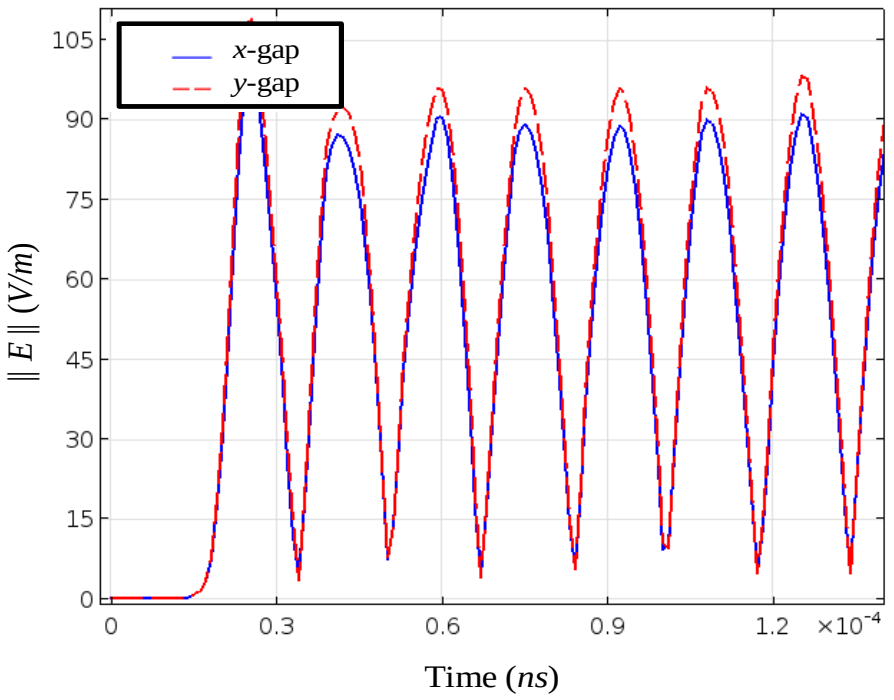

Figure 4.28: Normalized field at the gap for σ_{xxo} = 2.5 × 10^4 S/m, α = 0.01 m/V.

❖ $\boldsymbol{\sigma_{xxo} = 2.5 \times 10^4}$ **S/m and** $\boldsymbol{\alpha = 0.04}$

For the same value of conductivity, we set the value of α to 0.04 m/V. The *x*-polarized electric field E_x becomes more pronounced in *x*-gap and *y*-polarized electric field E_y becomes stronger in y-gap. However, no DC shift is observed in the polarized waves, as shown in Fig. 4.29. The normalized electric field at the gaps, shown in Fig. 4.30, also indicates no DC components in the polarized waves since the electric field at the gap in both directions is uniform with time.

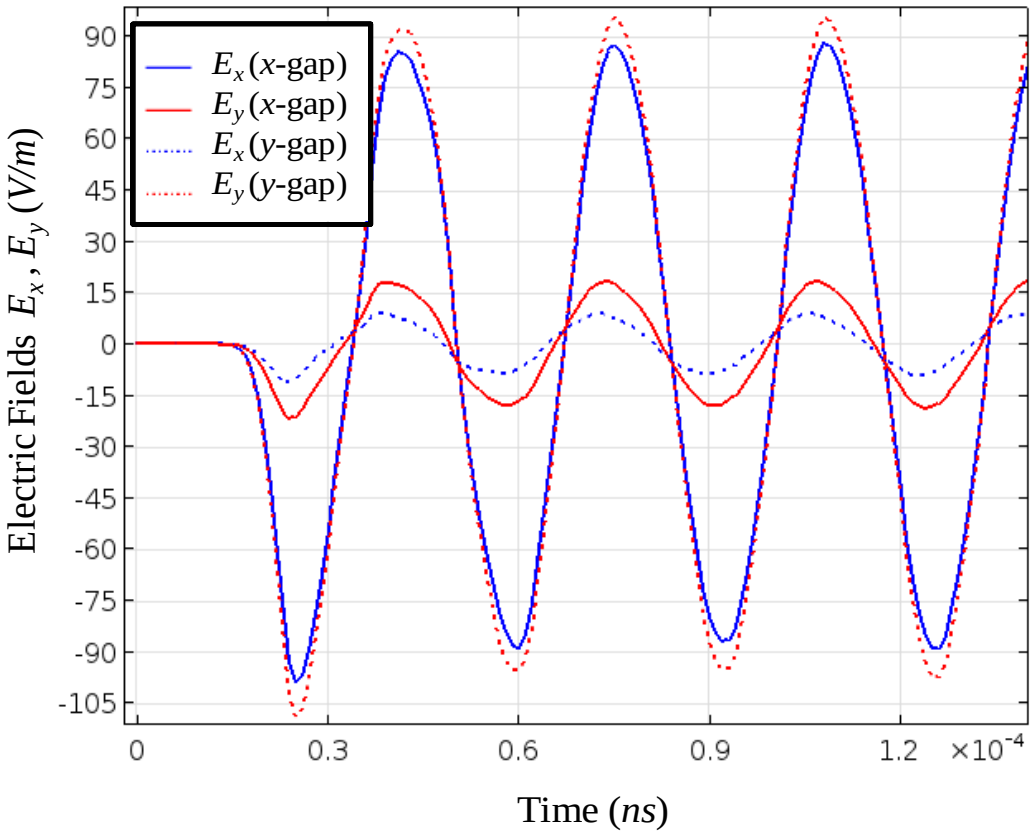

Figure 4.29: Electric field (E_x, E_y) at the gap for σ_{xxo} = 2.5 × 10^4 S/m, α = 0.04 m/V .

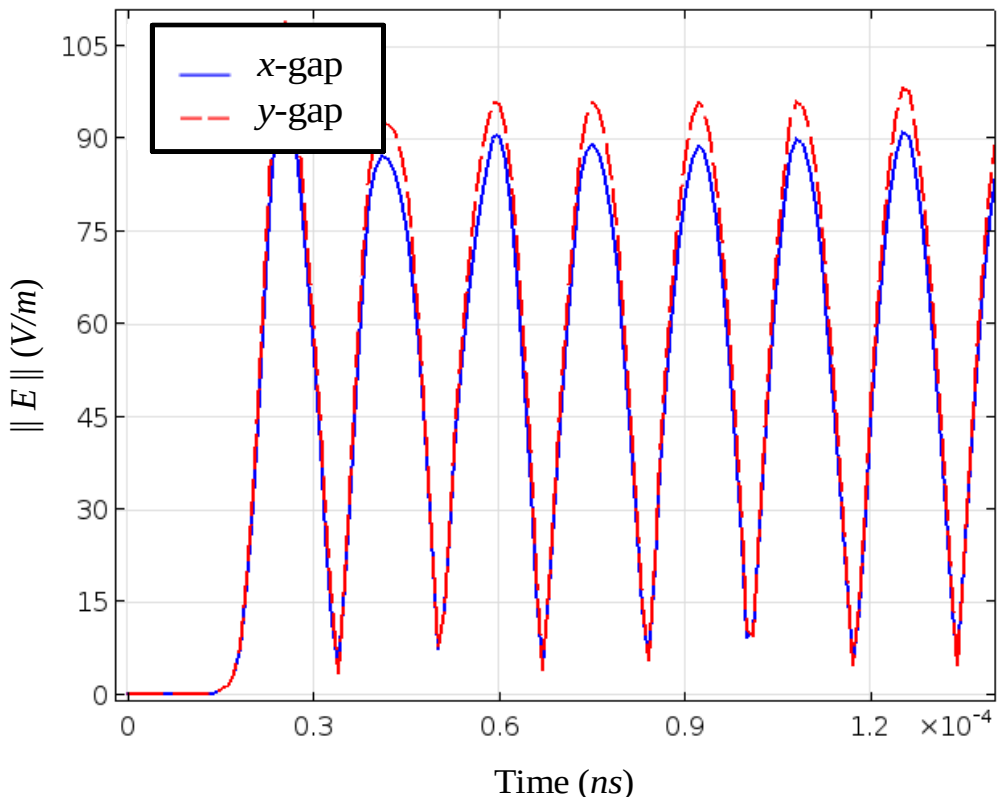

Figure 4.30: Normalized field at the gap for σ_{xxo} = 2.5 $\times 10^4$ S/m, α = 0.04 m/V.

In retrospect, it is noticed that once the value of the DC conductivity is set to $\sigma_{xxo} = 2.5 \times 10^3$ S/m, for different values of the nonlinear conductivity coefficient, i.e. $\alpha = 0.01, 0.02, 0.03, 0.04,$ and 0.05 m/V, the generated voltage V_{gen} increases and becomes significantly high at $\alpha = 0.05$ m/V. We further investigated our design by increasing the DC conductivity of the material by one order of magnitude i.e. $\sigma_{xxo} = 2.5 \times 10^4$ S/m. However, there is no existence of the DC shift in the orthogonally polarized electric fields for $\sigma_{xxo} = 2.5 \times 10^4$ S/m with different values of α.

We obtain a DC voltage difference across the terminal of the nanoantenna through the

parameterization of DC conductivity and nonlinear conductivity coefficient of the loaded anisotropic material in the gap. Our study indicates that for different values of DC conductivity σ_{xxo} and fixed α (i.e. $\alpha = 0.04$ m/V), a significant amount of voltage is generated i.e.$V_{gen} = 82\,nV$ at $\sigma_{xxo} = 2.5 \times 10^3$ S/m, as shown in Fig. 4.31. Fig. 4.32 shows that as the value of α increases from 0.01 to 0.05 for corresponding $\sigma_{xxo} = 2.5 \times 10^3$ S/m, the nonlinear component $\alpha\,\sigma_{xxo}\,E_y$ becomes comparable to σ_{xxo} and exhibits a significant DC shift in the polarized electric field resulting in large generated voltage. However, a further increase in the DC conductivity decreases the intensity of the electric field at the gap which affects the nonlinearity of the anisotropic material at the gap. This results in low voltage generation at the gap of the energy harvester.

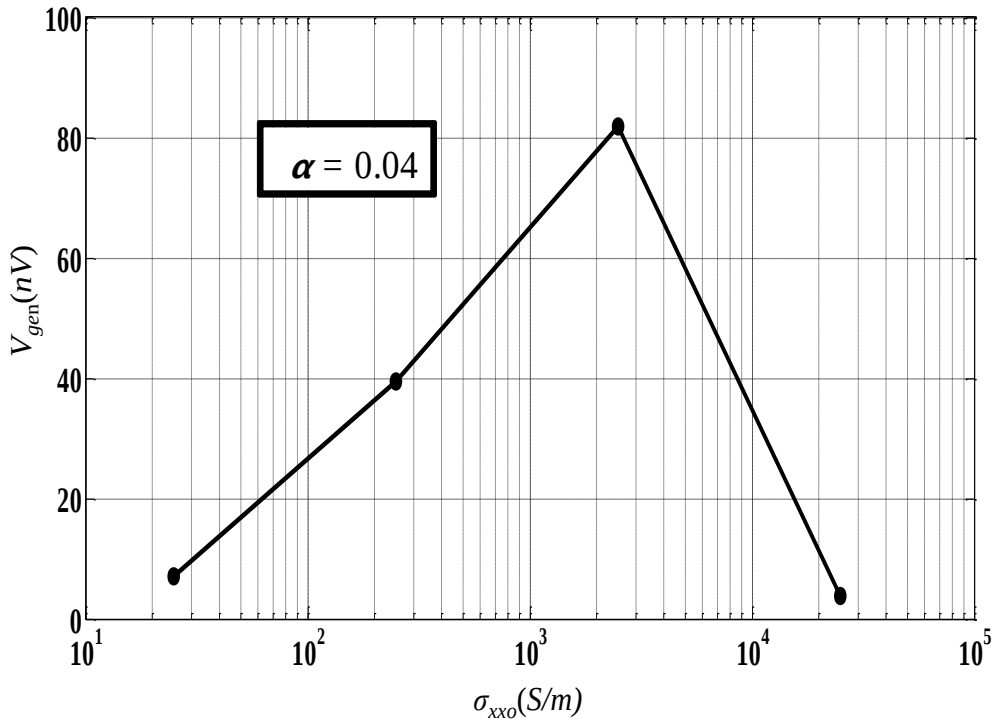

Figure 4.31: Generated voltage for different values of DC conductivity σ_{xxo} at fixed α = 0.04 m/V.

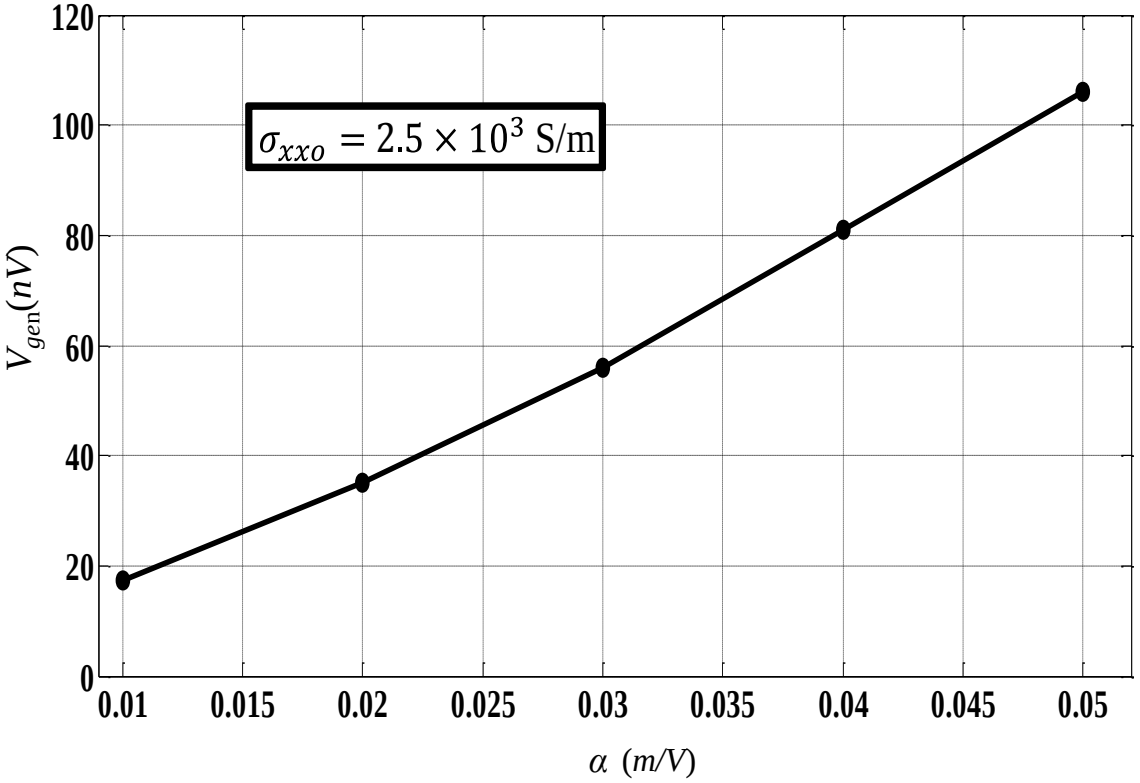

Figure 4.32: Generated voltage for different values of the nonlinear conductivity coefficient α at a fixed σ_{xxo} = 2.5 ×10^3 S/m.

4.6. Choice of Anisotropic Material

The anisotropic material which is employed in the simulation for our proposed model is an analytical material which has a characteristic of nonlinear electrical conductivity. Since the conductivity of the anisotropic material is direction-dependent, the conductivity of the material can be presented as a tensor quantity. In our design, the conductivity of the material in the x-direction σ_{xx} is dependent on the y-polarized electric field (E_y). The nonlinear conductivity in one direction of the anisotropic material leads to interesting

results once the light wave comes to the interaction with the dual polarized energy harvester.

However, the closest resembles of the loaded anisotropic material in nature and the design of the necessary mechanism (e.g. ohmic contact) is not the scope of this report, but part of our future work. We are currently investigating materials such as Graphene [75], GaAs thin films [76] and porous Si [77] as potential candidates for the anisotropic material of our novel energy harvester.

4.7. Optimization of Generated Voltage

Our proposed model is not optimized to obtain the maximum generated voltage. It is possible to maximize the generated voltage by optimizing the gap and geometrical parameters of the cross bowtie nanoantenna.

The generated voltage can be optimized through the spatial orientation of the anisotropic material in the gap with respect to the inner tips of cross bowtie nanoantenna. Since the high-intensity local field is generated at sharp corners or tips of the nanostructure, a rotation of 45 degrees of the anisotropic material at the gap, as shown in Fig.4.33, might result in high local field confinement at the gap between the material and the nanoantenna.

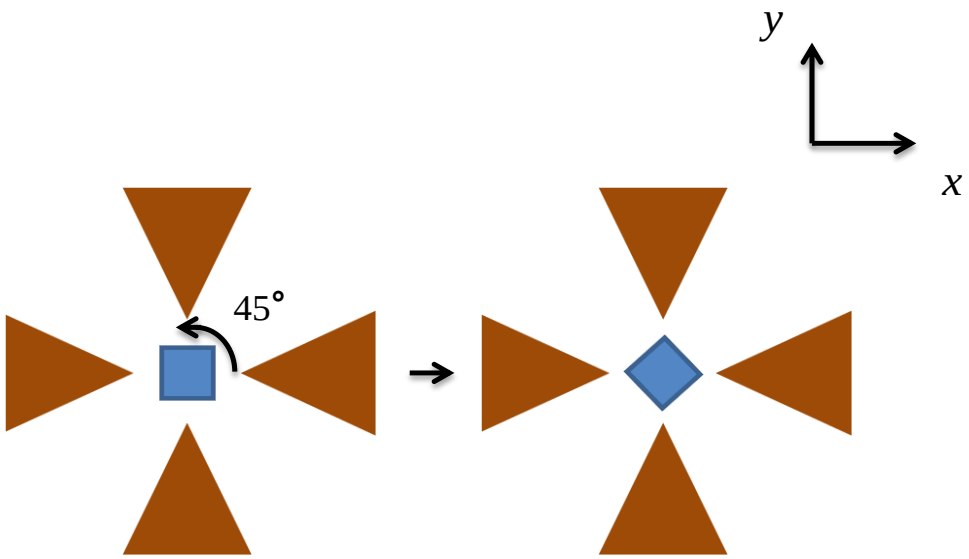

Figure 4.33: Optimization of the generated voltage by changing the spatial orientation of the anisotropic material at the gap.

In real life, the received field by the nanoantenna is weak. Therefore, in our simulation the strength of the electric field is selected to be 1 V/m. Our study shows that a significant DC voltage at micro-level can be generated using one device.

4.8. Array Configuration of Energy Harvester

An array with a large number of these energy harvesters can be connected in series/parallel to achieve reasonable voltage and power levels for energy harvesting applications. It is important to realize the connection of the device in an array in order to extract the energy efficiently. Fig 4.34 shows a parallel array configuration of the energy harvesting device. For parallel array configuration, the device is placed on a substrate and connected parallel to each other. The voltage is extracted from the gap of the harvester

through the common feed lines. These feed lines are connected to the devices by the vertical connections through the substrate.

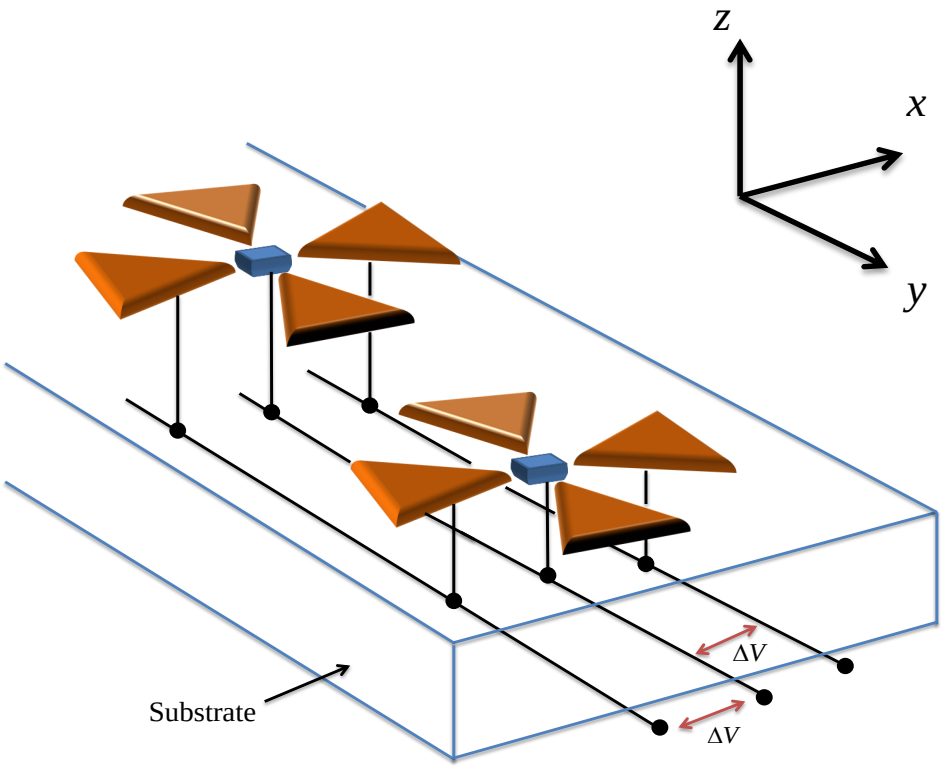

Figure 4.34: Isometric view of parallel array configuration of the energy harvester

The energy harvesters can also be connected to each other through series connections, as shown in Fig. 4.35. The generated voltage is connected in series in this array configuration. The series array configuration is simple and more convenient to implement. However, the overall output voltage using series connection is reduced due to the voltage drop across the anisotropic material. On the other hand, the parallel array configuration offers high output voltage compared to the series connections but it is difficult to implement.

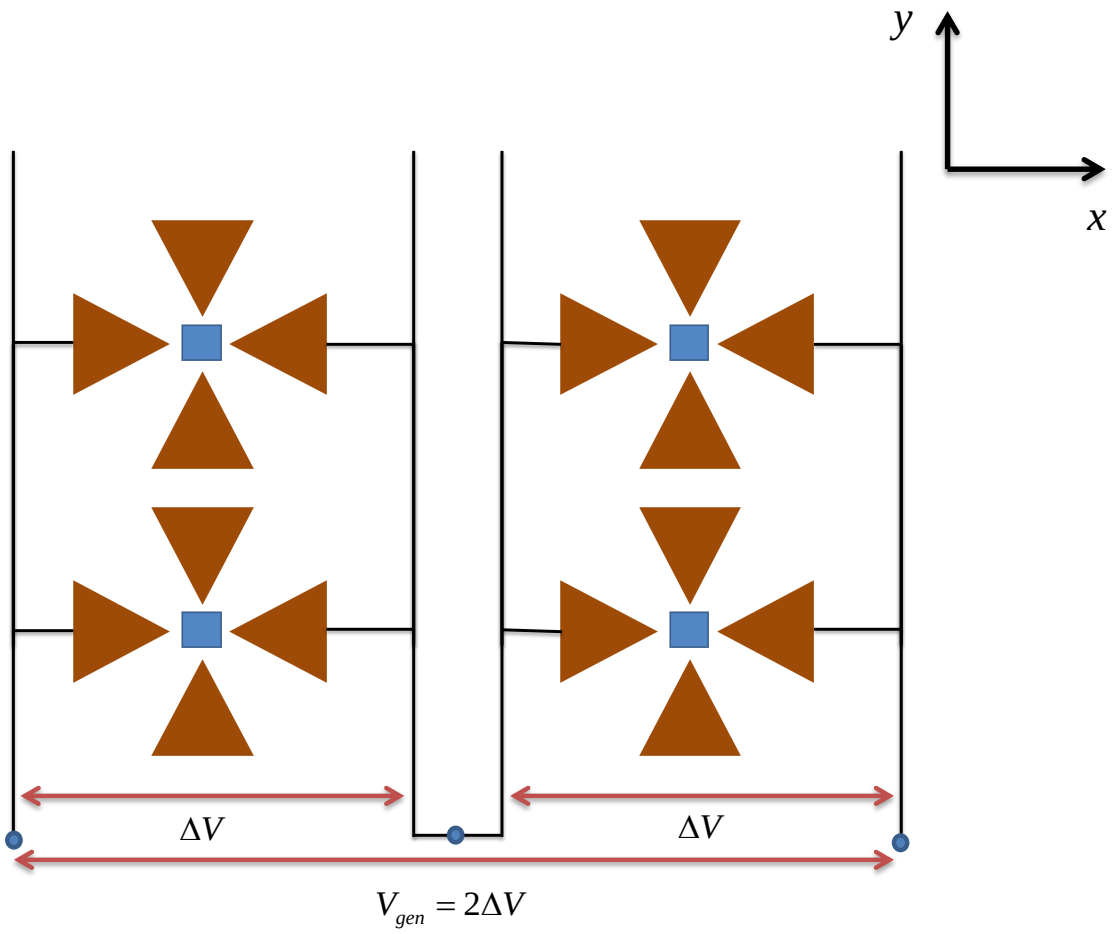

Figure 4.35: Top view of series array configuration of the energy harvester

CHAPTER 5

5.1 Conclusion

In this research work, we propose a novel technique to harvest solar energy of infrared radiation into DC energy at without using MIM diode. A theoretical study is performed to verify our proposed model in infrared regime as a proof of concept. Our proposed design is a sub-wavelength device which consists of dual polarized nanoantenna loaded with an anisotropic material in its gap. There are two major advantages of our proposed energy harvester. Firstly, the proposed device creates local field enhancement at its gap regardless of the polarization of the incoming light. Secondly, the design is able to perform rectification of solar electromagnetic radiation in the high-frequency regime without using MIM diode.

Our novel energy harvester consists of a dual polarized cross bowtie nanoantenna with an anisotropic material loaded in its gap. The theory of our energy harvester depends on the utilization of dual polarized cross bowtie nanoantenna. Therefore, we carry out a parametric study to investigate the variation of the local field enhancement at the gap with the geometrical parameters of the dual polarized nanoantenna. All the parametric studies of the dual polarized cross bowtie nanoantenna are performed using COMSOL Multiphysics software. A few conclusions can be drawn from the parametric studies of the dual polarized cross bowtie nanoantenna. Firstly, the local field increases and redshifts as the gap-size becomes smaller. Secondly, the local field at the resonance

redshifts and increases as the length of the nanoantenna increases. Thirdly, the local field at the resonance decreases and shifts to a shorter wavelength as the width of the nanoantenna increases. Finally, the effect of the tip-shape on the local field enhancement is investigated which indicates that the field at the gap decreases with the increase in the radius of the curvature of the tip.

To demonstrate the novel approach to generate DC energy from the infrared radiation by our energy harvester, an anisotropic material is loaded in the gap of the dual polarized cross bowtie nanoantenna. It is necessary to observe the nonlinear effects of the anisotropic material over the structure once the dual polarized waves interact. Therefore, time-domain simulation is carried out. The set up for time-domain simulation is different from its counterpart. Moreover, the simulation in time-domain is time-consuming and requires more memory to compute. A non-zero DC shift is observed in the polarized waves for specific values of DC conductivity and nonlinear conductivity coefficient of the anisotropic material. We estimate the generated voltage across the terminal of the nanoantenna from this DC shift in the polarized wave. It is theoretically proved that our proposed energy harvester is capable of generating DC energy from the infrared radiation.

5.2 Future Works

It is common in research that there are always some questions unanswered or room for improvement. Although some interesting results are achieved through our simulation model, there are still some works that can be listed to be done in the future. Firstly, the

anisotropic material that is employed in the design is an analytical material which has a defined nonlinear electrical conductivity. To find the closest resemblance to the material which has this kind of properties in nature can be listed as one of our future works in order to fabricate the prototype design. Secondly, since the fabrication of the nanostructure is challenging, it requires investigation whether we are able to extend the theory of our novel energy harvester for low frequency regime i.e. microwave. This proof will lead the theory to be generalized for all electromagnetic waves. If the model works in microwaves regime; essentially, the dimension of the device will get large, i.e. millimeter range. This will make the fabrication process much easier compared to nanometer range. Thirdly, the geometrical parameters of the nanoantenna and the spatial orientation of the anisotropic material at the gap can be optimized to obtain the maximum generated voltage for our model. Therefore, a handful of works left for future research which offers many exciting opportunities for future students.

References

[1] N. S. Lewis, G. Crabtree, A. J. Nozik, M. R. Wasielewski, and P. Alivisatos, "Basic Research Needs for Solar Energy Utilization," *Basic Energy Sci. Work. Sol. Energy Util.*, p. 276, 2005.

[2] Environmental Energy Technologies Division Newsletter, "Cool Color Project: Improved Materials for Cooler Roof," Lawrence Berkeley National Laboratory.

[3] C. K. Ho, C. M. Ghanbari, and R. B. Diver, "Concentrating Solar Power Plants," pp. 1–10, 2010.

[4] R. A. Voloshin, V. D. Kreslavski, S. K. Zharmukhamedov, V. S. Bedbenov, S. Ramakrishna, and S. I. Allakhverdiev, "Photoelectrochemical cells based on photosynthetic systems : a review," *Biofuel Res. J.*, vol. 6, pp. 227–235, 2015.

[5] Ariel Efrati, Chun-Hua Lu, Dorit Michaeli, Rachel Nechushtai, Sabine Alsaoub, Wolfgang Schuhmann and Itamar Willner, "Assembly of photo-bioelectrochemical cells using photosystem I-functionalized electrodes," *Nature Energy*, 2016.

[6] G. Abadal, J. Alda, and J. Agustí, "World's largest Science , Technology & Medicine Open Access book publisher Electromagnetic Radiation Energy Harvesting – The Rectenna Based Approach."

[7] I. E. Hashem, N. H. Rafat, and E. A. Soliman, "Dipole nantennas terminated by traveling wave rectifiers for ambient thermal energy harvesting," *IEEE Trans.*

Nanotechnology, vol. 13, no. 4, pp. 767–778, 2014.

[8] M. Bareiß, A. Hochmeister, G. Jegert, G. Koblmüller, U. Zschieschang, H. Klauk, B. Fabel, G. Scarpa, W. Porod, and P. Lugli, "Energy Harvesting using Nano Antenna Array," *IEEE International Conference on Nanotechnology*, pp. 218–221, 2011.

[9] L. Mescia and A. Massaro, "New Trends in Energy Harvesting from Earth Long-Wave Infrared Emission," *Advances in Materials Science and Engineering,* vol. 2014, 2014.

[10] Bailey R. L., "A proposed new concept for a solar-energy converter", *Journal of Engineering for Power*, April, 1972.

[11] E. Donchev, J. S. Pang, P. M. Gammon, A. Centeno, F. Xie, P. K. Petrov, J. D. Breeze, M. P. Ryan, D. J. Riley, and N. M. Alford, "The rectenna device: From theory to practice (a review)," *MRS Energy Sustain. - A Rev. J.*, vol. 1, pp. 1–34, 2014.

[12] L. Novotny, "Effective wavelength scaling for optical antennas," *Phys. Rev. Lett.*, vol. 98, no. 26, pp. 1–4, 2007.

[13] S. Grover, "Diodes for Optical Rectennas," *PhD Thesis*, 2011.

[14] L. Novotny and N. Van Hulst, "Antennas for light," vol. 5, *Nature Photonics*, February, 2011.

[15] R. Corkish, M. A. Green, T. Puzzer, and T. Humphrey, "Efficiency of antenna solar collection," *3rd World Conf. onPhotovoltaic Energy Convers. 2003 Proc.*, vol. 3, no. September, pp. 6–9, 2003.

[16] D. Marks and M. Alvin, "Femto diode and applications," *ed: EP Patent* 0172464A2, 1986.

[17] M. N. Gadalla and A. Shamim, "Design, Optimization and Fabrication of a 28.3 THz Nano-Rectenna for Infrared Detection and Rectification," pp. 1–9, *Scientific Reports, Nature Publishing Group,* 2014.

[18] R. Corkish, M. A. Green, and T. Puzzer, "Solar energy collection by antennas," *Soler Energy*, vol. 73, no. 6, pp. 395–401, 2002.

[19] D. Y. Goswami, S. Vijayaraghavan, S. Lu, and G. Tamm, "New and emerging developments in solar energy," *Soler Energy*, vol. 76, no. 1–3, pp. 33–43, 2004.

[20] C. H. Henry, "Limiting efficiencies of ideal single and multiple energy gap terrestrial solar cells," *J. Appl. Phys.*, vol. 51, no. 8, pp. 4494–4500, 1980.

[21] Hertz H., "Dictionary of Scientific Biography," Vol. VI, Scribner: *New York*, 2007, pp. 340 – 349.

[22] W. C. Brown, "The History of Power Transmission by Radio Waves," *IEEE Trans. Microwave Theory Tech.*, vol. 32, no. 9, pp. 1230–1242, 1984.

[23] G. H. Lin, R. Abdu, and J. O. Bockris, "Investigation of resonance light absorption

and rectification by subnanostructures," *J. Appl. Phys.*, vol. 80, no. 1, p. 565, 1996.

[24] W. C. Brown, "Optimization of the Efficiency and Other Properties of the Rectenna Element," *MTT-S Int. Microw. Symp. Dig.*, vol. 76, pp. 142–144, 1976.

[25] Dickinson R.M. and Brown W.C., "Radiated Microwave Power Transmission System Efficiency Measurements," Tech. Memo 33-727; *Jet Propulsion Lab., California Inst. Technol., Pasadena*, CA, March 15, 1975.

[26] J. O. Mcspadden, S. Member, L. Fan, and K. Chang, "Design and Experiments of a High-Conversion-Efficiency 5.8-GHz Rectenna - Microwave Theory and Techniques, *IEEE Transactions*," vol. 46, no. 12, 1998.

[27] Y.-H. Suh, C. Wang, and K. Chang, "Circularly polarised truncated-corner square patch microstrip rectenna for wireless power transmission," *IEEE Electronics Letter*, vol. 36, no. 7, p. 600, 2000.

[28] X.-X. Yang, C. Jiang, A. Z. Elsherbeni, F. Yang, and Y.-Q. Wang, "A Novel Compact Printed Rectenna for Data Communication Systems," *IEEE Transaction Antennas Propagation.*, vol. 61, no. 5, pp. 2532–2539, 2013.

[29] X. X. Yang, C. Jiang, A. Z. Elsherbeni, F. Yang, and Y. Q. Wang, "A novel compact printed rectenna for data communication systems," *IEEE Transaction, Antennas Propagation*, vol. 61, no. 5, pp. 2532–2539, 2013.

[30] Y. H. Suh and K. Chang, "A high-efficiency dual-frequency rectenna for 2.45- and 5.8-GHz wireless power transmission," *IEEE Transaction, Microwave Theory and*

Techniques., vol. 50, no. 7, pp. 1784–1789, 2002.

[31] T. W. Yoo and K. Chang, "Theoretical and Experimental Development of 10 and 35 GHz Rectennas," *IEEE Transaction, Microwave Theory and Techniques,* vol. 40, no. 6, pp. 1259–1266, 1992.

[32] J. O. McSpadden, T. Yoo, and K. Chang, "Theoretical and experimental investigation of a rectenna element\nfor microwave power transmission," *IEEE Transactions, Microwave Theory and Techniques*, vol. 40, no. 12, pp. 2359–2366, 1992.

[33] P. Koert and J. T. Cha, "Millimeter wave technology for space power beaming," *IEEE Transactions, Microwave Theory and Techniques,* vol. 40, no. 6, pp. 1251–1258, 1992.

[34] Koert P., Cha J.-T., and Macina M., "35 and 94 GHz rectifying antenna systems," In *Power from Space Dig., Paris, France* , Aug. 1991 , pp. 541 – 547 .

[35] H. K. Chiou and I. S. Chen, "High-efficiency dual-band on-chip rectenna for 35- and 94-GHz wireless power transmission in 0.13μm CMOS technology," *IEEE Transaction, Microwave Theory and Techniques*, vol. 58, no. 12, pp. 3598–3606, 2010.

[36] S. a Maier, *Fundamentals and Applications Plasmonics : Fundamentals and Applications*, vol. 677, no. 1. 2004.

[37] P. Bharadwaj, B. Deutsch, and L. Novotny, "Optical Antennas," *Advances in*

optics and photonics, pp. 438–483, 2009.

[38] M. Born and E. Wolf, "Principles of optics," *Principles of Optics Electromagnetic Theory of Propagation Interference and Diffraction of Light 2nd edition by Max Born Emil Wolf New York NY Pergamon Press 1964*. pp. 1–952, 1999.

[39] M. N. Gadalla, "Nano Antenna Integrated Diode (Rectenna) For Infrared Energy Harvesting," *M.Sc. Thesis*, 2013.

[40] Jurgen Jahns, Stefan Helfert, "Introduction to Micro and Nanooptics," *Physics Textbook.*

[41] Prof. Judah Levine, "Light and Color," Physics 1230, Fall 2001.

[42] R. H. Ritchie, "Plasma Losses by Fast Electrons in Thin Films," *Phys. Rev.*, vol. 106, no. 5, pp. 874–881, 1957.

[43] S. P. Gurunarayanan, "Anisotropy Engineering in 3D Magnetoplasmonic Nanoantennas," *Masters Thesis*, 2014.

[44] William L. Barnes, Alain Dereux and Thomas W. Ebbesen, "Surface Plasmon Subwavelength Optics," *Nature*, 824-830 (2003).

[45] S. Zeng, D. Baillargeat, H.-P. Ho, and K.-T. Yong, "Nanomaterials enhanced surface plasmon resonance for biological and chemical sensing applications.," *Chem. Soc. Rev.*, vol. 43, no. 10, pp. 3426–52, 2014.

[46] J. M. Luther, et al., Localized surface plasmon resonances arising from free

carriers in doped quantum dots, *Nature Materials*, 2011.

[47] S. Zeng, K.-T. Yong, I. Roy, X.-Q. Dinh, X. Yu, F. Luan, "A review on functionalized gold nanoparticles for biosensing appliations," *Plasmonics, Springer*, 2011.

[48] D. K. Kotter, S. D. Novack, and W. D. Slafer, "Solar nantenna electromagnetic collectors," *Proceedings of International Conference Energy Sustainability.*, pp. 1–7, 2008.

[49] E. Krasnok, I. S. Maksymov, I. Denisyuk, P. Belov, E. Miroshnichenko, C. R. Simovski, and Y. S. Kivshar, "Optical nanoantennas," *Physics-Uspekhi*, vol. 56, no. 6, pp. 539–564, 2013.

[50] Harry A. Atwater and Albert Polman, "Plasmonics for improved photovoltaic devices," *Nature Material*, February, 2010.

[51] T.-P. Vo, M. Mivelle, S. Callard, a Rahmani, F. Baida, D. Charraut, a Belarouci, D. Nedeljkovic, C. Seassal, G. W. Burr, and T. Grosjean, "Near-field probing of slow Bloch modes on photonic crystals with a nanoantenna.," *Opt. Express*, vol. 20, no. 4, pp. 4124–35, 2012.

[52] M. I. Tribelsky and B. S. Luk'yanchuk, "Anomalous light scattering by small particles," *Phys. Rev. Lett.*, vol. 97, no. 26, 2006.

[53] E. R. Brown, "A system-level analysis of Schottky diodes for incoherent THz imaging arrays," *2003 Int. Semicond. Device Res. Symp. ISDRS 2003 - Proc.*, vol.

6, no. 1982, pp. 380–381, 2003.

[54] H. Kazemi, K. Shinohara, G. Nagy, W. Ha, B. Lail, E. Grossman, G. Zummo, W. R. Folks, J. Alda, and G. Boreman, "First THz and IR characterization of nanometer-scaled antenna-coupled InGaAs/InP Schottky-diode detectors for room temperature infrared imaging," *Infrared Technology and Application XXXIII*, vol. 6542, pp. J5421–J5421, 2007.

[55] Blake J. Eliasson, "Metal-Insulator-Metal Diode for Solar Energy Conversion," *PhD Thesis*, 2001.

[56] S. Grover, S. Member, G. Moddel, and S. Member, "Applicability of Metal/ Insulator/Metal (MIM) Diodes to Solar Rectennas," *IEEE journal of Photovoltaics*, vol. 1, no. 1, pp. 78–83, 2011.

[57] Donald Neamen, "Semiconductor Physics and Devices," Third Edition.

[58] V. Daneu, D. Sokoloff, A. Sanchez, and A. Javan, "Extension of Laser Harmonic Frequency Mixing Techniques into the 9 μ Region with an Infrared Metal-Metal Point-Contact Diode," *Applied Physics Letter*, vol. 15, no. 12, pp. 398–401, 1969.

[59] J. C. Fisher and I. Giaever, "Tunneling through thin insulating layers," *J. Applied Physics*, vol. 32, no. 2, pp. 172–177, 1961.

[60] A. Sanchez, C. F. Davis, K. C. Liu, and A. Javan, "The MOM tunneling diode: Theoretical estimate of its performance at microwave and infrared frequencies," *J. Applied Physics*, vol. 49, no. 10, pp. 5270–5277, 1978.

[61] A. M. A. Sabaawi, S. Member, C. C. Tsimenidis, and S. Member, "Analysis and Modeling of Infrared Solar Analysis and Modeling of Infrared Solar Rectennas," *IEEE Journal of Selected Topics in Quantum Electronics*, May, 2013.

[62] S. Grover, O. Dmitriyeva, M. J. Estes, and G. Moddel, "Traveling-wave metal/insulator/metal diodes for improved infrared bandwidth and efficiency of antenna-coupled rectifiers," *IEEE Transaction, Nanotechnology.*, vol. 9, no. 6, pp. 716–722, 2010.

[63] M. Aldrigo, D. Masotti, A. Costanzo, and V. Rizzoli, "Numerical analysis of an innovative energy-harvesting system in the infrared region," *2013 IEEE Wireless Power Transfer WPT 2013*, pp. 123–126, 2013.

[64] M. N. Gadalla and A. Shamim, "28.3THz Bowtie Antenna Integrated Rectifier for Infrared Energy Harvesting," *Proceedings of the 44th European Microwave Conference*, pp. 652–655, 2014.

[65] K. Wang, H. Hu, S. Lu, L. Guo, and T. He, "Design of a sector bowtie nano-rectenna for optical power and infrared detection," *Front. Phys.*, vol. 10, no. 5, 2015.

[66] Z. Zhu, S. Joshi, S. Grover, and G. Moddel, "Graphene geometric diodes for terahertz rectennas," *Journal of Physics D: Applied Physics*, vol. 46, no. 18, p. 185101, 2013.

[67] E. Briones, J. Alda, and F. J. González, "Conversion efficiency of broad-band

rectennas for solar energy harvesting applications," *Opt. Express*, vol. 21, no. S3, p. A412, 2013.

[68] K. A. I. W. Ang, H. H. U. Aifeng, S. L. U. Han, L. I. G. Uo, T. A. O. Z. Hang, Y. U. H. An, A. O. Z. Hou, and T. H. E. Ao, "Design and analysis of a square spiral nano- rectenna for infrared energy harvest and conversion," vol. 6, no. 12, pp. 3977–3991, *Optical Material Express*, 2016.

[69] Ezzeldin A.Soliman, "Wideband nanocrescent plasmonic antenna with engineered spectral response," *Microwave and Optical Technology Letters*, March, 2013.

[70] A. Y. Elsharabasy, E. A. Soliman, M. H. Bakr, and M. J. Deen, "Nano crescent antenna with variable axial ratio for energy harvesting applications," *Photonics North, PN 2016*, May, pp. 1–3, 2016.

[71] "COMSOL Multiphysics Software", Version 5.1, COMSOL Inc., Burlington, MA.

[72] C. Paper, C. Di, G. Universit, L. Universit, E. H. View, and C. Di Garbo, "Review of Infrared Nanoantennas for Energy Harvesting," *International Conference on Modern Electrical Power Engineering*, July, 2016.

[73] A. Chekini, S. Sheikhaei, and M. Neshat, "A novel plasmonic nanoantenna structure for solar energy harvesting," *IEEE Conference, Millimeter-Wave Terahertz Technology MMWaTT*, pp. 20–24, 2017.

[74] P. R. West, S. Ishii, G. V Naik, N. K. Emani, and V. M. Shalaev, "Searching for better plasmonic materials," *Laser & photonics*, vol. 808, no. 6, pp. 795–808,

2010.

[75] J. B. Khurgin, "Graphene - A rather ordinary nonlinear optical material," *Applied Physics Letter*, vol. 104, no. 16, 2014.

[76] H. J. Shin, D. W. Park, S. J. Oh, J. O. Kim, H. Kim, S. K. Noh, and J. H. Son, "High-field nonlinear conductivities of n- and p-type GaAs thin films in the terahertz region," *Current Applied Physics*, vol. 16, no. 7, pp. 793–798, 2016.

[77] M. Ben-Chorin, F. Moller, and F. Koch, "Nonlinear Electrical-transport In Porous Silicon," *Physics Review B*, vol. 49, no. 4, pp. 2981–2984, 1994.